Large Scale Dynamics and Fluctuations in Non-Equilibrium Stochastic Particle Systems

by

Andrea Pizzoferrato

Thesis

Submitted to the University of Warwick

for the degree of

Doctor of Philosophy

Mathematics Institute

Contents

Acknowledgments

About 15 years ago, I asked my father to buy a textbook used in American high schools. It was simply titled "*Physics*" by J.D. Cutnell and K.W. Johnson. I remember spending many hours admiring the pictures while browsing through the pages. At that time, I thought that books were enough to gain knowledge about a topic. However, I was wrong. During the years, I learnt a lot by interacting with other students and researchers, sharing ideas and intuitions. Most importantly, these people were able to support me in many difficult moments and now I am convinced that this journey of study would not have been possible alone.
So, besides Cutnell and Johnson,

I would like to express my deepest and warmest gratitude to my supervisors Paul Chleboun and Stefan Grosskinsky, for their immense patience and continuous dedication during the PhD. They have always been available to share their knowledge and to explain every detail of our research. I will miss the pleasant atmosphere of our meetings.

I am also thankful to the many scientist I had the opportunity to discuss my work with. In particular, Rosemary Harris for her support in shaping the direction of my research at the beginning of the PhD, Davide Gabrielli for having spent a long evening at the CIRM in Marseilles to answer my questions about the Macroscopic Fluctuation Theory, and Hugo Touchette for having made my participation to the conference in South Africa possible and for his kindness in listening to my doubts about the future.

I am grateful to Angela, Salvatore and Valerio for all their support at every level since 1988.

I am also very happy to thank Adriano and Elena, roaring lion and lioness no matter what obstacle appears in their lives. They have been an example of

resolution and they have never stopped believing in my skills, even when I was not.

I will never, ever forget the crew of fellow PhD students during my years at the Mathematics Institute. Thanks to them, I was able to understand that "*Friendship is holding each others hands at the edge of a cliff*" like someone used to say. So, I hope I won't say goodbye to: Alice the Fighter, Aurelio the Good, Bruno the Teacher, Enrico the Believer, Ferdinando the Aristocrat, Francesco the Sweet, Gian Lorenzo the Romantic Hero, Giovanni the Right, Ilaria the Elegant, Livia the Player, Cassa the Mad, Massimo the Idealist, Mattia the Rock and Serena the Nest Keeper.

Many thanks also to:

Costanza for being a sparkling office mate,

Damiano to keep dancing and singing in the rain,

Merve and Tom who have helped me taking things less seriously,

Jacopo for his clear sociological analysis,

Francesco for his scissor mastery,

Pierpaolo for sharing our passion for technology,

Flavia if not for her support at the beginning of my studies I would not be here writing this, and

Chiara, who during the last 10 years has been a secure handhold when heavy winds were blowing and a twirling firefly when the nights were darker. To her, Cesare and Francesco I wish the very best.

Finally, my last thought goes to Dario, Kevin and Leonardo who have been fixed, but unfortunately distant, stars during all these years: even if our roads are driving us apart, I promise to guide you all through the only real journey that is meaningful doing in ones life.

Magis

Declarations

This work has been composed by myself and has not been submitted for any other degree or professional qualification.

- Chapters 2,3 and 4 present standard theory for Stochastic Particle Systems and Large Deviations which will be used throughout the thesis.
- Part of the work in Chapter 5 has been published in [20].
- The final section of Chapter 5 and the whole Chapter 6 extend significantly the work in [20] and will be submitted for publication.
- In Chapter 7 we apply the analysis scheme developed in [51] to another model. The results of this chapter are in preparation for publication.

Abbreviations

CKE: Chapman-Kolmogorov Equation

CTMC: Continuos Time Markov Chain

EP: Exclusion Process

HCTMC: Homogeneous Continuos Time Markov Chain

IP: Inclusion Process

GBE: Global Balance Equation

JV: Jensen-Varadhan

LDP: Large Deviations Principle

LDT: Large Deviations Theory

MBQT: Many-Body Quantum Theory

ME: Master Equation

NESS: Non-Equilibrium Stationary State

PA: Partially Asymmetric

SCGF: Scaled Cumulant Generating Function

SEP: Simple Exclusion Process

SM: Statistical Mechanics

SPS: Stochastic Particle Systems

TA: Totally Asymmetric

TPM: Transition Probability Matrix

w.r.t.: with respect to

ZRP: Zero-Range Process

CHAPTER 1

Introduction

Statistical Mechanics (SM) is a branch of theoretical physics which inquires the properties of systems made up of a large number of interacting components. Starting from the details of the dynamics describing the interaction among the smaller components, the goal of statistical mechanics is to determine the emergent collective behaviour of the system resulting from the interaction of its constitutive parts. In this way, SM constitutes a bridge between the microscopic and macroscopic worlds. Starting from the begining of the last century, SM has proven to be successful in describing many phenomena related to condensed matter physics like, just to cite a few, ferromagnetism [27, 1], law of gases [22, 6], glass states [90] etc. Notwithstanding, the fields of application of this subject goes far beyond pure physics and they reach artificial intelligence [24], quantitative sociolgy [36, 5], economics [29, 30], biology [77] etc. For all these reasons, SM is a vibrant and active discipline which keeps holding the attention of the scientific community.

To describe the emergent collective behaviours, we need to define macroscopic observables which are linked to microscopic quantities. In the present thesis, we will mainly focus on the density of particles in a system and their current, that is the net flow of particles in a specific direction. In particular, we will be interested in the stationary regime of the macroscopic current which is given by a suitable average over the microscopic and quickly fluctuating particle flow. When the detailed balance condition is satisfied the system is said to be in equilibrium, and on average there is no net stationary current. In general, a system may be able to exhibit many equilibrium configurations which can be selected by choosing suitable values of a tuning parameter, such as temperature. This abrupt change as a parameter varies is often called a phase transition and determining the critical thresholds among phases is one of the fundamental questions which SM tries to answer. Instead, when the macroscopic stationary current has a value different from zero, the system is in a *Non-Equilibrium Stationary State* (NESS) and this will be of central interest for

the present work.

The class of systems which are able, under certain conditions, to exhibit NESSs we will study are called *Stochastic Particle Systems* (SPS) (although in the literature they are also known as Interacting Particle Systems or Stochastic Lattice Gases or Driven Diffusive Systems). They consist of a discrete lattice, which can have closed or open boundary conditions, where each site carries a certain number of particles. The lattice can also be in contact with particle reservoirs. The particles present in the model can move in a continuous time process to other sites following certain probabilistic rules specified via jump rates. In the present thesis, we will consider two SPS models which are usually called the *Zero-Range Process* (ZRP), introduced in [75], and the *Inclusion Process* (IP), introduced in [39]. Regarding the former, particles are allowed to move to other sites with a jump rate rule which is a function of the number of particles of the departure site only. For the latter, the jump rates depend on the departure as well as the arrival site and they are increasing with both number of particles. We will fix the underlying lattice to be either a one-dimensional ring (periodic boundary conditions) or a one-dimensional open boundary systems in contact with two particle reservoirs at the edges of the lattice. For these two geometries, the ZRP and the IP admit stationary probability distributions of product form (see [3, 23, 19]) which are well understood. Certain choices of the jump rates allow ZRPs to exhibit a condensation transition in homogeneous systems due to particle interactions when the density exceeds a critical value [28, 33]. This has been studied in detail in recent years (see e.g. [35, 40, 41] and references therein), and has seen many applications [31, 15, 21]. The IP also admits a condensation transition for certain parameter choices [44] which, however, are not considered in the present work. It is important to note that SPS can also be studied from a macroscopic perspective via a hydrodynamic limit [56]. This description relies on the continuity equation for mass conservation and will be explored throughout the thesis. Due to the particular form of the stationary probability distribution, it is often possible to determine explicitely the typical behaviour for the main observables, like density and current, in the NESS. For this reason, it is interesting to study what happens out of the stationary regime and in particular what is the most likely way to realize an atypical fluctuation [25]. It should be noted that typical fluctuations "close enough" to the average values are already covered by the central limit theorem. Instead, fluctuations far from the mean can be treated using *Large Deviation Theory* (LDT) [80, 32]. This mathematical framework predicts an exponential decay, as the number of trials or the observation time of the experiment grows, of the probability of measuring a

value of an observable far away from its mean. The proportionality factor in the exponent is also called the rate or cost function.

The large deviation behaviour of dynamic observables has been a topic of major recent research interest in SPS. Most studies, as summarized in a recent review [60], focus on the particle current as one of the most important characteristics of nonequilibrium systems in one dimension. In general, current fluctuations are studied from a microscopic or macroscopic point of view. For the first perspective, algebraic techniques are implemented to calculate eigenvalues and eigenvectors of an exponentially tilted version of the generator of a stochastic lattice gas. In this way, the rate function of the large deviations of the current is calculated as a Legendre-Fenchel transform of the greatest eigenvalue of the tilted generator. These methods were successfully applied to the asymmetric simple exclusion process (where each site can allocate at most one particle) [42, 14], also in combination with the matrix product ansatz [26], and to ZRPs [47, 49, 51]. The statistics of the current and symmetry properties of the rate function can also be understood in the framework of the fluctuation theorem [61]. However, the symmetry relation stemming from the fluctuation theorem, also called Gallavotti-Cohen symmetry, breaks down in high current regimes for some condensing systems [50, 68]. Almost all previous studies focus on open boundary conditions, with only few available for periodic boundary conditions [66, 83], where microscopic results are difficult to obtain due to temporal correlations [46].

From the macroscopic point of view, one of the most powerful frameworks introduced in recent years is the *Macroscopic Fluctuation Theory* (MFT) (see [8] and references therein), whose more general rigorous description is based on empirical flows [10, 9]. This is able to provide, as a result of a variational principle, the time evolution of the most likely density profile which typically gives rise to a given fluctuation. It turns out that it can be hard to solve the variational problem and an expression for the density profiles has only been obtained for some specific models [8, 60]. In particular, MFT takes into account symmetric or weakly asymmetric SPS models only. In these cases, the continuity equations is of the heat form which is necessary for the specific hydrodynamic description MFT relies on. Lower current deviations, that is fluctuations of the current below its typical value, are usually realized by phase separated states for systems with concave flux function such as the exclusion process. These states can be described as weak solutions of the conservation law on a hydrodynamic level, while upper large deviations of the current are associated to hyperuniform states with long-range correlations [53], which are not accessible on a purely macroscopic level. The connection between hydrodynamics

and large deviations is provided by the well-known concept of entropy production in weak solutions that exhibit shocks [74]. Using all possible entropy functionals, this can be used to identify a unique entropic solution to the hydrodynamic equation describing the typical behaviour. For non-entropic solutions the entropy production can provide the large deviation rate function for observing such a non-typical profile, if the correct thermodynamic entropy is used [86]. This connection has been proved rigorously for the ASEP [54, 87], giving rise to the so-called *Jensen-Varadhan* (JV) theory. In [78], this has been applied heuristically to obtain a macroscopic derivation of the rate function for lower current deviations, which coincide with results based on exact microscopic computations and are in agreement with MFT predictions. As we will see, the JV theory is complementary to the MFT since it considers total and partially asymmetric dynamics.

In this thesis, we exploit many techniques, both at microscopic and macroscopic level, to determine observables fluctuations. In particular, we will extend the JV approach to study lower current deviations for ZRPs which have a concave current-density relation. At first, we will focus on totally asymmetric dynamics with periodic boundary conditions, for which only few results exist so far. Then, we will apply the method to the IP to study upper current deviations, the current-density relation being convex for this model. We will also see how to extend the JV method in the case of partially asymmetry. In the end, we will apply the MFT and microscopic techniques to study symmetric IP with open boundary conditions which have not been addressed so far. For lattice dimension greater than one, fluctuations can arise as a consequence of current loops [88] which are not covered in the present work.

The remainder of the thesis is structured as follows. In Chapter 2, we present the quantum notation for linear algebra which is immediately applied to write homogenous continuos time markov chains in a form resembling the Schrödinger equation. In Chapter 3, we introduce SPS using the quantum notation and, in particular, we will define the two models of interest for the present work which are the ZRP and the IP. We will introduce the stationary probability measures and will define the main observables used to characterize the behaviour of SPS. Chapter 4 is dedicated to a review of large deviation theory and tools. We will first summarize the main results of LDT and we will provide the main methods to determine the rate function for atypical events from the microscopic as well as macroscopic point of view. In Chapter 5, we will look at macroscopic large deviations of the current for both the TAZRP and the TAIP using the JV approach. Chapter 6 extends the method of the preceding section to partially asymmetric dynamics. Lastly, in Chapter 7,

we will study macroscopic current fluctuations for the SIP in contact with particle reservoirs via MFT, and we will also determine the large deviation behaviour of the activity using a microscopic algebraic method.

CHAPTER 2

Preliminaries

This preliminary chapter is devoted to the definition of the mathematical framework which is used to describe the systems under study. First, we will go through the main concepts in linear algebra expressing them in terms of the Dirac notation. Second, we will exploit these tools to characterize homogeneous continuous time Markov Chains. In this way, it is possible to use methods developed within *Many-Body Quantum Theory* (MBQT) in the context of stochastic processes.

2.1 Quantum Formalism for Linear Algebra

In this section, we will review some fundamental structures of linear algebra using the Dirac notation which was originally developed in Quantum Mechanics. The quantum formalism was introduced in terms of operators on general Hilbert spaces with a unitary time evolution in mind [55]. When applied to stochastic processes with finite or countable state space it is essentially a reformulation of linear algebra results, and therefore we choose to work directly in this framework here, following closely the lecture notes [71]. Loosely speaking, in quantum mechanics all the information related to the dynamics of the physical system is contained within the Hamiltonian, while in stochastic processes the analogous operator is, as we will see, the generator of the process. The former is a Hermitian matrix which implies that all the eigenvalues are real (this is motivated by the fact that eigenvalues corresponds to measure of physical quantities which, by definition, are real numbers). The properties of the latter, which results from the conservation of probability, specify the sign of the real part of its eigenvalue (as a consequence of Gershgorin's theorem [69, p. 31]) which can also be complex. In addition, right and left eigenvectors of the generator are generally different.

2.1.1 Matrices and Vectors

A *matrix* $\mathcal{A}$ with $m \in \mathbb{N}^+$ rows and $n \in \mathbb{N}^+$ columns is an array of numbers $a_{ij} \in \mathbb{C}$ where i is the row index and j the column one. [1] It is usually represented as

$$\mathcal{A} \coloneqq [a_{ij}] \coloneqq \begin{pmatrix} a_{11} & a_{12} & \cdots & a_{1n} \\ a_{21} & a_{22} & \cdots & a_{2n} \\ \vdots & \vdots & \ddots & \vdots \\ a_{m1} & a_{m2} & \cdots & a_{mn} \end{pmatrix}. \tag{2.1}$$

In most of our applications, the matrix coefficients will be real valued but for generality purposes we consider the complex field. Vectors are obtained from special values of the matrix dimensions. In particular, we call *ket-vector* a matrix whose dimensions are $m > 1$ and $n = 1$. We indicate this object using the ket-symbol as

$$|u\rangle \coloneqq [u_{i1}] \coloneqq \begin{pmatrix} u_{11} \\ u_{21} \\ \vdots \\ u_{m1} \end{pmatrix}. \tag{2.2}$$

The elements of the canonical basis vector of $\mathbb{C}^m$ are denoted as $|e_k\rangle \coloneqq [e_i = \delta_{i,k}]$, where we used the Kronecker-symbol

$$\delta_{i,k} = \begin{cases} 1 & \text{if } i = k \\ 0 & \text{otherwise} \end{cases}. \tag{2.3}$$

In other words, $|e_k\rangle$ corresponds to a vector whose components are all zero except at the kth-row where we have 1. When $m = 1$ and $n > 1$, we define *bra-vectors* using the bra-symbol as

$$\langle v| \coloneqq |v\rangle^T = [v_{i1}]^T \coloneqq \begin{pmatrix} v_{11} & v_{12} & \cdots & v_{1n} \end{pmatrix}. \tag{2.4}$$

Similarly, the canonical basis elements are denoted as $[\delta_{i,k}]^T =: \langle e_k|$. In the end, we can form new matrices by linear combinations of other matrices like

$$\mathcal{C} = \alpha\mathcal{A} + \beta\mathcal{B} = [\alpha a_{ij} + \beta b_{ij}] = [c_{ij}], \tag{2.5}$$

where $\alpha, \beta \in \mathbb{C}$ and $\mathcal{A}, \mathcal{B}, \mathcal{C}$ have the same number of rows and columns.

[1] For the models discussed in this thesis, the elements a_{ij} will be real numbers but, as mentioned in [71, p. 11], they can be complex in some applications and here we follow this general description.

2.1.2 Matrix Product

Given a $m \times p$ matrix $\mathcal{A}$ and a $p \times n$ matrix $\mathcal{B}$ (with $m, p, n \in \mathbb{N}^+$), we define the *Matrix Product* $\mathcal{A} \cdot \mathcal{B}$ component-wise as

$$\mathcal{C} = \mathcal{A} \cdot \mathcal{B} = \left[\sum_{k=1}^{p} a_{ik} b_{kj}\right] = [c_{ij}] \quad \text{with} \quad \begin{matrix} 1 \leqslant i \leqslant m \\ 1 \leqslant j \leqslant n \end{matrix} , \tag{2.6}$$

where the resulting matrix $\mathcal{C}$ has dimensions $m \times n$. As in the previous section, special values of m, p, n give different types of matrix products. In fact, we have

- **Right Linear Map** - $m > 1$, $p > 1$, $n = 1$
  In this case, $\mathcal{B} = |b\rangle$ and $\mathcal{C} = |c\rangle$, so the matrix $\mathcal{A}$ acts as in the standard right multiplication of a matrix with a column vector $\mathcal{A}\,|b\rangle = |c\rangle$.

- **Left Linear Map** - $m = 1$, $p > 1$, $n > 1$
  Same as before, but for left matrix multiplication $\langle a|\,\mathcal{B} = \langle c|$.

- **Dyadic Product** - $m > 1$, $p = 1$, $n > 1$
  Sometimes this is also known as column by row product. It is indicated as $\mathcal{C} = |a\rangle\,\langle b|$ or in block-matrix form

$$\mathcal{C} = |a\rangle\,\langle b| = \begin{pmatrix} a_{11} \begin{pmatrix} b_{11} & b_{12} & \cdots & b_{1n} \end{pmatrix} \\ a_{21} \begin{pmatrix} b_{11} & b_{12} & \cdots & b_{1n} \end{pmatrix} \\ \vdots \\ a_{m1} \begin{pmatrix} b_{11} & b_{12} & \cdots & b_{1n} \end{pmatrix} \end{pmatrix} . \tag{2.7}$$

  The dyadic product provides a useful way to write the identity matrix $\mathcal{I}$. In fact, it is given as the sum of the dyadic products of the canonical basis elements as

$$\mathcal{I} = \sum_{k=1}^{m} |e_k\rangle\,\langle e_k| . \tag{2.8}$$

- **Dual Pairing** - $m = 1$, $p \geqslant 1$, $n = 1$
  In this case, the notation is shortened as

$$c = \langle a|b\rangle \in \mathbb{C}. \tag{2.9}$$

  Since we are using complex valued coefficients, the bilinear form is in general different from the scalar product $\sum_{k=1}^{p} \overline{a}_{ik} b_{kj}$ where $\overline{a}_{ik}$ is the complex conjugate of a_{ik}.

2.1.3 Kronecker Product

Let $\mathcal{A} = [a_{ij}]$ and $\mathcal{B} = [b_{kl}]$ be finite-dimensional matrices with sizes $m_{\mathcal{A}} \times n_{\mathcal{A}}$ and $m_{\mathcal{B}} \times n_{\mathcal{B}}$, respectively (with $m_{\mathcal{A}}, n_{\mathcal{A}}, m_{\mathcal{B}}, n_{\mathcal{B}} \in \mathbb{N}^+$). We define the *Kronecker product* (abbreviated as K-product or also called *tensor product*) $\mathcal{A} \otimes \mathcal{B}$ component-wise as [52]

$$\mathcal{C} = \mathcal{A} \otimes \mathcal{B} = [a_{ij} b_{kl}] = [c_{st}] \quad \text{with} \quad \begin{array}{c} s = (i-1)\, m_{\mathcal{B}} + k \\ t = (j-1)\, n_{\mathcal{B}} + l \end{array} , \tag{2.10}$$

where the resulting matrix $\mathcal{C}$ has dimensions $m_{\mathcal{A}} m_{\mathcal{B}} \times n_{\mathcal{A}} n_{\mathcal{B}}$. In block-matrix form, the above definition corresponds to

$$\mathcal{A} \otimes \mathcal{B} = \begin{pmatrix} a_{11}\mathcal{B} & a_{12}\mathcal{B} \\ a_{21}\mathcal{B} & a_{22}\mathcal{B} \end{pmatrix} = \begin{pmatrix} a_{11} \begin{pmatrix} b_{11} & b_{12} \\ b_{21} & b_{22} \end{pmatrix} & a_{12} \begin{pmatrix} b_{11} & b_{12} \\ b_{21} & b_{22} \end{pmatrix} \\ a_{21} \begin{pmatrix} b_{11} & b_{12} \\ b_{21} & b_{22} \end{pmatrix} & a_{22} \begin{pmatrix} b_{11} & b_{12} \\ b_{21} & b_{22} \end{pmatrix} \end{pmatrix} , \tag{2.11}$$

where we have fixed $m_{\mathcal{A}} = n_{\mathcal{A}} = m_{\mathcal{B}} = n_{\mathcal{B}} = 2$ for better readable text. In general, the K-product is not commutative

$$\mathcal{A} \otimes \mathcal{B} \neq \mathcal{B} \otimes \mathcal{A}, \tag{2.12}$$

but satisfies the following multiplication rule

$$(\mathcal{A} \otimes \mathcal{B}) \cdot (\mathcal{C} \otimes \mathcal{D}) = (\mathcal{A} \cdot \mathcal{C}) \otimes (\mathcal{B} \cdot \mathcal{D}) . \tag{2.13}$$

With respect to multiplications for constants we have

$$(\alpha\beta)\, (\mathcal{A} \otimes \mathcal{B}) = (\alpha\mathcal{A}) \otimes (\beta\mathcal{B}) = (\beta\mathcal{A}) \otimes (\alpha\mathcal{B}) . \tag{2.14}$$

For $p \in \mathbb{N}$, the p-fold K-product of a matrix with itself is denoted by $\mathcal{A}^{\otimes p}$ where by convention $\mathcal{A}^{\otimes 1} = \mathcal{A}$ and $\mathcal{A}^{\otimes 0} = \mathcal{I}$. The matrix products of the previous section can be characterized using the K-product. In fact, again by direct calculation, we have the following properties

- **Ket and bra vectors** - $m_{\mathcal{A}} > 1, n_{\mathcal{A}} = 1, m_{\mathcal{B}} > 1, n_{\mathcal{B}} = 1$
  For what regards ket-vectors, the K-product is abbreviated as

  $$|a, b\rangle \coloneqq |a\rangle \otimes |b\rangle \in \mathbb{C}^{m_{\mathcal{A}} m_{\mathcal{B}}}. \tag{2.15}$$

  In particular given $|e_i\rangle \in \mathbb{C}^{m_{\mathcal{A}}}$ and $|e_j\rangle \in \mathbb{C}^{m_{\mathcal{B}}}$, by direct calculation, we notice

that

$$|e_i, e_k\rangle = \left|e_{(i-1)m_{\mathcal{B}}+k}\right\rangle \in \mathbb{C}^{m_{\mathcal{A}}m_{\mathcal{B}}}, \tag{2.16}$$

that is the tensor product of two canonical basis elements gives an element of the canonical basis of the resulting higher dimensional space. Bra-vectors follow the same construction, that is

$$\langle a, b| \coloneqq \langle a| \otimes \langle b| = |a\rangle^T \otimes |b\rangle^T = |a, b\rangle^T \in \mathbb{C}^{n_{\mathcal{A}}n_{\mathcal{B}}}. \tag{2.17}$$

- **Local Operator**
  In the case of the product of many ket-vectors, we may need a matrix which is able to act on one component only of the K-factors. So, given $|b_1, b_2, \cdots, b_k, \cdots, b_L\rangle$ and the right linear map $\mathcal{A}|b_k\rangle = |c_k\rangle$, we define the *local operator* as the matrix

$$\hat{a}_k \coloneqq \mathcal{I}^{\otimes(k-1)} \otimes \mathcal{A} \otimes \mathcal{I}^{\otimes(L-k)}, \tag{2.18}$$

  which works as

$$\hat{a}_k |b_1, b_2, \cdots, b_k, \cdots, b_L\rangle = |b_1, b_2, \cdots, c_k, \cdots, b_L\rangle . \tag{2.19}$$

  The same holds for bra-vectors provided a specification of the corresponding left linear map $\langle c_k| = \langle a_k|\mathcal{B}$. Furthermore, two local operators acting on different components always commute

$$\hat{a}_k\hat{b}_l = \hat{b}_l\hat{a}_k \quad \text{with} \quad k \neq l \ . \tag{2.20}$$

- **Dyadic Product Commutation Rule** - $m_{\mathcal{A}} = 1, n_{\mathcal{A}} > 1, m_{\mathcal{B}} > 1, n_{\mathcal{B}} = 1$
  We simply have that

$$\langle a| \otimes |b\rangle = |b\rangle \otimes \langle a| = |b\rangle \langle a| . \tag{2.21}$$

- **Dual Pairing Factorization** - $m_{\mathcal{A}} = 1, n_{\mathcal{A}} = m_{\mathcal{B}} > 1, n_{\mathcal{B}} = 1$
  Consider a set of bra-vectors $\langle a_k|$ and ket-vectors $|b_k\rangle$ indexed by $k = 1, \cdots, L$. Bras and kets with the same index value have the same number of components $d_k \in \mathbb{N}^+$. Then the following equality holds

$$\langle a_1, a_2, \cdots, a_L|b_1, b_2, \cdots, b_L\rangle = \prod_{k=1}^{L} \langle a_k|b_k\rangle \in \mathbb{C}. \tag{2.22}$$

2.2 Quantum Matrix Form for HCTMC

Here, we first recall some basic concepts of *Continuos Time Markov Chains* (CTMC) together with the procedure to build a realization of the process. Then, we will translate the main equations of CTMC in terms of the Dirac notation. In this way, we will define the Master Equation of a CTMC and highlight the most important eigenvalues and eigenvectors. In the last part we will show, using the quantum matrix form, how it is possible to describe the stationary behaviour of the process by calculating the eigenvalues and eigenvectors of the transition probability matrix.

2.2.1 Basic Definitions and Construction

Following [2], a continuous time stochastic process is a family $(X_t : t \geqslant 0)$ of random variables taking values in a configuration or state space C. We consider C to be a finite set with $|C| = m \in \mathbb{N}^+$. If, for any finite set of "times" $0 \leqslant s_1 < \ldots < s_{n-1} < s < t + s$ (where we called $s_n = s$ and $s_{n+1} = t + s$ with $t > 0$) and corresponding set $C_1, C_2, \ldots, C_n, C_{n+1}$ of states in C, we have

$$\mathbb{P}\left[X_s = C_n, X_{s_{n-1}} = C_{n-1}, \ldots, X_{s_1} = C_1\right] > 0, \tag{2.23}$$

and the following identity holds

$$\mathbb{P}\left[X_{t+s} = C_{n+1} | X_s = C_n, X_{s_{n-1}} = C_{n-1}, \ldots, X_{s_1} = C_1\right] = \mathbb{P}\left[X_{t+s} = C_{n+1} | X_s = C_n\right] \tag{2.24}$$

then the stochastic process $(X_t : t \geqslant 0)$ is called a *Continuos Time Markov Chain* (CTMC). Moreover, if in addition to (2.24) also

$$\mathbb{P}\left[X_{t+s} = C_{n+1} | X_s = C_n\right] = \mathbb{P}\left[X_t = C_{n+1} | X_0 = C_n\right] \tag{2.25}$$

holds, then $(X_t : t \geqslant 0)$ is called a *Homogeneous Continuos Time Markov Chain* (HCTMC). In the following, we will consider HCTMC only [2]. As we will see, it is useful to fix an enumeration of states in C for notational convenience and write

$$C \coloneqq \{C_1, C_2, \ldots, C_m\}. \tag{2.26}$$

[2] Here $\mathbb{P}$ denotes the law of the process $(X_t : t \geqslant 0)$ on path space, which can be fully characterized by finite dimensional distributions of the form (2.23) by Kolmogorov's extension theorem (see [11] for details).

From (2.25), we can associate to a pair of states C_i, C_j the element of a matrix as

$$\mathcal{P}(t) \coloneqq [p_{ij}(t)] \coloneqq [\mathbb{P}[X_t = C_j | X_0 = C_i]]. \tag{2.27}$$

which is called *Transition Probability Matrix* (TPM). The TPM must satisfy the following properties

$$\begin{aligned} &\bullet\, p_{ij}(t) \geqslant 0 \\ &\qquad\qquad \forall i, j = 1, \ldots, m \text{ and } \forall t \geqslant 0\ . \\ &\bullet\, \textstyle\sum_{j=1}^{m} p_{ij}(t) = 1 \end{aligned} \tag{2.28}$$

Any matrix satisfying (2.28) is called a *Stochastic Matrix*. Denoting by $\mathbb{P}_{C_i}(0)$ the probability of being in state C_i at time 0, then

$$\mathbb{P}_{C_j}(t) \coloneqq \sum_{i=1}^{m} p_{ij}(t)\, \mathbb{P}_{C_i}(0) \tag{2.29}$$

is the probability of being in state C_j at time t. For HCTMC, we have the *Chapman-Kolmogorov Equation* (CKE) which is [57]

$$\mathcal{P}(t+s) = \mathcal{P}(t)\, \mathcal{P}(s). \tag{2.30}$$

Contrary to the discrete-time version, we can not iterate the CKE on $\mathcal{P}(s)$ or $\mathcal{P}(t)$, since an infinitesimal version of the TPM cannot be defined consistently [57, p. 460]. To overcome this difficulty, we introduce the *Generator* of the process, which is defined as

$$\mathcal{Q} \coloneqq [q_{ij}] \coloneqq \left.\frac{d\mathcal{P}(t)}{dt}\right|_{t=0}, \tag{2.31}$$

whose elements are specified in the following way

$$q_{ij} \coloneqq \begin{cases} \lim_{h\to 0} \frac{p_{ij}(h)}{h} & i \neq j \\ \lim_{h\to 0} \frac{p_{ii}(h)-1}{h} & i = j \end{cases}, \tag{2.32}$$

since $p_{ij}(0) = \delta_{i,j}$. From (2.28), we notice that that $q_{ii} = -\sum_{j\neq i} q_{ij} \leqslant 0$. The TPM and the generator are related to each other through *Kolmogorov's Differential Equations*

$$\frac{d\mathcal{P}(t)}{dt} = \mathcal{P}(t)\, \mathcal{Q} \tag{2.33}$$

$$= \mathcal{Q}\mathcal{P}(t) \tag{2.34}$$

where the first (second) is called *forward* (*backward*) *equation*. A formal solution to both (2.33) and (2.34) is given by

$$\mathcal{P}(t) = e^{\mathcal{Q}t} = \sum_{n=0}^{\infty} \frac{(\mathcal{Q}t)^n}{n!}, \tag{2.35}$$

when the series representation is well defined for finite state spaces.

2.2.2 Probability Vector and Expectation

The configuration space we have chosen for our presentation of CTMC is finite and can be enumerated. In this way, we can find a unique way to represent each element with a vector and it is natural to choose the canonical basis bra-vectors. So we have the following map

$$C_i \mapsto \langle e_i| =: \langle C_i| \; \forall i = 1, \ldots, m, \tag{2.36}$$

which implies that $\mathcal{I} = \sum_{i=1}^{m} |C_i\rangle \langle C_i|$. We notice that the vectors $|e_i\rangle$ have m entries with only one component equal to 1 and the remaining $m-1$ equal to 0. We express the generic observable whose value is configuration dependent as

$$\langle F| := \sum_{i=1}^{m} F_{C_i} \langle C_i| , \tag{2.37}$$

and its relative diagonal matrix as

$$\mathcal{F} := \sum_{i=1}^{m} F_{C_i} |C_i\rangle \langle C_i| . \tag{2.38}$$

In this way, having in mind (2.29), the *probability vector* is simply

$$\langle \mathbb{P}(t)| := \sum_{i=1}^{m} \mathbb{P}_{C_i}(t) \langle C_i| , \tag{2.39}$$

We notice that each component of $|\mathbb{P}(t)\rangle$ corresponds to the probability of finding the system at time t in the configuration associated to the entry with non-zero value of the relative canonical basis vector. The probability of finding the system in a specific state can be recovered by projecting the probability vector on its components, for instance

$$\langle C_j|\mathbb{P}(t)\rangle = \sum_{i=1}^{m} \mathbb{P}_{C_i}(t) \langle C_j|C_i\rangle = \sum_{i=1}^{m} \mathbb{P}_{C_i}(t) \delta_{j,i} = \mathbb{P}_{C_j}(t) . \tag{2.40}$$

Moreover, an element of the TPM can be obtained as

$$\langle C_i| e^{\mathcal{Q}t} |C_j\rangle = \langle C_i| \mathcal{P}(t) |C_j\rangle = \mathbb{P}[X_t = C_j | X_0 = C_i], \tag{2.41}$$

which is called the *Propagator* in the language of MBQT. As for discrete time Markov Chains, starting from an initial distribution on the configurations, the evolution of the probability vector is given by applying the TPM on the initial distribution

$$\langle \mathbb{P}(t)| = \langle \mathbb{P}(0)| \mathcal{P}(t). \tag{2.42}$$

The relation (2.42) is of fundamental importance, since by multipling on the left (2.33) with $\langle \mathbb{P}(0)|$ and then transposing the result, we get the *Master Equation* (ME)

$$\frac{d|\mathbb{P}(t)\rangle}{dt} = \mathcal{Q}^T |\mathbb{P}(t)\rangle, \tag{2.43}$$

whose formal solution

$$|\mathbb{P}(t)\rangle = e^{\mathcal{Q}^T t} |\mathbb{P}(0)\rangle \tag{2.44}$$

rules the evolution of the probability vector in terms of the generator of the process [3]. In this formalism, the law of conservation of probability can be written, using the *Summation Vector*

$$\langle \sigma| \coloneqq \sum_{i=1}^{m} \langle C_i|, \tag{2.45}$$

which has all its components equal to 1, as

$$\langle \sigma|\mathcal{P}^T(t) |\mathbb{P}(0)\rangle = \langle \sigma|\mathbb{P}(t)\rangle = \sum_{i=1}^{m} \mathbb{P}_{C_i}(t) = 1. \tag{2.46}$$

Since $\mathcal{P}(t)$ is stochastic, here we immediately see that

$$\langle \sigma| e^{\mathcal{Q}^T t} = \langle \sigma| \mathcal{P}^T(t) = \langle \sigma|, \tag{2.47}$$

so $\langle \sigma|$ is a left-eigenvector of $\mathcal{P}^T(t)$ with eigenvalue 1. In the same way, if we take the time derivative of $e^{\mathcal{Q}t} |\sigma\rangle$ we get $Q|\sigma\rangle = |0\rangle$. This allows us to see that

$$\langle \sigma| e^{-\mathcal{Q}^T t} = \langle \sigma| \sum_{n=0}^{\infty} (-1)^n \frac{(\mathcal{Q}^T t)^n}{n!} = \langle \sigma| \left(1 + \sum_{n=1}^{\infty} (-1)^n \frac{(\mathcal{Q}^T t)^n}{n!}\right) = \langle \sigma|. \tag{2.48}$$

[3] In the theoretical physics literature, the ME is usually written having the probability vector in ket form as $\frac{d}{dt}|P(t)\rangle = -H|P(t)\rangle$ (see Equation (2.11) in [72, p. 21]) where $-H = \mathcal{Q}^T$. To establish a clear comparison with formulas present in the physics literature, we transpose the TPM when writing ME and expectations.

Putting everything together, we can write the time-average of a configuration dependent observable as

$$\langle \mathcal{F} \rangle_t \coloneqq \sum_{i=1}^{m} F_{C_i} \mathbb{P}_{C_i}(t) = \langle \sigma | \mathcal{F} | \mathbb{P}(t) \rangle . \tag{2.49}$$

Using (2.44) and (2.48), we can collect the time dependence of the preceding expression in the operator term like

$$\langle \mathcal{F} \rangle_t = \langle \sigma | e^{-\mathcal{Q}^T t} \mathcal{F} e^{\mathcal{Q}^T t} | \mathbb{P}(0) \rangle = \langle \sigma | \mathcal{F}(t) | \mathbb{P}(0) \rangle \tag{2.50}$$

where

$$\mathcal{F}(t) \coloneqq e^{-\mathcal{Q}^T t} \mathcal{F} e^{\mathcal{Q}^T t}. \tag{2.51}$$

Contrarily to quantum mechanics, time evolution is not invertibile in stochastic processes. In other words, although $e^{-\mathcal{Q}^T t}$ is the inverse of $\mathcal{P}^T(t) = e^{\mathcal{Q}^T t}$, it is not a stochastic matrix and does not represent the backward evolution of the process.

2.2.3 Stationary Distribution

It is known that, if the HCTMC is ergodic (that is irreducible and positive-recurrent[4], see [57, p. 461]), for asymptotic times, the probability vector converges to a unique *Stationary Distribution*

$$\lim_{t\to\infty} \langle \mathbb{P}(t) | = \lim_{t\to\infty} \langle \mathbb{P}(0) | e^{\mathcal{Q}t} =: \langle \mathbb{P}^* | . \tag{2.52}$$

This implies that if we start the system in the stationary distribution, that is $\langle P(0) | = \langle \mathbb{P}^* |$, we have from (2.42)

$$\langle \mathbb{P}^* | = \langle \mathbb{P}^* | \mathcal{P}(t) , \tag{2.53}$$

so $\langle \mathbb{P}^* |$ is a left-eigenvector for $\mathcal{P}(t)$ with eigenvalue equal to 1. In this way, we can write

$$\mathcal{P}(t) = e^{\mathcal{Q}t} \to |\sigma\rangle \langle \mathbb{P}^* | \quad \text{as} \quad t \to \infty \ , \tag{2.54}$$

since trivially $\langle \mathbb{P}^* | \mathcal{P}(t) = \langle \mathbb{P}^* | \sigma \rangle \langle \mathbb{P}^* | = 1 \cdot \langle \mathbb{P}^* | = \langle \mathbb{P}^* |$[5]. Now, if we take the time derivative of the preceding equation and using (2.33), we get the *Global Balance*

[4] A state is *positive-recurrent* if its mean first passage time is finite.

[5] The existence of the stationary distribution can be seen as a consequence of the ergodicity of X_t through the Perron-Frobenius theorem. Moreover, this theorem also states that all the other eigenvalues of $\mathcal{P}(t)$ are smaller than 1 in absolute value.

Equation (GBE)

$$\frac{d\langle \mathbb{P}^*|}{dt} = \langle 0| = \frac{d\langle \mathbb{P}^*|\,\mathcal{P}(t)}{dt} = \langle \mathbb{P}^*|\,\frac{d\mathcal{P}(t)}{dt} = \langle \mathbb{P}^*|\,\mathcal{P}(t)\,\mathcal{Q} = \langle \mathbb{P}^*|\,\mathcal{Q}, \tag{2.55}$$

where $\langle 0|$ is bra-vector with null components. So, $\langle \mathbb{P}^*|$ is a left-eigenvector for $\mathcal{Q}$ with eigenvalue equal to 0. Component-wise the GBE corresponds to

$$\sum_{i=1}^{m} \mathbb{P}^*_{C_i} q_{ij} = |0\rangle_j\,, \quad \text{thus} \quad \sum_{i\neq j}^{m} \mathbb{P}^*_{C_i} q_{ij} = \mathbb{P}^*_{C_j} \sum_{i\neq j}^{m} q_{ji}\ . \tag{2.56}$$

If, in addition, $\mathbb{P}^*$ and $\mathcal{Q}$ satisfy the *Detailed Balance Equations*

$$\mathbb{P}^*_{C_i} q_{ij} = \mathbb{P}^*_{C_j} q_{ji} \quad \forall i,j\ , \tag{2.57}$$

then X_t started from $\mathbb{P}^*$ is reversible and the system described by X_t is said to be in equilibrium. Finally, to determine the mean value of an observable for large times, we can calculate directly the expectation with respect to the stationary distribution as

$$\langle \mathcal{F}(\cdot)\rangle_* \coloneqq \langle \sigma|\,\mathcal{F}\,|\mathbb{P}^*\rangle = \langle \sigma|\,\mathcal{F}(t)\,|\mathbb{P}^*\rangle\,. \tag{2.58}$$

In the end, a summary of the eigenvalues and eigenvectors related to the TPM and the generator is given in Table 2.1.

Table 2.1: Matrices, Eigenvectors and Eigenvalues for CTMC

Matrix	$\langle\ \vert$	$\vert\ \rangle$	Eigenvalue
$\mathcal{P}(t)$	$\langle \mathbb{P}^*\vert$	$\vert\sigma\rangle$	1
$\mathcal{Q}$	$\langle \mathbb{P}^*\vert$	$\vert\sigma\rangle$	0

2.2.4 Spectral Expansion of the Generator

From the master equation, we see that all the information related to the evolution of the probability vector is included within the generator of the process. The spectral expansion allows to explicit the time dependence of $\langle \mathbb{P}(t)|$ from the eigenvalues and eigenvectors of $\mathcal{Q}$. Following [57], we see this classical approach in the context of the quantum matrix form assuming non-multiplicity of the eigenvalues.

The *right-eigenvectors* and eigenvalues of $\mathcal{Q}$ are defined from the equation

$$\mathcal{Q}\,|u_i\rangle = \gamma_i\,|u_i\rangle \quad \text{with } i = 1,\ldots,m\ . \tag{2.59}$$

In the same way, we have an equivalent relation for the *left-eigenvectors*

$$\langle v_i| \mathcal{Q} = \gamma_i \langle v_i| \quad \text{with } i = 1, \dots, m \ . \tag{2.60}$$

Using the Dirac notation, we can define relevant matrices for the eigenvalue equations as

$$\mathcal{U} \coloneqq \sum_{i=1}^{m} |u_i\rangle \langle C_i| \,, \quad \Gamma \coloneqq \sum_{i=1}^{m} \gamma_i |C_i\rangle \langle C_i| \,, \quad \mathcal{V} \coloneqq \sum_{i=1}^{m} |C_i\rangle \langle v_i| \ , \tag{2.61}$$

so we have in matrix form

$$\mathcal{Q}\mathcal{U} = \mathcal{U}\Gamma \quad \text{and} \quad \mathcal{V}\mathcal{Q} = \Gamma\mathcal{V} \ . \tag{2.62}$$

We stress that the eigenvectors chosen to build the matrices $\mathcal{U}$ and $\mathcal{V}$ are arbitrary, in the sense that one can pick any eigenvector belonging to the same linear variety (that is, we have $\mathcal{Q}(c|u_i\rangle) = \gamma_i (c|u_i\rangle)$ for any coefficient $c \in \mathbb{C}$). Now, multiplying the first of (2.62) on the left by $\mathcal{V}$ and the second on the right by $\mathcal{U}$, we have that

$$(\mathcal{V}\mathcal{U})\,\Gamma = \Gamma\,(\mathcal{V}\mathcal{U}) \,, \tag{2.63}$$

which means that the matrix $(\mathcal{V}\mathcal{U})$ commutes with Γ. Moreover, since Γ is a diagonal matrix, this equation implies that $(\mathcal{V}\mathcal{U})$ is a diagonal matrix as well which means that left and right eigenvectors belonging to different eigenvalues are orthogonal [67, p. 565]. In this way, we can reduce the product of the two matrices to

$$\mathcal{V}\mathcal{U} = \sum_{i=1}^{m}\sum_{j=1}^{m} \langle v_i|u_j\rangle |C_i\rangle \langle C_j| = \sum_{i=1}^{m} \langle v_i|u_i\rangle |C_i\rangle \langle C_i| \,. \tag{2.64}$$

Since we can pick eigenvectors on a linear variety, we can define a matrix of left-eigenvectors starting from $\langle v_i|$ and $|u_i\rangle$ of the following form

$$\mathcal{W} \coloneqq \sum_{i=1}^{m} \frac{1}{\langle v_i|u_i\rangle} |C_i\rangle \langle v_i| \,. \tag{2.65}$$

This implies that, $(\mathcal{W}\mathcal{U}) = \mathcal{I}$ so $\mathcal{W} = \mathcal{U}^{-1}$ and

$$\mathcal{Q} = \mathcal{U}\Gamma\mathcal{W}. \tag{2.66}$$

Now, we can exploit the structure we have just outlined on the TPM. Using Kol-

mogorov's solution (2.35) we have

$$\mathcal{P}(t) = \mathcal{U}\Lambda(t)\mathcal{W} = \sum_{i=1}^{m} e^{\gamma_i t} \frac{|u_i\rangle \langle v_i|}{\langle v_i|u_i\rangle} \tag{2.67}$$

where $\Lambda(t) := \sum_{i=1}^{m} e^{\gamma_i t} |C_i\rangle \langle C_i|$ as result from the series expansion of the exponential matrix $e^{\mathcal{Q}t}$. In this way, equation (2.42) becomes

$$\langle \mathbb{P}(t)| = \langle \mathbb{P}(0)| \mathcal{P}(t) = \sum_{i=1}^{m} e^{\gamma_i t} \frac{\langle \mathbb{P}(0)|u_i\rangle}{\langle v_i|u_i\rangle} \langle v_i| \tag{2.68}$$

Since the TPM admits a stationary distribution, one of the $\mathcal{Q}$ eigenvalues is 0 and the others have negative real part (see (2.55)). We label the relevant eigenvectors with the subscript *zero*. We know that the right-eigenvector of $\mathcal{Q}$ with 0 eigenvalue is $|u_{zero}\rangle = |\sigma\rangle$. Hence, the preceding equation reduces to

$$\langle \mathbb{P}(t)| = \left(\frac{1}{\langle v_{zero}|\sigma\rangle}\right) \langle v_{zero}| + \sum_{i\neq j:\gamma_j=0}^{m} e^{\gamma_i t} \left(\frac{\langle \mathbb{P}(0)|u_i\rangle}{\langle v_i|u_i\rangle}\right) \langle v_i|, \tag{2.69}$$

since $\langle \mathbb{P}(0)|u_{zero}\rangle = \langle \mathbb{P}(0)|\sigma\rangle = 1$. The asymptotic behaviour of the probability vector is dominated by the eigenvalue having the minimum absolute value, that is smallest in magnitude, of the real part (subscripted with *min*)

$$\langle \mathbb{P}(t)| \approx \left(\tfrac{1}{\langle v_{zero}|\sigma\rangle}\right) \langle v_{zero}| + e^{-\mathrm{Re}(\gamma_{min})t} \left(\tfrac{\langle P(0)|u_{min}\rangle}{\langle v_{min}|u_{min}\rangle}\right) \langle v_{min}| \quad \text{for large } t\ , \tag{2.70}$$

where $[\mathrm{Re}(\gamma_{min})]^{-1}$ is also called the *characteristic relaxation time*. In the end, as time tends to infinity, the stationary distribution is given by

$$\langle \mathbb{P}^*| = \lim_{t\to\infty} \langle \mathbb{P}(t)| = \left(\frac{1}{\langle v_{zero}|\sigma\rangle}\right) \langle v_{zero}|, \tag{2.71}$$

which means that it can be determined from the eigenvalue problem related to $\mathcal{Q}$.

2.2.5 Path Integrals

Up to now, we have reviewed the algebraic structure and properties underlying HCTMC. In this section, we will see how to obtain a realization of the process starting from its generator. To begin with, we define two useful sets of times which will mark a change of state in the system and its soujourn in the new configuration.

We call the *Transition Time* (also referred to as *Jump Time*) the quantity

$$T_{n+1} = \inf\{t > T_n \,:\, X_t \neq X_{T_n}\} \quad \text{for } n > 1 \quad \text{and } T_0 = 0. \tag{2.72}$$

and the *Holding Time* (also called *Soujorn Time*)

$$\tau_n \coloneqq T_{n+1} - T_n. \tag{2.73}$$

We note that τ_n and T_{n+1} are random variables which depend on X_{T_n}. Now, starting from the definition (2.24), it is possible to express the following two properties (see, for instance, [2, p. 16] for proofs).

1. **Exponential distribution of Holding Times**
   Suppose the system is initially in a certain state $X_0 = C_i$. Then, the amount of time τ_0 the system spends in state C_i is exponentially distributed with rate parameter q_{ii}
   $$\mathbb{P}\left[\tau_0 \leqslant t | X_0 = C_i\right] = 1 - e^{q_{ii}t}. \tag{2.74}$$

2. **Markovianity of the Embedded Chain**
   The *Embedded Chain* (EC) is defined as the sequence of the states visited by the CTMC at the jump times $\{Y_n = X_{T_n} : n \in \mathbb{N}\}$. The EC is indexed using a discrete time. So, at the end of its soujourn in state C_i, the system moves to another state which is chosen with a probability equal to
   $$\mathbb{P}\left[X_{T_1} = C_j | X_0 = C_i\right] = \mathbb{P}\left[Y_1 = C_j | Y_0 = C_i\right] = -\frac{q_{ij}}{q_{ii}} \quad \text{with } i \neq j. \tag{2.75}$$

In this way, we have described a single transition of the system (see Figure 2.1). If the Markov Chain is homogenous, the evolution of the system can be continued from a new initial state $X_0 = C_j$, thus we repeat the procedure from step 1. Now, we make use of this setting. Consider a generic *Path* or *Trajectory* followed by the system, that is an ordered set of configurations and holding times, such as

$$X_{[0,T_{n+1}]} \coloneqq \left((C_i, \tau_0), (C_k, \tau_1), (C_l, \tau_2), \ldots, (C_h, \tau_{n-1}), (C_j, \tau_n)\right). \tag{2.76}$$

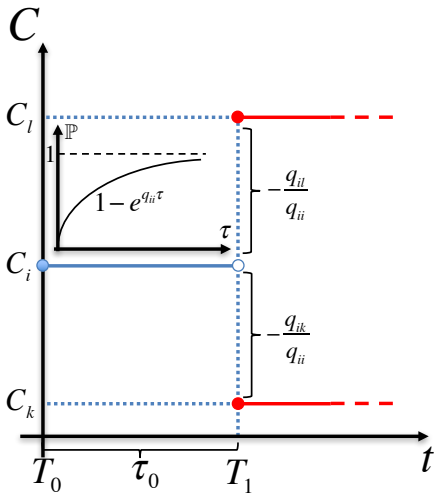

Figure 2.1: Visualization of the construction procedure for HCTMC given in (2.74) and (2.75). At the initial time T_0, the system is prepared in the state C_i and it remains in this state for a random amount of time τ_0 which is exponentially distributed with intensity q_{ii}. At the end of the holding time the system can move to its accessible states. The probability to arrive in a generic state C_k from C_i is given by $-\frac{q_{ik}}{q_{ii}}$. For clearer visualization, in the Figure only two arrival states, C_l and C_k, are depicted.

Using the construction of HCTMC, we can informally write the probability of the path (2.76) as [65]

$$\begin{aligned}\mathbb{P}\left[dX_{[0,T_{n+1}]}|X_0 = C_i\right] &= \left[(-q_{ii}e^{q_{ii}\tau_0}d\tau_0)\left(-\frac{q_{ik}}{q_{ii}}\right)\right]\left[(-q_{kk}e^{q_{kk}\tau_1}d\tau_1)\left(-\frac{q_{kl}}{q_{kk}}\right)\right] \\ &\quad \ldots\left[(-q_{hh}e^{q_{hh}\tau_n}d\tau_n)\left(-\frac{q_{hj}}{q_{hh}}\right)\right] \qquad (2.77)\\ &= (e^{q_{ii}\tau_0}d\tau_0)\, q_{ik}\, (e^{q_{kk}\tau_1}d\tau_1)\, q_{kl} \ldots (e^{q_{hh}\tau_n}d\tau_n)\, q_{hj}. \qquad (2.78)\end{aligned}$$

If the initial state of the system is distributed according to $\mathbb{P}(0)$, we write

$$\mathbb{P}\left[dX_{[0,T_{n+1}]}\right] = \sum_{i=1}^{m} \mathbb{P}\left[dX_{[0,T_{n+1}]}|X_0 = C_i\right]\mathbb{P}_{C_i}(0)\,. \qquad (2.79)$$

In this way, the elements of the TPM can be written as

$$\langle C_i|\,\mathcal{P}(t)\,|C_j\rangle = \mathbb{P}\left[X_t = C_j|X_0 = C_i\right] = \int_{D(C_i,C_j)} \mathbb{P}\left[dX_{[0,t]}|X_0 = C_i\right], \qquad (2.80)$$

where $D(C_i, C_j)$ is the set of all paths starting at C_i and ending at C_j at time t [16, p. 23] [89]. This connection with the TPM allows us to understand the following

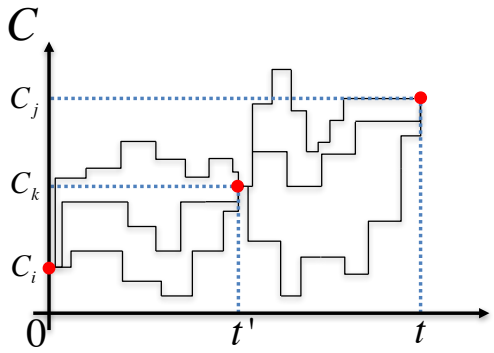

Figure 2.2: Visualization of the probability path integral given in given in (2.85) considering all the trajectories passing, in order, through the points $(0, C_i)$, (t', C_k) and (t, C_j).

normalizations

$$\sum_{j=1}^{m} \int_{D(C_i,C_j)} \mathbb{P}\left[dX_{[0,t]} | X_0 = C_i\right] = \langle\sigma|\, \mathcal{P}^T(t)\, |C_i\rangle = 1, \tag{2.81}$$

which follows from the TPM being stochastic, and

$$\langle\sigma|\, e^{\mathcal{Q}^T t}\, |\mathbb{P}(0)\rangle = \sum_{j=1}^{m}\sum_{i=1}^{m} \int_{D(C_i,C_j)} \mathbb{P}\left[dX_{[0,t]}\right] = \int_D \mathbb{P}\left[dX_{[0,t]}\right] = 1, \tag{2.82}$$

where D is the set of all possible trajectories from 0 up to time t. Since paths are given in terms of products of transition rates and exponentials, for HCTMC we can combine a transition among three configurations as the product of two paths (see Figure 2.2)

$$\mathbb{P}\left[X_{t'} = C_k | X_0 = C_i\right] \mathbb{P}\left[X_t = C_j | X_{t'} = C_k\right] \tag{2.83}$$

$$= \mathbb{P}\left[X_{t'} = C_k | X_0 = C_i\right] \mathbb{P}\left[X_{t-t'} = C_j | X_0 = C_k\right] \tag{2.84}$$

$$= \langle C_i|\, e^{\mathcal{Q}t'}\, |C_k\rangle \langle C_k|\, e^{\mathcal{Q}(t-t')}\, |C_j\rangle \tag{2.85}$$

In the end, given a function of the paths $f : D \to \mathbb{R}$, this framework allows us to write the expectation on the path space distribution as

$$\mathbb{E}_t[f] = \int_D f\left[X_{[0,t]}\right] \mathbb{P}\left[dX_{[0,t]}\right]. \tag{2.86}$$

CHAPTER 3

Stochastic Particle Systems

In this chapter, we will describe a class of *Stochastic Particle Systems* (SPS) which locally conserve the number of particles. In the first place, we will give a heuristic description of the structure of SPS. Afterwards, by applying the quantum formalism for MC, we will see how SPS can be understood from the point of view of many-body quantum systems. We will also specify the main observables for SPS, which are density and current, and their related quantities. In particular, we will focus on two models which are the ZRP and IP. We will also define the NESS regime which will be the central interest of the present thesis.

3.1 Heuristic Introduction to SPS

Consider a finite lattice Λ, with $|\Lambda| = L \in \mathbb{N}$ being the number of different sites and x the index moving through the sites, that is $x = 1, ..., L$. Each site can be occupied by any finite number of particles. We label the number of particles on the generic site x as $\eta_x \in \mathbb{N}$. A *configuration* or *state* of the system is given by the vector

$$\eta \coloneqq (\eta_1, \eta_2, ..., \eta_x, ..., \eta_L) \in \Omega \coloneqq \mathbb{N}^L, \tag{3.1}$$

which specifies the number of particles present on each site. Ω is called the *configuration* or *state space*. The particles in the system are allowed to jump between two sites which are connected by lattice links. In the present work, we will consider only jumps between nearest-neighbouring sites on one dimensional lattices. In general, a particle jump corresponds to a change in the system configuration $\eta \to \eta'$. Since only nearest-neighbour jumps are considered, we can keep track of the particle movement in the configuration labelling as

$$\eta^{x,x+1} \coloneqq (\eta_1, \eta_2, ..., \eta_x - 1, \eta_{x+1} + 1, ..., \eta_L)\,, \tag{3.2}$$

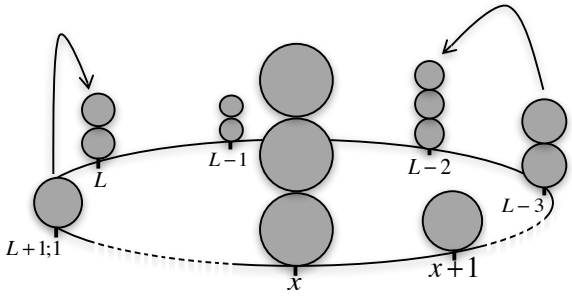

Figure 3.1: Generic particle system on a ring. The arrows represent possible transitions from one site to another. As can be seen from the arrow directions, particles can jump to the right and to the left.

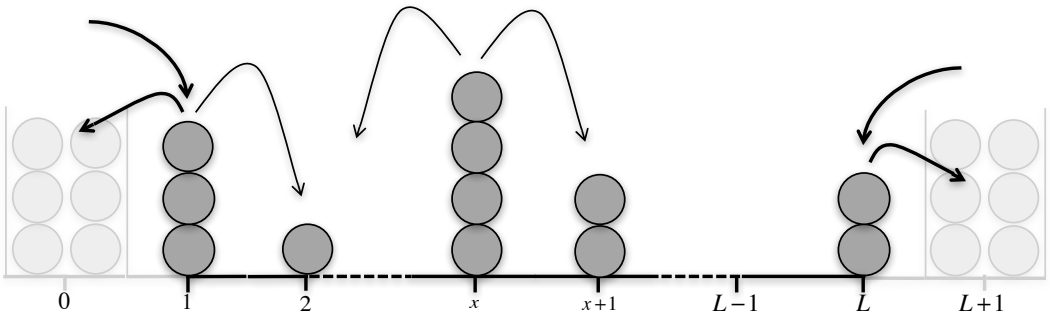

Figure 3.2: Generic particle system in contact with boundary reservoirs. The arrows connecting the bulk of the system with sites 0 and $L+1$ are drawn bold since the jump rates may have a different structure when the departure or arrival site coincide with the reservoirs.

for a particle moving from site x to $x+1$, and

$$\eta^{x,x-1} \coloneqq (\eta_1, \eta_2, ..., \eta_{x-1}+1, \eta_x - 1, ..., \eta_L)\,, \tag{3.3}$$

for a particle moving backwards. In our analysis, we will consider two classes of one-dimensional lattices. For the first type, particles lie on a *ring* (see Figure 3.1), that is the lattice has *periodic boundary conditions* (sites 1 and L are linked or, in other words, sites 1 and $L+1$ coincide). For the second type, the system has *open boundaries*, that is sites 1 and L are linked to particle reservoirs which can influence the system behaviour in many ways which will be specified later (see Figure 3.2). In the latter case, the number of particles is not in general a conserved quantity.

The dynamics of the systems can be described as follows. First, particles

are allowed to move to the right and to the left with probabilities dependent on the system configuration. Second, in SPS time is a continuos variable and the particle jump times follow a probability distribution function (p.d.f.) which is exponential with rate parameter $c(\eta)$. Due to the nearest-neighbour interaction condition, the total rate at which the configuration changes has the following form

$$c(\eta) \coloneqq \sum_{x=1}^{L} g_r(x,\eta) + g_l(x,\eta), \tag{3.4}$$

where g_r and g_l are real valued functions called *jump rates* (the subscripts r and l standing for *right* and *left*, respectively). In particular, we will consider

$$g_r(x,\eta) \coloneqq pu(\eta_x)\, v(\eta_{x+1}) \quad \text{and} \quad g_l(x,\eta) \coloneqq qu(\eta_x)\, v(\eta_{x-1}), \tag{3.5}$$

where

- $p \in [0,1]$ and $q \coloneqq 1-p$ are usually referred to as the spatial part of the jump rates,
- $u : \mathbb{N} \to [0,\infty)$ is function of the number of particles of the departure site. We assume that $u(\eta_x) = 0$ iff $\eta_x = 0$, which means that no jump occurs if site x is empty, and
- $v : \mathbb{N} \to [0,\infty)$ depends on the number of particles of the arrival site. We fix $v(\eta_x) > 0 \, \forall \eta_x \geqslant 0$ and $v(0) = 1$ as a normalization.

In the end, under certain regularity assumptions on the rates, SPS on finite lattices can be considered as CTMC (see Figure 2.1). The formal construction in more general cases revolves around using techniques such as the *Hille-Yosida* theorem which, through the concept of semigroups, links an operator defined from the jump rates, called *generator*, to Markov processes. This makes the evolution of SPS well defined whenever the local state space is compact and the jump rates are bounded [85, 63]. One of the reasons which makes this construction necessary lies in the fact that, for general SPS the lattice can coincide with $\mathbb{Z}$ so the number of particles can be infinite, thus, for any time interval, infinitely many particles can jump. Moreover, the jump rates can depend on the entire configuration. However, for the closed ring geometry the lattice is finite and the number of particles can be fixed to be finite since there is no exchange of particles with any external systems. In this case, the state space is finite, so the usual construction of CTMC, which can be found in standard theory textbooks (see [57]), can be used. When the system is contact

with reservoirs, the number of particles in the system fluctuates and is a priori unbounded. Hence, the state space is countably infinite. In Section 2.2, we will recall the construction of CTMC for finite state space and we will see how to extend this structure to the open boundary case in the following sections. In particular, we will look at the behaviour of the system for asymptotic times, that is for $t \to \infty$, and for stationary distributions.

It should be noted that the system behaviour is specified only through the jump rates, which modify the value of a discrete variable (particle number) of an ordered set (lattice sites). In SPS there is no energy, in the physical sense, which can be a priori associated to a system configuration and the particle number can represent any discrete additive quantity (like mass, electric charge etc) [65, p. 30]. The description in terms of jumping particles is just a useful graphical representation. Notwithstanding, SPS turns out to be useful in the study of real physical phenomena [34, 12] and complex systems [21, 15, 58]. They represent situations where the motion of particles is activated by an external energy source (e.g. thermal, electric field etc) which is not explicitely included in the model.

3.2 SPS via Quantum Formalism

In the previous sections we have outlined the Dirac notation for linear algebra and the quantum matrix form for CTMC. In this section, we will see how to use this framework in the context of SPS. We will begin with a presentation of the theory for a simple model to highlight how it works and then how it adapts for general SPS (see [72] for a general self-contained description). Here, we will also see how the generator can be written in terms of local creation and annihiliation operators, which is a formulation originally developed in MBQT.

3.2.1 Quantum Formulation for a Toy Model

Consider a discrete lattice made up of two sites only which follow the *exclusion rule*, that is each site can be allocated either zero or one particle. We represent the two possible states of a site as[1]

$$|\epsilon_\circ) := \begin{pmatrix} 1 \\ 0 \end{pmatrix} \quad \text{and} \quad |\epsilon_\bullet) := \begin{pmatrix} 0 \\ 1 \end{pmatrix} , \tag{3.6}$$

[1]Here we write vectors in ket version as used in the physics literature.

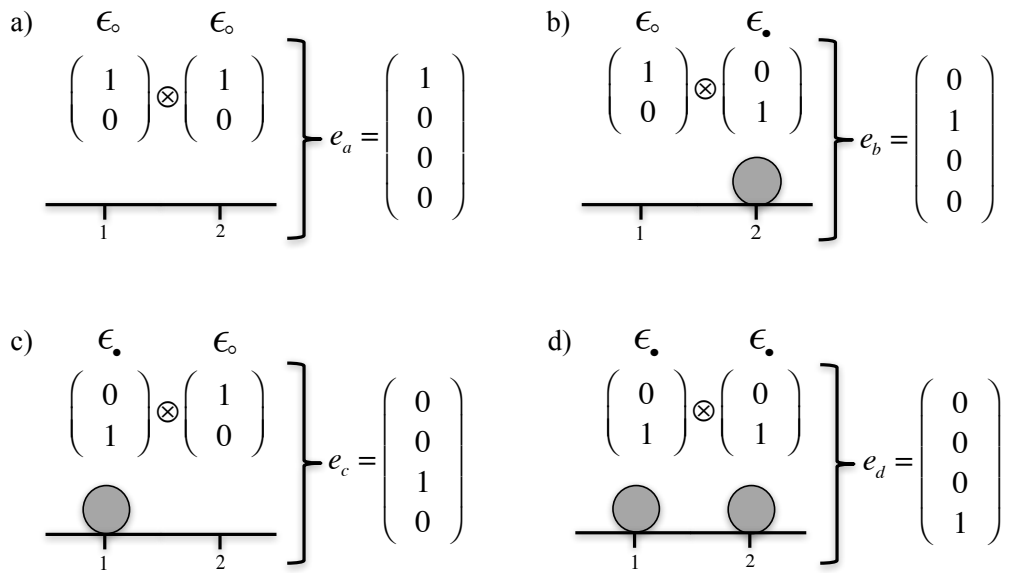

Figure 3.3: All the admissible configurations, and their vectorial representations, of a two-sites lattice subject to the exclusion rule.

where $|\epsilon_\circ)$ and $|\epsilon_\bullet)$[2] identify an empty and occupied site, respectively (here and in the following, we use curve brackets $|\,)$ for site configurations and angular ones $|\,\rangle$ for system configurations). The two vectors together constitute the canonical basis for $\mathbb{C}^2$, which we refer to as $\mathcal{E} \coloneqq \{|\epsilon_\circ), |\epsilon_\bullet)\}$. Here, we notice that the length of the basis vectors is equal to the number of possible states of a site, which corresponds to the maximum possible number of particles which a site can accomodate plus one (corresponding to the empty configuration).

We can build vectors representing the state of the whole system from the site states using the tensor products. This relies on the fact that the tensor product is non-commutative. Thus, all the possible vectors which can be obtained by applying the tensor product between the elements of $\mathcal{E}$ are four and they constitute the canonical basis of $\mathbb{C}^4$, which we refer to as $E \coloneqq \{|e_a\rangle, |e_b\rangle, |e_c\rangle, |e_d\rangle\}$ (see Figure 3.3). For instance, we have that $|e_c\rangle = |\epsilon_\bullet) \otimes |\epsilon_\circ)$. In this way, each state of the system as a whole has a unique representation in E. In this case, the length of the basis vectors corresponds to the number of possible configurations of the system. As we have seen in Section 2.2.2, the summation and probability vectors are given

[2]The pictures in the subscripts relate directly to the empty and occupied sites configurations. We avoid to use $|0)$ and $|1)$ to label configurations because in the literature the former is typically used to indicate a ground state configuration or a vector with null entries and the latter for a vector with entries all equal 1.

as

$$|\sigma\rangle = \sum_{e\in E} |e\rangle = \begin{pmatrix} 1 \\ 1 \\ 1 \\ 1 \end{pmatrix} \quad \text{and} \quad |P(t)\rangle = \sum_{e\in E} P_e(t)\,|e\rangle = \begin{pmatrix} P_{e_a}(t) \\ P_{e_b}(t) \\ P_{e_c}(t) \\ P_{e_d}(t) \end{pmatrix} , \quad (3.7)$$

where $P_e(t)$ is the probability of finding the system in state e at time t.

The basic events in an SPS consist of a particle jumping from one site to another, which corresponds to a change in the state of both sites. This action can be split in two steps: the removal (*annihilation* in MBQT language) of the particle from the departure site and its placement (*creation*) on the arrival site. Also the creation or annihilation events alone can be thought as a two-steps procedure: one site is left identitical and on the other a particle is either created or annihilated. All these situations can be represented as the application of suitable defined square matrices to the vectors associated to the site states. For the toy model considered, the identity, annihilation and creation matrices are defined as

$$\mathcal{I} = \begin{pmatrix} 1 & 0 \\ 0 & 1 \end{pmatrix} \in \mathcal{M}^2 \quad ; \quad \mathcal{A} \coloneqq \begin{pmatrix} 0 & 1 \\ 0 & 0 \end{pmatrix} \in \mathcal{M}^2 \quad ; \quad \mathcal{C} \coloneqq \begin{pmatrix} 0 & 0 \\ 1 & 0 \end{pmatrix} \in \mathcal{M}^2.$$

For example, the annihilation of a particle on a site is given by $|\epsilon_\circ) = \mathcal{A}\,|\epsilon_\bullet)$. Moreover, we define the following matrices

$$\mathcal{M} \coloneqq \begin{pmatrix} 1 & 0 \\ 0 & 0 \end{pmatrix} \quad , \quad \mathcal{N} \coloneqq \begin{pmatrix} 0 & 0 \\ 0 & 1 \end{pmatrix} \quad (3.8)$$

which will shortly be used to write the generator of the process in block form. As we did for site vectors, we can build operators acting on the whole system, that is on the elements of E, as a tensor product of site matrices. For the model considered, the matrices

$$\hat{a}_1 = \mathcal{A} \otimes \mathcal{I} = \begin{pmatrix} 0 & \mathcal{I} \\ 0 & 0 \end{pmatrix} \in \mathcal{M}^4 \quad ; \quad \hat{a}_2 = \mathcal{I} \otimes \mathcal{A} = \begin{pmatrix} \mathcal{A} & 0 \\ 0 & \mathcal{A} \end{pmatrix} \in \mathcal{M}^4 \ ,$$

describe the annihilation of a particle on the first and second site, respectively, while

$$\hat{c}_1 \coloneqq \mathcal{C} \otimes \mathcal{I} = \begin{pmatrix} 0 & 0 \\ \mathcal{I} & 0 \end{pmatrix} \in \mathcal{M}^4 \quad ; \quad \hat{c}_2 \coloneqq \mathcal{I} \otimes \mathcal{C} = \begin{pmatrix} \mathcal{C} & 0 \\ 0 & \mathcal{C} \end{pmatrix} \in \mathcal{M}^4 \ ,$$

are the corresponding creation matrices. So, for example we have that $|e_c\rangle =$

$\hat{a}_2 |e_d\rangle = \hat{c}_1 |e_a\rangle = \hat{c}_1 \hat{a}_2 |e_b\rangle$. The identity matrix for the system configuration is simply

$$\mathbf{1} \coloneqq \mathcal{I} \otimes \mathcal{I} = \begin{pmatrix} \mathcal{I} & 0 \\ 0 & \mathcal{I} \end{pmatrix}. \tag{3.9}$$

Moreover, we introduce a matrix which acts in a similar way to a logical operator on the system sites: it returns a $|0\rangle$ if the site is empty and the original configuration $|\eta\rangle$ if there is one particle on it. The explicit expression is given by

$$\hat{\eta}_1 \coloneqq \mathcal{N} \otimes \mathcal{I} = \begin{pmatrix} 0 & 0 \\ 0 & \mathcal{I} \end{pmatrix} \quad \text{and} \quad \hat{\eta}_2 \coloneqq \mathcal{I} \otimes \mathcal{N} = \begin{pmatrix} \mathcal{N} & 0 \\ 0 & \mathcal{N} \end{pmatrix}, \tag{3.10}$$

for its action on the first and second site, respectively. In terms of the dynamics of the process, we see that the setting chosen only allows transition from state b to c and vice versa. For this reason the generator of the process reduces to

$$\mathcal{Q}^T = \begin{pmatrix} q_{aa} & q_{ab} & q_{ac} & q_{ad} \\ q_{ba} & q_{bb} & q_{bc} & q_{bd} \\ q_{ca} & q_{cb} & q_{cc} & q_{cd} \\ q_{da} & q_{db} & q_{dc} & q_{dd} \end{pmatrix}^T = \begin{pmatrix} 0 & 0 & 0 & 0 \\ 0 & -q_{bc} & q_{cb} & 0 \\ 0 & q_{bc} & -q_{cb} & 0 \\ 0 & 0 & 0 & 0 \end{pmatrix}, \tag{3.11}$$

which in block form is equivalent to

$$\mathcal{Q}^T = q_{bc} \left[\begin{pmatrix} 0 & 0 \\ \mathcal{A} & 0 \end{pmatrix} - \begin{pmatrix} \mathcal{N} & 0 \\ 0 & 0 \end{pmatrix} \right] + q_{cb} \left[\begin{pmatrix} 0 & \mathcal{C} \\ 0 & 0 \end{pmatrix} - \begin{pmatrix} 0 & 0 \\ 0 & \mathcal{M} \end{pmatrix} \right], \tag{3.12}$$

and in terms of operators

$$\mathcal{Q}^T = q_{bc} \left[\hat{c}_1 \hat{a}_2 - (\mathbf{1} - \hat{\eta}_1) \hat{\eta}_2 \right] + q_{cb} \left(\hat{c}_2 \hat{a}_1 - (\mathbf{1} - \hat{\eta}_2) \hat{\eta}_1 \right). \tag{3.13}$$

The preceding equation corresponds to the expression for the quantum Hamiltonian of the ASEP which can be found in [72, p. 43] Equation (3.28). In the end, we notice that the aforementioned matrices have a synthetic definition in the Dirac notation as

$$\mathcal{M} = |\epsilon_\circ\rangle (\epsilon_\circ| \quad , \quad \mathcal{A} = |\epsilon_\circ\rangle (\epsilon_\bullet| \quad , \quad \mathcal{C} = |\epsilon_\bullet\rangle (\epsilon_\circ| \quad , \quad \mathcal{N} = |\epsilon_\bullet\rangle (\epsilon_\bullet| \ . \tag{3.14}$$

So, the generator can also be written as (see Equation (2.4) in [48])

$$\mathcal{Q}^T = q_{bc} \left(|e_c\rangle \langle e_b| - |e_b\rangle \langle e_b| \right) + q_{cb} \left(|e_b\rangle \langle e_c| - |e_c\rangle \langle e_c| \right). \tag{3.15}$$

3.2.2 General Characterization

Up to now, we have described CTMC with finite state space. However, in the following, we will consider a possibly countable infinite state space in order to have a framework suitable for the open boundary case as well. The previous representation with finite matrices was purely for illustration and we switch to a more abstract description from now on.

3.2.2.1 Vectors

Consider a discrete lattice made up of L sites which can allocate any number of particles. Following [47], we indicate the state of a site, which is identified by the number of particles on it, with the vector

$$|\eta_x) \in \mathbb{C}^\infty, \tag{3.16}$$

since the possible number of particles per site is now unbounded[3]. The state of the system is given by the tensor product of site vectors

$$|\eta\rangle = |\eta_1) \otimes |\eta_2) \otimes ... \otimes |\eta_L) \in \Omega \coloneqq (\mathbb{C}^\infty)^{\otimes L}\,, \tag{3.17}$$

which forms a canonical basis for the space Ω. In this place, the dual pairing product of two system configurations ζ and η is denoted by

$$\langle\zeta|\eta\rangle = \begin{cases} 1 & \text{if } \zeta_i = \eta_i \forall i \\ 0 & \text{otherwise} \end{cases} =: \delta_{\zeta,\eta}. \tag{3.18}$$

In a similar way as in Section 3.1, the configurations obtained after a particle jump are expressed as

$$\left|\eta^{+x}\right\rangle \coloneqq |\eta_1, \eta_2, ..., \eta_x + 1, ..., \eta_L\rangle\,, \tag{3.19}$$

and

$$\left|\eta^{-x}\right\rangle \coloneqq |\eta_1, \eta_2, ..., \eta_x - 1, ..., \eta_L\rangle\,. \tag{3.20}$$

Also in this context, the summation and probability vectors are sums on the canonical basis elements as

$$|\sigma_N\rangle = \textstyle\sum_{\eta\in\Omega} |\eta\rangle \quad \text{and} \quad |\mathbb{P}_N(t)\rangle = \sum_{\eta\in\Omega} \mathbb{P}_\eta(t)\,|\eta\rangle\ , \tag{3.21}$$

[3] In analogy with Equation (3.6), the general form of the vector is, for example, $|\eta_x) = \begin{pmatrix} 0 & \dots & 0 & 1 & 0 & \dots \end{pmatrix}^T$ where the position of 1 indicates the number of particles on the site.

where $\mathbb{P}_\eta(t) = \langle\eta|\mathbb{P}(t)\rangle$ is the probability of finding the system in state η at time t. We stress that the vector $|0\rangle$ indicates that all its components are null and is different from $|0,0,...,0\rangle$ which referes to a system with no particles.

3.2.2.2 Operators

Operators are used to modify the states according to the dynamical rules involved in the time evolution of an SPS. In this section, we define all the operators involved in the definition of the master equation by specifing how they modify the system state, i.e. act on basis vectors. The first operator we define is the *identity operator*

$$\hat{I}|\eta\rangle \coloneqq |\eta\rangle \quad \text{with} \quad \hat{I} = \textstyle\sum_\eta |\eta\rangle\langle\eta| \ . \tag{3.22}$$

In this context, also the jump rates are understood in an operator form simply as

$$\hat{u}_x|\eta\rangle = u(\eta_x)|\eta\rangle \quad ; \quad \hat{v}_x|\eta\rangle = v(\eta_x)|\eta\rangle \ . \tag{3.23}$$

The creation and annihilation operators are non-diagonal since they modify the system state by moving a particle on the lattice. They are defined as

$$\hat{c}_x|\eta\rangle \coloneqq |\eta^{+x}\rangle \quad ; \quad \hat{a}_x|\eta\rangle \coloneqq \begin{cases} |0\rangle & \text{if } \eta_x = 0 \\ |\eta^{-x}\rangle & \text{if } \eta_x > 0. \end{cases} \tag{3.24}$$

Since the number of particles is locally conserved, the creation and annihilation operators will always appear together but acting on different sites which are the arrival and departure one, respectively. To take into account jump rates depending on multiple sites, for which no standard convention in the quantum notation exists so far, we have not included the jump rates in the definition of the annihilation operators (as used instead for the ZRP, see e.g. Equation 4 in [51, p. 6]). In this way, we can avoid to define different annihilation operators for each occupation number of the target site and multiple-sites dependence can be included in a consistent way. With this choice, the usual commutator rule for particle creation and annihilation operators is recovered as

$$[\hat{a}_x\hat{u}_x\hat{v}_y, \hat{c}_z] = \hat{a}_x\hat{u}_x[\hat{v}_y, \hat{c}_z] + \hat{a}_x[\hat{u}_x, \hat{c}_z]\hat{v}_y + [\hat{a}_x, \hat{c}_z]\hat{u}_x\hat{v}_y \tag{3.25}$$

$$= \begin{cases} 0 & z \neq x,\ z \neq y,\ y \neq x \\ (u(\eta_x+1) - u(\eta_x))\, v(\eta_y) & z = x,\ y \neq x \\ u(\eta_x)\,(v(\eta_y+1) - v(\eta_y)) & z = y,\ y \neq x \end{cases} \ . \tag{3.26}$$

Another common operator is the particle number, which is defined as

$$\hat{N}_x \left|\eta\right\rangle = \eta_x \left|\eta\right\rangle . \tag{3.27}$$

3.2.3 Stationary State

As we have seen in Section 2.2.4, the asymptotic behaviour of a HCTMC is dominated by the stationary distribution. For the choice of transition rates in (3.5), it is known (see [19]) that provided the condition

$$u\left(n\right) v\left(m\right) - u\left(m\right) v\left(n\right) = u\left(n\right) - u\left(m\right) \quad \forall n, m \geqslant 0 \tag{3.28}$$

the probability of observing the system in state η in the stationary regime is given by

$$\mathbb{P}^*_\eta \coloneqq \prod_{x\in\Lambda} \mathbb{P}^*_{\eta_x} \coloneqq \prod_{x\in\Lambda} \left[\frac{1}{z\left(\phi\right)} w\left(\eta_x\right) \phi^{\eta_x}\right] \tag{3.29}$$

where

- $w\left(\eta_x\right) \coloneqq \prod_{k=1}^{\eta_x} \frac{v(k-1)}{u(k)}$ with $w\left(0\right) = 1$,
- ϕ is a real parameter called *fugacity* which, as we will see later in (3.55), is fixed through the density,
- $z\left(\phi\right) \coloneqq \sum_{n=0}^{\infty} w\left(n\right) \phi^n$, with radius of convergence

$$\phi_c = \left[\limsup_{n\to\infty} \left(w\left(n\right)\right)^{\frac{1}{n}}\right]^{-1}, \tag{3.30}$$

  is the *partition function*. Distributions (3.29) are well defined for all $\phi < \phi_c$, possibly also for $\phi = \phi_c$.

It turns out that the condition (3.28) fixes a constraint on the arrival jump rate which has to assume the form

$$v\left(n\right) = Cu\left(n\right) + v\left(0\right) \tag{3.31}$$

with C being an arbitrary constant and $v\left(0\right) = 1$. With (3.29), we can build probability vectors as

$$\left|\mathbb{P}^*\right\rangle \coloneqq \sum_{\eta\in\Omega} \mathbb{P}^*_\eta \left|\eta\right\rangle . \tag{3.32}$$

One of the most important properties of (3.29) is site factorizability. This allows to simplify a bit the notation

$$\begin{aligned}|\mathbb{P}^*\rangle =& \sum_{\eta\in\Omega}\prod_{x\in\Lambda}\mathbb{P}^*_{\eta_x}|\eta\rangle = \sum_{\eta\in\Omega}\mathbb{P}^*_{\eta_1}|\eta_1)\otimes\mathbb{P}^*_{\eta_2}|\eta_2)\otimes\ldots\otimes\mathbb{P}^*_{\eta_L}|\eta_L)\\ =& \sum_{\eta\in\Omega}\left|\mathbb{P}^*_{\eta_1}\right)\otimes\left|\mathbb{P}^*_{\eta_2}\right)\otimes\ldots\otimes\left|\mathbb{P}^*_{\eta_L}\right) = |\mathbb{P}^*_1)\otimes|\mathbb{P}^*_2)\otimes\ldots\otimes|\mathbb{P}^*_L)\\ =& |\mathbb{P}^*_1,\mathbb{P}^*_2,\ldots,\mathbb{P}^*_L\rangle \end{aligned} \tag{3.33}$$

where $|\mathbb{P}^*_x) = \sum_{k=0}^{\infty}\mathbb{P}^*_{\eta_k}|k)$ independently of x. The expectation of a local observable $F(\eta_x)$ with respect to the stationary measure is defined as

$$\langle F\rangle_* \coloneqq \frac{1}{z(\phi)}\sum_{n=0}^{\infty}F(n)\,w(n)\,\phi^n. \tag{3.34}$$

With this definition, as shown in Appendix A, we notice the important relation among the jump rates

$$\langle v\rangle_* = \frac{\langle u\rangle_*}{\phi}. \tag{3.35}$$

On the side of the generators, for the ring geometry the dynamics of the system is described by the following combination of operators

$$\begin{aligned}\mathcal{Q}^T = \hat{M}^N_{ring} \coloneqq& p\sum_{x=1}^{L}\left[\hat{c}_{x+1}\hat{a}_x\left(\hat{u}_x\hat{v}_{x+1}\right)-\hat{u}_x\hat{v}_{x+1}\right]\\ &+q\sum_{x=1}^{L}\left[\hat{c}_x\hat{a}_{x+1}\left(\hat{u}_{x+1}\hat{v}_x\right)-\hat{u}_{x+1}\hat{v}_x\right].\end{aligned} \tag{3.36}$$

where $L+1$ and 1 are the same site. For the open boundary case, we need to consider operators which take into account the presence of the reservoirs. For our purposes we define

$$\hat{\alpha}^r_1|\eta\rangle \coloneqq \langle u\rangle_\phi\,\hat{v}_1|\eta\rangle, \tag{3.37}$$

$$\hat{\beta}^r_L|\eta\rangle \coloneqq \hat{u}_L\langle v\rangle_\phi|\eta\rangle, \tag{3.38}$$

$$\hat{\alpha}^l_L|\eta\rangle \coloneqq \langle u\rangle_\phi\,\hat{v}_L|\eta\rangle, \tag{3.39}$$

$$\hat{\beta}^l_1|\eta\rangle \coloneqq \hat{u}_1\langle v\rangle_\phi|\eta\rangle. \tag{3.40}$$

In this way, the expression of the generator in terms of creation and annihilation operators for the open boundaries case is

$$\begin{aligned}\hat{M}_{OB}^{N} \coloneqq & p\left(\hat{c}_1\hat{\alpha}_1^r - \hat{\alpha}_1^r\right) + p\sum_{x=1}^{L-1}\left[\hat{c}_{x+1}\hat{a}_x\left(\hat{u}_x\hat{v}_{x+1}\right) - \hat{u}_x\hat{v}_{x+1}\right] + p\left(\hat{a}_L\hat{\beta}_L^r - \hat{\beta}_L^r\right) \\ & + q\left(\hat{a}_1\hat{\beta}_1^l - \hat{\beta}_1^l\right) + q\sum_{x=1}^{L-1}\left[\hat{c}_x\hat{a}_{x+1}\left(\hat{u}_{x+1}\hat{v}_x\right) - \hat{u}_{x+1}\hat{v}_x\right] + q\left(\hat{c}_L\hat{\alpha}_L^l - \hat{\alpha}_L^l\right).\end{aligned} \tag{3.41}$$

As we will show in the Appendix A, the special form of $\hat{\alpha}_1^r$, $\hat{\beta}_L^r$, $\hat{\alpha}_L^l$ and $\hat{\beta}_1^l$ implies that $\hat{M}_{OB}^{N}\left|\mathbb{P}^*\right\rangle = \left|0\right\rangle$ for general $u\left(\eta_x\right)$ and $v\left(\eta_x\right)$. Later we will see that when $v\left(\eta_x\right) = 1$ for all η_x, the jump rates from and to the reservoirs can have a more general form. For the periodic boundary case we have that $\hat{M}_{ring}^{N}\left|\mathbb{P}^*\right\rangle = \left|0\right\rangle$ as well. In the stationary state, calculations are greatly simplified due to the following properties (which are proved in the Appendix A)

- **Bulk creation and annihilation operators**

$$\hat{c}_x\hat{v}_x\left|\mathbb{P}^*\right\rangle = \phi^{-1}\hat{u}_x\left|\mathbb{P}^*\right\rangle \;\; \forall x \in \Lambda \tag{3.42}$$

$$\hat{a}_x\hat{u}_x\left|\mathbb{P}^*\right\rangle = \phi\hat{v}_x\left|\mathbb{P}^*\right\rangle \;\; \forall x \in \Lambda \tag{3.43}$$

- **Boundaries creation and annihilation operators**

$$\hat{c}_x\hat{\alpha}_x\left|\mathbb{P}^*\right\rangle = \phi^{-1}\left\langle u\right\rangle_\phi\hat{u}_x\left|\mathbb{P}^*\right\rangle \;\; \forall x \in \Delta \tag{3.44}$$

$$\hat{a}_x\hat{\beta}_x\left|\mathbb{P}^*\right\rangle = \phi\left\langle v\right\rangle_\phi\hat{v}_x\left|\mathbb{P}^*\right\rangle \;\; \forall x \in \Delta \tag{3.45}$$

In the mathematical literature, particular SPS are usually specified using a suitably defined operator called the generator [64]. Here we give a short comparison among the functional analysis and the quantum operators description. For simplicity, we will look at the case of totally asymmetric dynamics on a ring. With this constraint the functional analysis version of the generator is usually given as

$$\mathcal{L}\left[f\right]\left(\eta\right) = \sum_{x=1}^{L} u\left(\eta_x\right) v\left(\eta_{x+1}\right)\left[f\left(\eta^{x,x+1}\right) - f\left(\eta\right)\right], \tag{3.46}$$

where $f : \Omega \to \mathbb{R}$, while in the quantum notation we have

$$\hat{M} = \sum_{x=1}^{L}\left[\hat{c}_{x+1}\hat{a}_x\left(\hat{u}_x\hat{v}_{x+1}\right) - \hat{u}_x\hat{v}_{x+1}\right]. \tag{3.47}$$

Since the configuration space is countable, we can define the function f in vectorial representation as $\langle f| = \sum_{\eta\in\Omega} f(\eta)\langle\eta|$. In this way, we have

$$\begin{aligned}\langle f|\hat{M}|\eta\rangle &= \langle f|\left(\sum_{x=1}^{L}\hat{c}_{x+1}\hat{a}_x\left(\hat{u}_x\hat{v}_{x+1}\right)|\eta\rangle - \hat{u}_x\hat{v}_{x+1}|\eta\rangle\right)\\ &= \langle f|\left(\sum_{x=1}^{L}u(\eta_x)\,v(\eta_{x+1})\left|\eta^{x,x+1}\right\rangle - u(\eta_x)\,v(\eta_{x+1})|\eta\rangle\right)\\ &= \sum_{x=1}^{L}u(\eta_x)\,v(\eta_{x+1})\left\langle f|\eta^{x,x+1}\right\rangle - u(\eta_x)\,v(\eta_{x+1})\langle f|\eta\rangle\\ &= \sum_{x=1}^{L}u(\eta_x)\,v(\eta_{x+1})\left[f\left(\eta^{x,x+1}\right) - f(\eta)\right], \end{aligned} \tag{3.48}$$

where the last equality follows from the fact that the configuration space is orthonormal, so that $\langle f|\eta\rangle = f(\eta)$ for all $\eta\in\Omega$. In the end, $\mathcal{L}[f](\eta)$ in (3.46) is simply given by a matrix element of the operator $\hat{M}$.

3.2.4 Observables

The two most important quantities describing the mechanical behaviour of a SPS are *density* and *current*, which can be characterized in many different ways. In fact, both have a global and local description in terms of space or time. Moreover, these two quantities have specific expressions in the stationary regime as we will show in the next sections.

3.2.4.1 Density

We indicate the number of particles at a given time t and site x as

$$\eta_x(t)\in\mathbb{N}. \tag{3.49}$$

Sometimes, $\eta_x(t)$ is referred to as the *empirical local density*. Since $\eta_x(t)$ varies on the system sites, this change can be pictured as a profile which evolves in time (see Figure 3.4). In this way, the amount of particles present in the system bulk at a given time is $N(t) \coloneqq \sum_{x=1}^{L}\eta_x(t)$. In the case of the ring geometry, the number of particles in the system N is constant, so the *global density* defined as

$$\rho \coloneqq \frac{N}{L}\in\mathbb{R}^+ \tag{3.50}$$

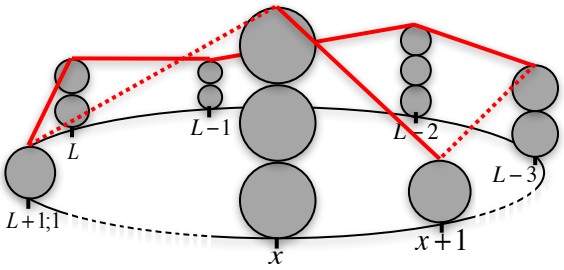

Figure 3.4: Using the ring geometry to fix ideas in mind, the red lines represent the local density profile. Red dotted lines are used when connecting sites which are not shown in the Figure.

is a fixed number. Instead, when the system bulk is in contact with particle reservoirs, we consider the *empirical global density* which is a fluctuating quantity defined as

$$\rho(t) := \frac{N(t)}{L} \in \mathbb{R}^{+}. \tag{3.51}$$

In terms of the stationary distribution (3.29), the *stationary local density*

$$\langle \sigma_N | \hat{N}_x | \mathbb{P}^* \rangle = \langle \eta_x \rangle_* = \phi \partial_\phi \ln z(\phi) =: R(\phi), \tag{3.52}$$

depends on the fugacity ϕ and where $R(0) = 0$. In place of the fugacity, it is often useful to replace the fugacity with the chemical potential $\mu := \ln \phi$ which implies that $R(\mu) = \partial_\mu \ln z(\mu)$. In this way, we can immediately see that the stationary local density is a monotone increasing function since

$$\begin{aligned} \partial_\mu^2 \ln z(\mu) =& \frac{\sum_{n=0}^{\infty} n^2 \omega(n) e^{\mu n}}{z(\mu)} - \frac{\left(\sum_{n=0}^{\infty} n\omega(n) e^{\mu n}\right)^2}{z^2(\mu)} \\ =& \langle \eta_x^2 \rangle_* - (\langle \eta_x \rangle_*)^2 = \mathrm{Var}(\eta_x) > 0, \end{aligned} \tag{3.53}$$

and $\partial_\mu R(\mu) = \partial_\mu^2 \ln z(\mu)$. In the following, we will always write the empirical local density as dependent on the fugacity. Since the partition function is involved in the definition, it is important to consider what happens when we approach the radius of convergence. For this reason, we define the *critical density* as

$$\rho_c := \lim_{\phi \to \phi_c} R(\phi) \in [0, \infty]. \tag{3.54}$$

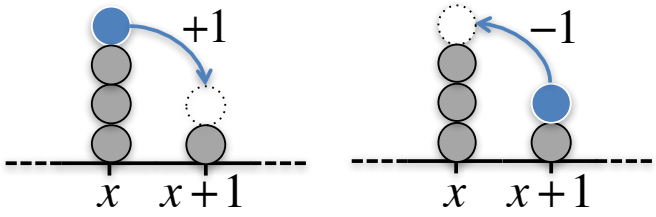

Figure 3.5: Representation of the time-integrated local current. We define the local current counter to increase when particles move to the right and decrease when they move to the left. The particle which is going to move is filled in blue and its arrival arrangement in white.

So for all densities $\rho \leqslant \rho_c$ there exist product measures of the form (3.29) and we can parametrize the distributions by the density. We denoted

$$\text{the inverse of } R(\phi) \text{ as } \Phi(\rho). \tag{3.55}$$

3.2.4.2 Current

For SPS, the prototypical path can be written as

$$\eta_{[0,T_{n+1}]} \coloneqq \left(\left(\eta^0, \tau_0\right), \left(\eta^1, \tau_1\right), \ldots, \left(\eta^{n-1}, \tau_{n-1}\right), \left(\eta^n, \tau_n\right)\right), \tag{3.56}$$

where as before we will write t in place of T_{n+1}. The *empirical time-integrated local current* up to time $t > 0$ across the bond identified by two sites x and $x+1$ is the counting variable defined as (see Figure 3.5)

$$\theta_{x,x+1}\left[\eta_{[0,t]}\right] \coloneqq \sum_{\eta',\eta'' \in \eta_{[0,t]}} \theta^+_{x,x+1}\left(\eta', \eta''\right) - \sum_{\eta',\eta'' \in \eta_{[0,t]}} \theta^-_{x,x+1}\left(\eta', \eta''\right) \in \mathbb{Z}, \tag{3.57}$$

where, given two subsequent configurations η' and η'',

$$\theta^+_{x,x+1}\left(\eta', \eta''\right) \coloneqq \begin{cases} +1 & \text{if } \eta'' = (\eta')^{x,x+1} \\ 0 & \text{otherwise} \end{cases} \tag{3.58}$$

$$\theta^-_{x,x+1}\left(\eta', \eta''\right) \coloneqq \begin{cases} +1 & \text{if } \eta'' = (\eta')^{x+1,x} \\ 0 & \text{otherwise} \end{cases} \tag{3.59}$$

For the whole system, we define the *empirical time-averaged current density* as

$$\mathcal{J}_L\left[\eta_{[0,t]}\right] \coloneqq \frac{1}{Lt}\sum_{x=1}^{L}\theta_{x,x+1}\left[\eta_{[0,t]}\right] \in \mathbb{R}. \tag{3.60}$$

As we have seen before, SPS are HCTMC which means that the holding time in configuration η is exponentially distributed with parameter $c(\eta)$. So, for the state η, the total exit rate, also called the *instantaneous total activity*, is

$$c(\eta) = \sum_{x=1}^{L} g_r(x,\eta) + g_l(x,\eta). \tag{3.61}$$

If we now consider the stationary regime (3.29), we have that the *stationary activity density* is given as

$$A(\rho) \coloneqq \frac{\langle c(\eta)\rangle_*}{L} = \langle g_r(x,\eta)\rangle_* + \langle g_l(x,\eta)\rangle_* = (p+q)\langle u(n_x)\rangle_*\langle v(n_x)\rangle_* \tag{3.62}$$

where $(p+q)=1$. The presence of the factor L^{-1} comes from the fact that rates are additive and the stationary distribution is site factorizable, so every site contributes in the same way. Also, we notice that the activity considers positive contribution from right and left transition rates. The quantity which distinguishes between the direction of the exit rate contributions is the *instantaneous total current*

$$j(\eta) \coloneqq \sum_{x=1}^{L} j_{x,x+1}(\eta) \coloneqq \sum_{x=1}^{L}\left(g_r(x,\eta) - g_l(x+1,\eta)\right) \tag{3.63}$$

together with its averaged counterpart called the *stationary current density*, which is defined as

$$J(\rho) \coloneqq \frac{\langle j(\eta)\rangle_*}{L} = \langle g_r(x,\eta)\rangle_* - \langle g_l(x+1,\eta)\rangle_* = (p-q)\langle u(n_x)\rangle_*\langle v(n_x)\rangle_*. \tag{3.64}$$

where we have expressed the fugacity in function of ρ using (3.55). We see that for totally asymmetric dynamics, for instance with $q=0$, the absolute values of activity and current coincide.

3.2.4.3 Continuity Equation

Even when the system is in contact with particle reservoirs, the particle number in the bulk is locally conserved after each transition and the variation can be either equal to 1, 0 or -1. Thus we can express this variation in terms of differences of a counting variable at different times. For the nearest-neighbour interaction we are

considering, the contributions to the particle variation are restricted to

$$\eta_x(t_2) - \eta_x(t_1) = \theta_{x-1,x}\left[\eta_{[t_1,t_2]}\right] - \theta_{x,x+1}\left[\eta_{[t_1,t_2]}\right]. \tag{3.65}$$

Now, taking the path expectation on both sides and writing $t_2 = t_1 + h$, leads to

$$\mathbb{E}_{t_1+h}[\eta_x] - \mathbb{E}_{t_1}[\eta_x] = \mathbb{E}_{t_1+h}\left[\theta_{x-1,x}\left[\eta_{[t_1,t_1+h]}\right]\right] - \mathbb{E}_{t_1+h}\left[\theta_{x,x+1}\left[\eta_{[t_1,t_1+h]}\right]\right], \tag{3.66}$$

where we notice that the expectation over the counting variable can be written for small h as

$$\begin{aligned}\mathbb{E}_{t_1+h}\left[\theta_{x,x+1}\left[\eta_{[t_1,t_1+h]}\right]\right] =& h\mathbb{E}_{t_1}\left[g_r(x,\eta_{t_1}) - g_l(x+1,\eta_{t_1})\right] + O\left(h^2\right)\\ =& h\mathbb{E}_{t_1}\left[j_{x,x+1}(\eta_{t_1})\right] + O\left(h^2\right).\end{aligned} \tag{3.67}$$

Dividing both sides in (3.66) by h and taking the limit $h \to 0$, leads to the *continuity equation*

$$\frac{d}{dt}\mathbb{E}_t[\eta_x] + \nabla_x \mathbb{E}_t[j_{x-1,x}(\cdot)] = 0, \tag{3.68}$$

where used the lattice derivative (see [43, p. 165])

$$\nabla_x \mathbb{E}_t[j_{x-1,x}] \coloneqq \mathbb{E}_t[j_{x,x+1}] - \mathbb{E}_t[j_{x-1,x}]. \tag{3.69}$$

In the stationary regime we have $\mathbb{E}_*[j_{x,x+1}] \equiv const. = J(\rho)$ since in our case ϕ is independent of x.

3.3 Zero-Range Process

We see that condition (3.28) is satisfied for $v(\eta_x) = 1$ for all $\eta_x \geqslant 0$. In this case, the system is called *Zero-Range process* since the jump rates depend only from the departure site (so the range of interaction is 0). In the following, we will discuss some examples of ZRPs by specifying the jump rate functions. We will include bounded and unbounded jump rates. However, for all models, the totally asymmetric current

(that is (3.64) with $p = 1$ and $q = 0$) coincides with the fugacity parameters since

$$\begin{aligned}\langle u(\eta_x)\rangle_* =& \frac{1}{z(\phi)}\sum_{n=0}^{\infty} u(n)\, w(n)\, \phi^n \\ =& \frac{1}{z(\phi)}\sum_{n=1}^{\infty} \phi^n u(n) \prod_{k=1}^{n}\frac{1}{u(k)} = \frac{1}{z(\phi)}\phi\sum_{n=1}^{\infty}\phi^{n-1}\prod_{k=1}^{n-1}\frac{1}{u(k)} \\ =& \frac{1}{z(\phi)}\phi\sum_{m=0}^{\infty}\phi^m\prod_{k=1}^{m}\frac{1}{u(k)} \\ =& \phi \end{aligned} \tag{3.70}$$

For the zero-range processes, the radius of convergence of the partition function reduces to $\phi_c = \lim_{n\to\infty} u(n)$ if this limit exists in $[0, \infty]$. In addition, for the open boundary case, the zero-range dynamics allows more freedom in the choice of the parameters taking into account the interaction with the reservoirs, while keeping the same stationary probability distribution as in (3.29). In fact, any real numbers can be chosen as the coefficient of the spatial part from and into the reservoirs, see [47] or Figure 7.7.

3.3.1 Three Classes of Jump Rates

The simplest example is given by constant jump rates

$$u(n) = 1 \quad \text{for all } n \geq 1 \quad \text{and} \quad u(0) = 0\,. \tag{3.71}$$

In this case, the stationary measure $\nu_\phi(\eta_x) = (1-\phi)\,\phi^{\eta_x}$ is simply a geometric distribution, and the main quantities involved in the description of the process can be computed explicitly as

$$z(\phi) = \frac{1}{1-\phi}\,, \quad R(\phi) = \frac{\phi}{1-\phi} \quad \text{and} \quad J(\rho) = \frac{\rho}{1+\rho}\,, \tag{3.72}$$

see Figure 3.6. Note that all densities $R(\phi) \geq 0$ are admissible, i.e. there exists a $\phi \geq 0$ such that $R(\phi) = \rho$, while the current $J(\rho) \in [0, 1)$ due to the bounded jump rates for periodic boundary conditions. This process is equivalent to an exclusion process as explained in [43, p. 174]. We will also consider ZRPs with unbounded jump rates, for which it can be shown (see e.g. [19]) that product measures exist for

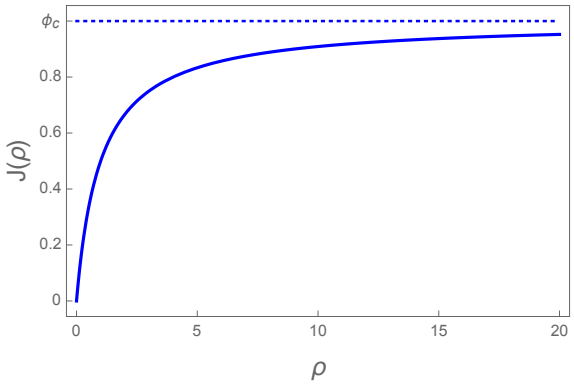

Figure 3.6: Plot of the current-density relation for the total asymmetric ZRP with constant rates. We notice that, as is evident from (3.72), the curve as a horizontal asymptote at $\phi_c = 1$ (dotted line).

all $\phi \geq 0$, and all densities $\rho \geq 0$ are admissible. The first example we consider is

$$u(0) = 0 \ , \quad u\,(n) = n + d \quad \text{for all } n \geq 1 \ , \quad \text{with } d > 0 \ . \tag{3.73}$$

The current behaves asymptotically as $J(\rho) \simeq u(\rho) = d + \rho$ for $\rho \to \infty$ (see left Figure 3.7). Again, the main quantities can be computed explicitly in terms of known special functions, this time the complete and incomplete Euler gamma function, with

$$z(\phi) = de^{\phi}\phi^{-d}\big(\Gamma[d] - \Gamma[d,\phi]\big) \ . \tag{3.74}$$

In particular, this implies that $R(\phi) = \phi\partial_\phi \log z(\phi)$ is a convex function. The second example with unbounded rates is given by sub-linearly diverging jump rates of the form

$$u\,(n) = \frac{[(n+1)^\gamma - 1]}{\gamma} \ , \quad \text{with } \gamma \in (0,1) \ . \tag{3.75}$$

Rather than n^γ we use this regularized functional form for the rates, since $u'(0) = 1$ and it converges uniformly to $u(n) = \log(n+1)$ as $\gamma \to 0$ which can be studied as a limiting case. Again, all densities are admissible with $\rho_c = \infty$. We are not aware of known special functions that lead to exact expressions for the partition function z to simplify the numerics in this case. $J(\rho)$ turns out to be concave for all $\rho \geq 0$ and behaves asymptotically as $J(\rho) \simeq u(\rho) \simeq (1+\rho)^\gamma/\gamma$ as $\rho \to \infty$ (see right Figure 3.7).

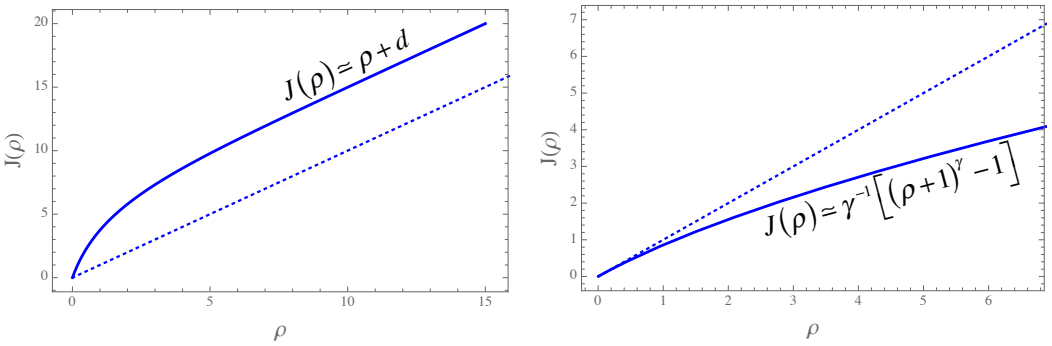

Figure 3.7: (Left) Plot of the current-density relation for the total asymmetric ZRP with linear diverging rates (3.73). The value of the parameter used is $d = 5$. The asymptotic behaviour of the curve is reported in the Figure (dotted line indicates $J(\rho) = \rho$). (Right) Plot of the current-density relation for the totally asymmetric ZRP with sub-linearly diverging rates (3.75). The value of the parameter used is $\gamma = 0.6$. The asymptotic behaviour of the curve is reported in the Figure (dotted line indicates $J(\rho) = \rho$).

3.3.2 Condensation

The second example with bounded jump rates we will consider (which was first introduced in [28, 33]) is given by

$$u(0) = 0 \ , \quad u(n) = 1 + \frac{b}{n} \quad \text{for all } n \geq 1 \ , \quad \text{with } b > 0 \ . \tag{3.76}$$

This form of the rates imply that $\phi_c = 1$. Using the hypergeometric function ${}_2F_1$, we can write the partition function and average density as

$$z(\phi) = {}_2F_1(1, 1; 1 + b; \phi) \quad \text{and} \quad R(\phi) = \tfrac{\phi\, {}_2F_1(2,2;2+b;\phi)}{(1+b)\, {}_2F_1(1,1;1+b;\phi)} \tag{3.77}$$

respectively. In particular, it can be shown (see [45] for rigorous results and [35] for a heuristic derivation) that

$$\rho_c = \tfrac{1}{b-2} \quad \text{for } b > 2 \quad \text{and} \quad \rho_c = \infty \quad \text{for } b \leqslant 2. \tag{3.78}$$

The common interpretation of the existence of a finite critical ρ_c is the following. If the system is prepared with $\rho L > \rho_c L$ particles, it phase separates into a fluid phase, which is homogeneously distributed as ν_{ϕ_c}, and a *condensed phase* or *condensate*, where a finite fraction of $(\rho - \rho_c)L$ particles concentrates on a random single lattice site (see Figure 3.8).

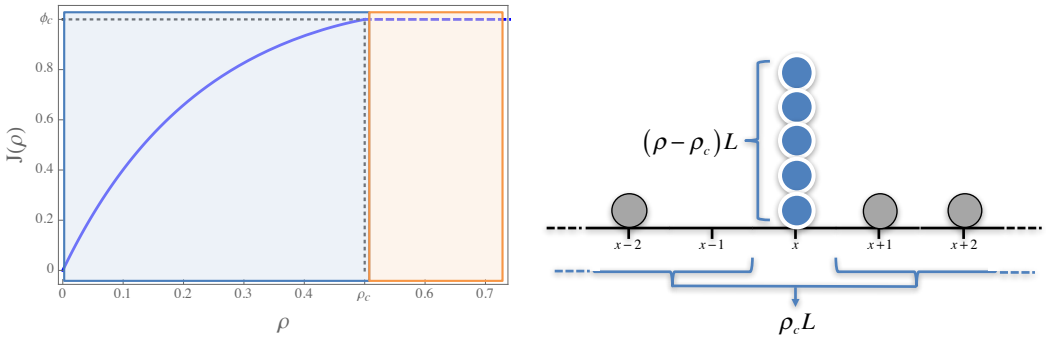

Figure 3.8: (Left) Plot of the current-density relation for the total asymmetric ZRP with bounded condensing rates (3.76). The value of the parameter used is $b = 4$. The two transparent rectangles highlight two different regimes as explained in Section 3.3.2. For $\rho < \rho_c$ the system is in the *fluid phase*, while $\rho > \rho_c$ identifies the condensation region. (Right) Sketch of the condensation phenomenon for a ring lattice with L sites. Since there are no inhomogeneities the site on which the condensate sits is random. We see that the condensate has on average $(\rho - \rho_c) L$ particles, while the bulk accommodates $\rho_c L$ particles.

3.4 Inclusion Process

We see that the condition (3.28) is satisfied also when the jump rates of the arrival site are given as

$$v(\eta_x) = Cu(\eta_x) + v(0) \tag{3.79}$$

where $C \in \mathbb{R}$ and $v(0) = 1$. The second SPS we will work on belongs to this class. In particular, we will consider the case when

$$u(\eta_x) = \eta_x \quad \text{and} \quad v(\eta_x) = \eta_x + 1 \ , \tag{3.80}$$

which is a special kind of *Inclusion Process*. The reason for this name comes from the fact that the transition rates are also increasing in the number of particles of the arrival site assuming, in this way, an inclusive behaviour (as opposite to the exclusion process where the presence of a particle on the arrival site forbids the transition). In this case, the stationary density and current are given as

$$R(\phi) = \tfrac{\phi}{1-\phi} \quad \text{and} \quad J(\rho) = \rho(\rho + 1) \ , \tag{3.81}$$

respectively. They are plotted in Figure 3.9. It is interesting to notice that, as opposed to the zero-range case, the stationary current plot is convex shaped. In the following, we will study the IP on the ring geometry as well as in contact with

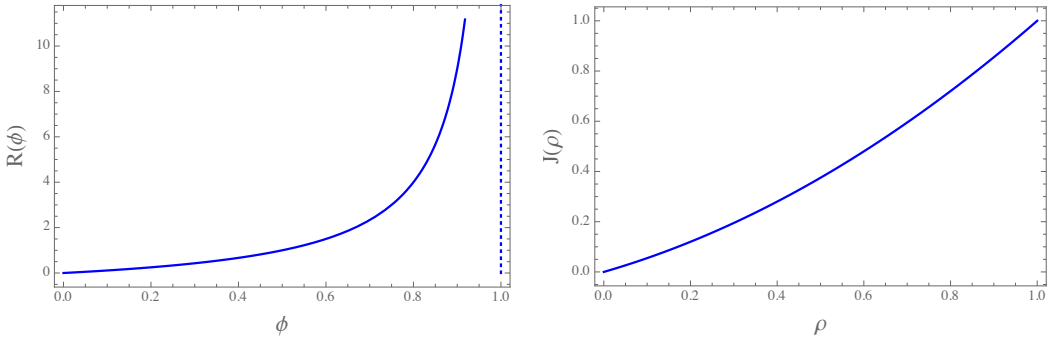

Figure 3.9: Plot of the current-density relation (3.81) for the asymmetric IP. The parameters are $p = 3/4$ and $q = 1/4$.

particle reservoirs. As mentioned in [19], by a suitable rescaling it is possible to express the rate of the arrival site with an additional degree of freedom as

$$v\left(\eta_x\right) = \eta_x + d, \tag{3.82}$$

with $d \in \mathbb{R}^+$, and, for general computations, we will use this form. Moreover, for diverging number of particles and for a finite lattice with closed boundaries, the IP with $p \neq q$ is known to exhibit condensation. Instead, for $p = q$ condensation is achieved only for $d \to 0$. For both cases, see [44].

CHAPTER 4

Micro and Macro Approach to Large Deviations Principles

After having introduced the notation and the models we will work with, here we present the mathematical *Theory of Large Deviations* (LDT), which is used to address the question of determining current fluctuations for stochastic particle systems. First, without deepening the details, we will recall the main statements of LDT to outline its logic structure and main hypothesis. Next, we will see in the context of CTMC how the scaled cumulant generating function, which will be introduced in the text, can be used to calculate a generator whose stationary behaviour coincides with typical fluctuation of the observables. This corresponds to a microscopic perspective to LD. In the end, we will approach stochastic particle systems macroscopically, by giving a heuristic continuous limit argument, and we will introduce suitable rate functions to deal with different kinds of spatial asymmetry.

4.1 Large Deviation Principle

We will present LDT following the recent reviews [80, 81]. Consider a sequence of random variables $A_n \in \mathbb{R}$ indexed by the integer n (which can also be a continuous parameter). We denote the limiting average of A_n by $\bar{A} \coloneqq \lim_{n\to\infty} \mathbb{E}_n [A_n]$. With the notation $A_n \approx a$ with $a \in \mathbb{R}$ we indicate that $A_n \in (a, a + da)$. We say that the random variable A_n satisfies a LDP if the following limit holds

$$\lim_{n\to\infty} -\frac{1}{n} \ln \mathbb{P} [A_n \approx a] = I(a) \in (0, \infty) \ \forall a \in \mathbb{R}. \tag{4.1}$$

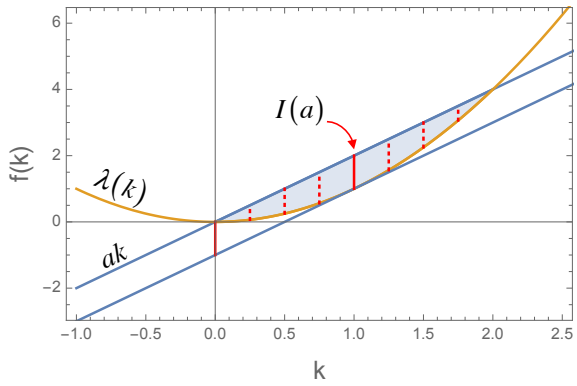

Figure 4.1: Example of the Legendre-Fenchel transform. For each value of a, the corresponding $I(a)$ is given by the maximum distance (considering the sign) between the line ak and the curve $\lambda(k)$. If the SCGF satisfies some regularity conditions, the value of $I(a)$ corresponds to the intercept of the tangent line to $\lambda(k)$ having angular coefficient a.

where I is called the *rate* or *cost function*. The preceding equation is often rewritten in the following form

$$\mathbb{P}[A_n \approx a] \asymp e^{-nI(a)}da \quad \text{as} \quad n \to \infty \ , \tag{4.2}$$

where the symbol $\asymp$ stands for logarithmic equivalence in the sense of (4.1). The rate function can be determined via the *Gärtner-Ellis theorem* [32] which states that if the *Scaled Cumulant Generating Function* (SCGF), defined as

$$\lambda(k) \coloneqq \lim_{n\to\infty} \frac{1}{n} \ln \mathbb{E}_n \left[e^{nkA_n} \right], \tag{4.3}$$

exists and is differentiable and strictly convex for all $k \in \mathbb{R}$, then A_n satisfies a LDP as in (4.2) with rate function given by

$$I(a) = \sup_{k\in\mathbb{R}} \{ka - \lambda(k)\}. \tag{4.4}$$

The preceding equation which puts I in relation with λ is denominated *Legendre-Fenchel transform* (see Figure 4.4). Given these premises, it is possible to determine some general properties about the rate function and its SCGF. We report some of them since they will be used through the thesis while leaving the proofs in the reference [32]:

- positivity of the rate function $I(a) \geqslant 0 \, \forall a \in \mathbb{R}$,

- the minimum of the rate function is achieved at $I\left(\bar{A}\right) = 0$

and for the SCGF, which we assume to be differentiable for all $k \in \mathbb{R}$ in the following,

- $\lambda\left(0\right) = 0$,
- $\frac{d}{dk}\lambda\left(0\right) = \lim_{n\to\infty} \left.\frac{\mathbb{E}_n\left[A_n e^{nkA_n}\right]}{\mathbb{E}_n\left[e^{nkA_n}\right]}\right|_{k=0} = \lim_{n\to\infty} \mathbb{E}_n\left[A_n\right] = \bar{A}$
- if the limit exists, we have $\frac{d^2}{dk^2}\lambda\left(0\right) = \lim_{n\to\infty} n\left(\mathbb{E}_n\left[\left(A_n\right)^2\right] - \mathbb{E}_n\left[A_n\right]^2\right) = \lim_{n\to\infty} n\mathrm{Var}\left(A_n\right)$. In particular, if A_n obeys a standard central limit theorem with $\sqrt{n}\left(A_n - \bar{A}\right) \to N\left(0, \sigma^2\right)$ for some $\sigma^2 > 0$ we have $\frac{d^2}{dk^2}\lambda\left(0\right) = \sigma^2$.

In many applications, A_n can be more complicated than a scalar variable like $A_n = \left(A_n^1, A_n^2\right)$ with rate function $I\left(a^1, a^2\right)$. It is possible to obtain a LDP for one of the components of A_n by marginalizing the associated joint probability distribution using the saddle-point approximation

$$\mathbb{P}\left[A_n^1 \approx a^1\right] = \int_{\mathbb{R}} \mathbb{P}\left[\left(A_n^1, A_n^2\right) \approx \left(a^1, a^2\right)\right] da^2 \tag{4.5}$$

$$\asymp \left(\int_{\mathbb{R}} e^{-nI\left(a^1,a^2\right)} da^2\right) da^1 \tag{4.6}$$

$$\simeq e^{-n\min_{a^2\in\mathbb{R}} I\left(a^1,a^2\right)} da^1. \tag{4.7}$$

which leads to the rate function of A_n^1

$$I^1\left(a^1\right) \coloneqq \inf_{a^2\in\mathbb{R}} I\left(a^1, a^2\right). \tag{4.8}$$

In the context of LDT, the last expression is called the *contraction principle*.

4.2 Microscopic Methods for LD

4.2.1 Effective Microscopic Dynamics

In the present thesis, we will mainly focus on studying the large deviation behaviour of the empirical time-integrated current density for SPS $(\eta_t : t \geqslant 0)$. The LDP can be written as

$$\mathbb{P}\left[\mathcal{J}^L\left[\eta_{[0,t]}\right] \approx j\right] \asymp e^{-tI^L(j)} dj \quad \text{as} \quad t \to \infty \ , \tag{4.9}$$

Using the Gärtner-Ellis theorem, we will see that the calculation of the SCGF reduces to an eigenvalue problem for a suitably defined *tilted generator*. Here, we will

mainly follow [59, 60, 70, 17]. Having in mind a generic path for $\eta_{[0,t]}$, see (3.56), by a direct approach, we write explicitly the expectation of the current SCGF as

$$\begin{aligned}\mathbb{E}_t\left[e^{tk\mathcal{J}_L}\right] &= \int_D e^{tk\mathcal{J}_L\left[\eta_{[0,t]}\right]}\mathbb{P}\left[d\eta_{[0,t]}\right] \\ &= \int_D e^{\frac{k}{L}\sum_{x=1}^{L}\sum_{\eta',\eta''\in\eta_{[0,t]}}\theta^{+}_{x,x+1}\left[\eta_{[0,t]}\right]} e^{-\frac{k}{L}\sum_{x=1}^{L}\sum_{\eta',\eta''\in\eta_{[0,t]}}\theta^{-}_{x,x+1}\left[\eta_{[0,t]}\right]}\mathbb{P}\left[d\eta_{[0,t]}\right].\end{aligned} \tag{4.10}$$

Now, consider two subsequent states η^h and η^j. If, for instance, $\eta^j = \left(\eta^h\right)^{x,x+1}$ then we can move a factor $e^{+\frac{k}{L}}$ from $e^{tk\mathcal{J}_L\left[\eta_{[0,t]}\right]}$ to the corresponding square brackets in $\mathbb{P}\left[d\eta_{[0,t]}\right]$, see (2.77), which is related to the transition from state η^h to state η^j, so to have

$$\left[\left(e^{q_{hh}\tau_n}d\tau_n\right)e^{+\frac{k}{L}}q_{hj}\right]. \tag{4.11}$$

If we repeat this procedure for every transition of the possible paths in D, then (4.10) is equivalent to applying a modified generator which has the following form

$$\mathcal{Q}_k = \begin{cases} q_{hj}e^{\frac{k}{L}\sum_{x=1}^{L}\left(\theta^{+}_{x,x+1}\left(\eta^h,\eta^j\right)-\theta^{-}_{x,x+1}\left(\eta^h,\eta^j\right)\right)} & h\neq j \\ q_{hh} & h=j \end{cases}. \tag{4.12}$$

This new operator, which is called *Exponential Tilted Generator*, can be applied to probability vectors to obtain new vectors like

$$\left|P_k\left(t\right)\right\rangle := e^{\mathcal{Q}_k^T t}\left|\mathbb{P}\left(0\right)\right\rangle, \tag{4.13}$$

which is a solution of the equation

$$\frac{d\left|P_k\left(t\right)\right\rangle}{dt} = \mathcal{Q}_k^T\left|P_k\left(t\right)\right\rangle. \tag{4.14}$$

We notice that $\left|P_k\left(t\right)\right\rangle$ is not a probability vector since it lacks normalization. However, formally, everything resembles the algebraic structure of a master equation. So, calling $P_k\left[d\eta_{[0,t]}\right]$ the corresponding path measure, we can write (4.10) as

$$\mathbb{E}_t\left[e^{tk\mathcal{J}_L}\right] = \int_D e^{tk\mathcal{J}_L\left[\eta_{[0,t]}\right]}\mathbb{P}\left[d\eta_{[0,t]}\right] = \int_D P_k\left[d\eta_{[0,t]}\right]. \tag{4.15}$$

From (4.13), we can get relevant probability vectors by normalizing for the SCGF as

$$\left|\mathbb{P}_k\left(t\right)\right\rangle := \frac{\left|P_k\left(t\right)\right\rangle}{\left\langle\sigma_N\right|e^{\mathcal{Q}_k^T t}\left|\mathbb{P}\left(0\right)\right\rangle} = e^{\mathcal{Q}_k^T t}\frac{\left|\mathbb{P}\left(0\right)\right\rangle}{\left\langle\sigma_N\right|e^{\mathcal{Q}_k^T t}\left|\mathbb{P}\left(0\right)\right\rangle} \tag{4.16}$$

where the denominator is a time dependent normalization, see (2.82). We stress that $|\mathbb{P}_k(t)\rangle$ cannot be understood as the solution of an analogous time-homogeneous master equation, in particular $\frac{d|\mathbb{P}_k(t)\rangle}{dt} \neq \mathcal{Q}_k^T |\mathbb{P}_k(t)\rangle$. To overcome this difficulty, at least in the stationary regime when $t \to \infty$, we use the generalized *Doob's h-transform*. To begin with, we consider the spectral expansion, see (2.67), of the matrix $\mathcal{Q}_k$

$$e^{\mathcal{Q}_k t} \approx \frac{|g_k^R\rangle\langle g_k^L|}{\langle g_k^L|g_k^R\rangle} e^{g(k)t} \quad \text{as} \quad t \to \infty \tag{4.17}$$

where $g(k)$ is the principal eigenvalue of the expansion. The right and left eigenvectors, $\mathcal{Q}_k |g_k^R\rangle = g(k) |g_k^R\rangle$ and $\langle g_k^L| \mathcal{Q}_k = g(k) \langle g_k^L|$ respectively, have components

$$|g_k^R\rangle \coloneqq \textstyle\sum_\eta g_k^R(\eta) |\eta\rangle \quad \text{and} \quad \langle g_k^L| \coloneqq \textstyle\sum_\eta g_k^L(\eta) \langle\eta| \ . \tag{4.18}$$

We also define the matrix

$$\mathcal{Q}_k^* \coloneqq \frac{|g_k^R\rangle\langle g_k^L|}{\langle g_k^L|g_k^R\rangle} g(k) \tag{4.19}$$

which, as we will see, "acts as $\mathcal{Q}_k$" when $t \to \infty$. So with (4.16) and (4.17), we have

$$\lim_{t\to\infty} \langle \mathbb{P}_k(t)| = \frac{\langle \mathbb{P}(0)|g_k^R\rangle\langle g_k^L|}{\langle g_k^L|g_k^R\rangle} \frac{\langle g_k^L|g_k^R\rangle}{\langle \mathbb{P}(0)|g_k^R\rangle\langle g_k^L|\sigma_N\rangle} = \frac{1}{\langle \sigma_N|g_k^L\rangle} \langle g_k^L| =: \langle \mathbb{P}_k^*| \tag{4.20}$$

Then, the Doob transform of $\mathcal{Q}_k$ is a new matrix defined as (see Equation (71) in [17])

$$\tilde{\mathcal{Q}}_k \coloneqq G_k^{-1} \mathcal{Q}_k^* G_k - g(k)\mathcal{I} \tag{4.21}$$

with $\mathcal{Q}_k^*$ as in (4.19) and given the matrices

$$G_k \coloneqq \textstyle\sum_\eta g_k^R(\eta) |\eta\rangle\langle\eta| \quad \text{and} \quad G_k^{-1} = \textstyle\sum_\eta \frac{1}{g_k^R(\eta)} |\eta\rangle\langle\eta| \ . \tag{4.22}$$

The last equality holds since G_k is diagonal and $g_k^R(\eta)$, $g_k^L(\eta) > 0$ as follows from the Perron-Frobenius theorem with $g(k)$ being the principal eigenvalue. Now, we will show that $\tilde{\mathcal{Q}}_k$ gives rise to a Master Equation for a proper probability vector. First, the normalized vector

$$\left\langle \tilde{\mathbb{P}}_k^* \right| \coloneqq \frac{1}{\langle g_k^L|g_k^R\rangle} \sum_\eta g_k^R(\eta) g_k^L(\eta) \langle\eta| \tag{4.23}$$

satisfies

$$\left\langle \tilde{\mathbb{P}}_k^* \right| \tilde{\mathcal{Q}}_k = \langle 0| \, . \tag{4.24}$$

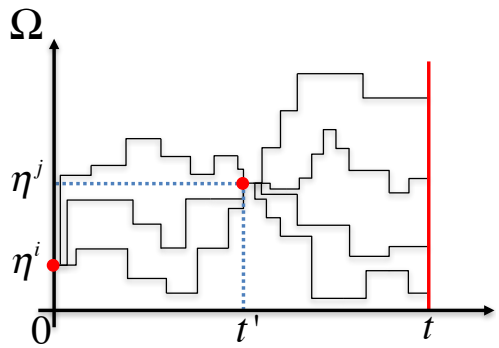

Figure 4.2: Schematic representation of (4.30). The system is prepared in state η^i (first red dot on the left) at time 0 and we are looking at all the transitions towards state η^j at t'. The red vertical line at time t means that we are considering all the transition from state η^j to all other reachable states in Ω. Black lines represent some of the possible paths (in the context of CTMC) connecting the states of the system.

In fact, we have in succession

$$\left\langle \tilde{\mathbb{P}}_k^* \right| G_k^{-1} = \frac{1}{\left\langle g_k^L | g_k^R \right\rangle} \left\langle g_k^L \right| , \tag{4.25}$$

$$\frac{1}{\left\langle g_k^L | g_k^R \right\rangle} \left\langle g_k^L \right| \mathcal{Q}_k^* = \frac{g\left(k\right)}{\left\langle g_k^L | g_k^R \right\rangle} \left\langle g_k^L \right| , \tag{4.26}$$

$$\frac{g\left(k\right)}{\left\langle g_k^L | g_k^R \right\rangle} \left\langle g_k^L \right| G_k = g\left(k\right) \left\langle \tilde{\mathbb{P}}_k^* \right| . \tag{4.27}$$

In this way, $\left\langle \tilde{\mathbb{P}}_k^* \right|$ behaves like a stationary distribution probability vector, see Table 2.1, and, as we did in (2.54), we can write $e^{\tilde{\mathcal{Q}}_k t} \to \left| \sigma_N \right\rangle \left\langle \tilde{\mathbb{P}}_k^* \right|$ as $t \to \infty$. It is possible to show similarly that $\tilde{\mathcal{Q}}_k \left| \sigma_N \right\rangle = \left| 0 \right\rangle$. Second, we can check that $\tilde{\mathcal{Q}}_k$ gives rise to a TPM where its elements are given in terms of a propagator in a fashion similar to (2.41). To do this, we calculate the path integral among three states, like in (2.85), in the limit $t \to \infty$, see Figure 4.2. By preparing the system in a precise state, that is $\left| \mathbb{P}\left(0\right) \right\rangle = \left| \eta^i \right\rangle$, we have that[1]

$$\mathbb{E}_t \left[e^{tk\mathcal{J}_L} \delta_{\eta_{t'}, \eta^j} \middle| \eta_0 = \eta^i \right] \tag{4.28}$$

$$= \frac{\sum_l \mathbb{P}_k \left(\eta_t = l | \eta_{t'} = j\right) \mathbb{P}_k \left(\eta_{t'} = j | \eta_0 = i\right)}{\sum_l \mathbb{P}_k \left(\eta_t = l | \eta_0 = i\right)} \tag{4.29}$$

[1]Here we consider the transposed vector to establish a clear comparison with Equation (14) in [49].

$$= \frac{\langle \sigma_N | \, e^{\mathcal{Q}_k^T (t-t')} \, |\eta^j\rangle \langle \eta^j | \, e^{\mathcal{Q}_k^T t'} \, |\eta^i\rangle}{\langle \sigma_N | \, e^{\mathcal{Q}_k^T t} \, |\eta^i\rangle}. \tag{4.30}$$

In the limit $t \to \infty$, we can make use of the principal contribution of the spectral expansion of $\mathcal{Q}_k$. In fact, by inverting the Doob transform (4.21), so to obtain $\left(G_k^{-1} e^{\tilde{\mathcal{Q}}_k^T t} G_k\right)\left(e^{g(k)t}\mathcal{I}\right) = e^{\left(\mathcal{Q}_k^*\right)^T t}$ and by noticing that $e^{\mathcal{Q}_k^T t} \to e^{\left(\mathcal{Q}_k^*\right)^T t}$ when t increases, we can go through the following steps

$$\lim_{t\to\infty} \frac{\langle \sigma_N | \, G_k^{-1} e^{\tilde{\mathcal{Q}}_k^T (t-t')} G_k \, |\eta^j\rangle \langle \eta^j | \, G_k^{-1} e^{\tilde{\mathcal{Q}}_k^T t'} G_k \, |\eta^i\rangle}{\langle \sigma_N | \, G_k^{-1} e^{\tilde{\mathcal{Q}}_k^T t} G_k \, |\eta^i\rangle} \frac{e^{g(k)(t-t')} e^{g(k)t'}}{e^{g(k)t}}$$

$$= \frac{\langle \sigma_N | \, G_k^{-1} \left|\tilde{\mathbb{P}}_k^*\right\rangle \langle \sigma_N | \, G_k \, |\eta^j\rangle \langle \eta^j | \, G_k^{-1} e^{\tilde{\mathcal{Q}}_k^T t'} G_k \, |\eta^i\rangle}{\langle \sigma_N | \, G_k^{-1} \left|\tilde{\mathbb{P}}_k^*\right\rangle \langle \sigma_N | \, G_k \, |\eta^i\rangle}$$

$$= \frac{\langle \sigma_N | \eta^j\rangle \langle \eta^j | \, e^{\tilde{\mathcal{Q}}_k^T t'} \, |\eta^i\rangle}{\langle \sigma_N | \eta^i\rangle} \frac{g^R\left(\eta^j\right)\left(g^R\left(\eta^j\right)\right)^{-1} g^R\left(\eta^i\right)}{g^R\left(\eta^i\right)}$$

$$= \langle \eta^j | \, e^{\tilde{\mathcal{Q}}_k^T t'} \, |\eta^i\rangle =: \tilde{\mathbb{P}}_k\left[\eta_{t'} = \eta^j | \eta_0 = \eta^i\right].$$

In the end, (4.24) together with (4.2.1) give rise to a Master Equation

$$\frac{d\left|\tilde{\mathbb{P}}_k\left(t'\right)\right\rangle}{dt'} = \tilde{\mathcal{Q}}_k^T \left|\tilde{\mathbb{P}}_k\left(t'\right)\right\rangle \tag{4.31}$$

with the usual exponential solution and whose stationary probability distribution is then obtained by solving the eigenvalue problem related to $\tilde{\mathcal{Q}}_k$. To understand the meaning of the last formula we can look at the expectation of an observable in the tilted stationary regime. As before, we need to take into account an intermediate time t. However, we need to consider an observation time window which is far enough from the origin to be in $\left|\tilde{\mathbb{P}}_k^*\right\rangle$ but not too large so to avoid $|\mathbb{P}_k^*\rangle$. More precisely, we consider edge intervals $[0, \epsilon]$ and $[t-\delta, t]$ with time moving within $t' \in [\epsilon, t-\delta]$. Next, we take the limit $t \to \infty$ and then $\epsilon, \delta \to \infty$ with the constraint that $[\epsilon, t-\delta]$ remains finite

$$\lim_{\epsilon\to\infty} \lim_{t-\delta\to\infty} \langle \sigma_N | \, \mathcal{F} \left|\mathbb{P}_k\left(t'\right)\right\rangle = \lim_{\epsilon\to\infty} \lim_{t-\delta\to\infty} \frac{\langle \sigma_N | \, e^{\mathcal{Q}_k^T (t-t')} \mathcal{F} e^{\mathcal{Q}_k^T t'} \, |\mathbb{P}\left(0\right)\rangle}{\langle \sigma_N | \, e^{\mathcal{Q}_k^T t} \, |\mathbb{P}\left(0\right)\rangle} \tag{4.32}$$

$$= \langle \sigma_N | \, \mathcal{F} \left|\tilde{\mathbb{P}}_k^*\right\rangle. \tag{4.33}$$

The interpretation is that within initial and final transient times, as explained above, the conditioned system is in a stationary state with distribution $\left|\tilde{\mathbb{P}}_k^*\right\rangle$ and $\tilde{\mathcal{Q}}_k^T$ gen-

erates an effective process whose typical dynamics corresponds to the atypical dynamics of the original process.

4.2.2 Current Operator

As we have seen in (4.12), the exponential factor appears only in the off-diagonal terms. So the master equation operator for SPS, as seen in (3.36) and (3.41), can be suitably modified simply by multiplying creation and annihilation operators by $e^{\pm\frac{k}{L}}$ (where the sign depends on the direction of the particle flow). However, also in this case, it is possible to see the meaning of the exponential prefactors in the context of the dynamics of the system. For this reason, we will define a vector space in a similar fashion to $|\eta\rangle$ which will keep track of the number of jumps in the system. Here, we will follow [48, 47].

To begin with, we recall that we label a bond between two sites with respect to the left one, that is given two sites x and $x+1$ their bond will be numbered x. In the open boundaries case, the particle reservoirs will be considered to lie on sites 0 and $L+1$ so the numbering protocol still makes sense. To simplify the presentation of the equations, we will use the ring case as a reference. The basis vectors for the counting space $\Theta = (\mathbb{C}^\infty)^{\otimes L}$ are indicated as

$$|\theta\rangle \coloneqq |\theta_1, \theta_2, ..., \theta_L\rangle \tag{4.34}$$

where $\theta_i \in \mathbb{N}$ records the number of jumps across bond i. In the same fashion of the configuration space, we define the following fundamental vectors

$$|\theta^{+x}\rangle \coloneqq |\theta_1, \theta_2, ..., \theta_x + 1, ..., \theta_L\rangle \quad ; \quad |\theta^{-x}\rangle \coloneqq |\theta_1, \theta_2, ..., \theta_x - 1, ..., \theta_L\rangle$$

and

$$|\sigma_J\rangle \coloneqq \sum_\theta |\theta\rangle$$

which has the same role of $|\sigma_N\rangle$. Following [48, p. 11] Equation 2.13 and below, the counting process of the current is generated by identity, raising and lowering operators (see also [47, p. 6]) defined as

$$\hat{I}\,|\theta\rangle \coloneqq |\theta\rangle \quad , \quad \hat{j}_x^+\,|\theta\rangle \coloneqq |\theta^{+x}\rangle \quad \text{and} \quad \hat{j}_x^-\,|\theta\rangle \coloneqq |\theta^{-x}\rangle \tag{4.35}$$

respectively. Note that this set-up does not follow the usual convention of creation and annihilation operators for particles, but is the standard procedure in the context of current conditioning [51, p. 8]. The role of the particle number operator is played

in this context by

$$\hat{J}_x \left|\theta\right\rangle \coloneqq \theta_x \left|\theta\right\rangle .$$

Also, we define the probability vector for the counting process in a similar way

$$\left|\mathbb{P}_J\left(t\right)\right\rangle \coloneqq \sum_{\theta\in\Theta} \mathbb{P}_\theta\left(t\right)\left|\theta\right\rangle . \tag{4.36}$$

As shown in the Appendix A, the following identities of operators are verified

$$e^{-k\hat{J}_x}\hat{j}_x^{\pm}e^{k\hat{J}_x} = e^{\mp k}\hat{j}_x^{\pm} \quad \text{and} \quad \left[\hat{j}_x^{\pm}, \hat{J}_x\right] = \mp\hat{j}_x^{\pm} \ . \tag{4.37}$$

To embed the counting variable in the master equation, first we need to consider the following tensor product for the basis:

$$\left|\eta\right\rangle \otimes \left|\theta\right\rangle \coloneqq \left|\eta,\theta\right\rangle \in \Omega\otimes\Theta$$

So the probability vector is

$$\left|\mathbb{P}\left(t\right)\right\rangle \coloneqq \left|\mathbb{P}_J\left(t\right),\mathbb{P}_N\left(t\right)\right\rangle \coloneqq \sum_{\{\eta,\theta\}} \mathbb{P}_{\{\eta,\theta\}}\left(t\right)\left|\eta,\theta\right\rangle$$

where the sum is over all possible and compatible[2] couples of η and θ. As observed in [48], the counting variable alone is not a Markov chain since its future time evolution depends on the state of the full process. However, if we consider the joint variable $\left|\eta,\theta\right\rangle$ the process is again Markovian on the joint configuration space. Notwithstanding, generically there is no joint stationary distribution for the coupled process since θ_x can grow indefinitely and the jump rates do not limit θ_x since they do not depend on the counting variables. In the end, the master equation operator of the joint process on a ring is given as

$$\hat{M}_{ring}^{N,J} \coloneqq p\sum_{x=1}^{L}\left[\hat{j}_x^{+}\hat{c}_{x+1}\hat{a}_x\left(\hat{u}_x\hat{v}_{x+1}\right) - \hat{u}_x\hat{v}_{x+1}\right] \tag{4.38}$$

$$+\, q\sum_{x=1}^{L}\left[\hat{j}_x^{-}\hat{c}_x\hat{a}_{x+1}\left(\hat{u}_{x+1}\hat{v}_x\right) - \hat{u}_{x+1}\hat{v}_x\right] . \tag{4.39}$$

Next, as we did in the previous section, we want to calculate the SCGF. This

[2]Given two subsequent configurations η' and $\eta'' = (\eta')^{x,x+1}$, the corresponding current changes from θ' to $\theta'' = (\theta')^{+x}$. This means that $\mathbb{P}_{\{\eta'',\theta''\}} = 0$ if $\theta'' \neq (\theta')^{+x}$.

corresponds to

$$\begin{aligned}\left\langle e^{k\sum_{x=1}^{L} J_x}\right\rangle_t &= \langle \sigma_N, \sigma_J |\, e^{k\sum_{x=1}^{L} J_x}\, |\mathbb{P}_J(t), \mathbb{P}_N(t)\rangle \\ &= \langle \sigma_N, \sigma_J |\, e^{k\sum_{x=1}^{L} J_x} e^{\hat{M}_{ring}^{N,J} t}\, |\mathbb{P}_J(0), \mathbb{P}_N(0)\rangle \\ &= \langle \sigma_N |\, e^{\tilde{M}_{ring}^{N,J}(k) t}\, |\mathbb{P}_N(0)\rangle \end{aligned} \tag{4.40}$$

where $\mathbb{P}_J(0)$ is the canonical basis vector of the no-jump configuration (since no jump has yet occured at time 0) and in the last passage we have used the identities (4.37) to define

$$\begin{aligned}\tilde{M}_{ring}^{N,J}(k) :=& p\sum_{x=1}^{L}\left[e^{\frac{k}{L}}\hat{c}_{x+1}\hat{a}_x\left(\hat{u}_x\hat{v}_{x+1}\right) - \hat{u}_x\hat{v}_{x+1}\right] \\ &+ q\sum_{x=1}^{L}\left[e^{-\frac{k}{L}}\hat{c}_x\hat{a}_{x+1}\left(\hat{u}_{x+1}\hat{v}_x\right) - \hat{u}_{x+1}\hat{v}_x\right].\end{aligned} \tag{4.41}$$

Comparing (4.38) with (4.41), we can see that the counting process operators give rise to the tilting of the master equation operator as happened in (4.15).

4.3 Macroscopic Methods for LD

4.3.1 Hydrodynamic Limit

SPS can be viewed from a macroscopic scale via a coarse-graining procedure which is called *Hydrodynamic Limit*. Heuristically speaking, the hydrodynamic limit consists in considering a system which is made up of many macroscopically small but microscopically large subsystems. With these specifications, we can consider each subsystem to be in a NESS which, however, can differ from the stationary configuration of the other subsystems with which it interacts. In this way, the resulting system can be out of equilibrium and the variation (through many stationary values) of a specific observable along the system appears smooth by increasing the number of subsystems. The goal of the hydrodynamic limit is to write a continuity equation for SPS to see the global effect of microscopic dynamics rules. A rigorous account of this procedure for specific SPS can be found in [56, 76].

Here, we consider a much shorter and intuitive argument to show the scalings of space and time involved in the hydrodynamic limit. We call s the *macroscopic time* defined as $s = \delta t$ where δ is the scaling parameter, which corresponds to speeding up the microscopic time as $t = \frac{s}{\delta}$. The time scaling applies to derivatives

simply as $\frac{d}{dt} = \delta \frac{d}{ds}$. For the spatial part, consider a one-dimensional lattice made up of L components of length ϵ whose total extension is $\ell = \epsilon L$. The Eulerian scaling assumes that, when $\epsilon \to 0$ and $L \to \infty$, the product of their limits $\epsilon L \to \ell$ remains fixed. We call y the *macroscopic space coordinate* defined as $y = \epsilon x \in [0, \ell]$ with $x = 0, 1, \ldots, L$. So, we can consider y to be a coordinate running over the bounded one dimensional space $[0, \ell]$ and, for each L the function $y_L(x) = \epsilon x$ maps points from the discrete lattice to the continuous set $[0, \ell]$.

In addition, we also assume that the total density $\rho = \frac{N}{L}$ remains fixed when N and L tend to infinite. In the end, we call the *macroscopic empirical local density* the map

$$\tilde{\eta}_y : s \mapsto \eta_{[y\epsilon^{-1}]}\left(s\delta^{-1}\right), \tag{4.42}$$

where $\left[y\epsilon^{-1}\right]$ is the integer part of $y\epsilon^{-1}$. In a similar fashion, we call $\tilde{\mathbb{E}}_s$ the path expectation parametrized by macroscopic space and time variables, so that we can calculate the expectation of the macroscopic empirical density as $\tilde{\mathbb{E}}_s\left[\tilde{\eta}_y(s)\right]$. For the Eulerian scaling one considers $\epsilon = L^{-1}$, however, as we will now see, the time scaling δ is not always equal to L^{-1}.

Consider the lattice derivative of the instantaneous local current which, for our choice of jump rates in (3.5), reduces to

$$\begin{aligned} \nabla_x \mathbb{E}_t\left[j_{x-1,x}(\eta)\right] =& \mathbb{E}_t[u(\eta_x)\left(pv(\eta_{x+1}) + qv(\eta_{x-1})\right) && (4.43)\\ & - v(\eta_x)\left(qu(\eta_{x+1}) + pu(\eta_{x-1})\right)]. && (4.44) \end{aligned}$$

In the new spacial coordinates we have $x = yL$ and $x \pm 1 = \left(y \pm \frac{1}{L}\right) L$. As for the density, we write the *macroscopic istanteneous local current* as

$$\tilde{j}^L_{y,y+\frac{1}{L}} : s \mapsto j_{[yL],[yL+1]}\left(\eta\left(s\delta^{-1}\right)\right), \tag{4.45}$$

and the *macroscopic jump rates* like

$$\tilde{u}_L : (y,s) \mapsto u\left(\eta_{[yL]}\left(s\delta^{-1}\right)\right) \quad \text{and} \quad \tilde{v}_L : (y,s) \mapsto v\left(\eta_{[yL]}\left(s\delta^{-1}\right)\right). \tag{4.46}$$

Next, we perform a Taylor expansion of the macroscopic jump rates around the generic point y

$$\tilde{u}_L\left(y \pm \frac{1}{L}, s\right) \simeq \tilde{u}_L(y,s) \pm \frac{1}{L}\frac{\partial \tilde{u}_L}{\partial y}(y,s) + \frac{1}{2}\frac{1}{L^2}\frac{\partial^2 \tilde{u}_L}{\partial y^2}(y,s) \tag{4.47}$$

$$\tilde{v}_L\left(y \pm \frac{1}{L}, s\right) \simeq \tilde{v}_L(y,s) \pm \frac{1}{L}\frac{\partial \tilde{v}_L}{\partial y}(y,s) + \frac{1}{2}\frac{1}{L^2}\frac{\partial^2 \tilde{v}_L}{\partial y^2}(y,s) \tag{4.48}$$

Now, we can put (4.47) in place of u and v in (4.43), to otain a new equation. For asymmetryc dynamics, that is $p \neq q$, the Taylor expansion has the form

$$\nabla_y \tilde{\mathbb{E}}_s \left[\tilde{j}^L_{y-\frac{1}{L},y}(s) \right] \simeq \frac{1}{L}(p-q)\, \tilde{\mathbb{E}}_s \left[\tilde{v}_L(y,s) \frac{\partial \tilde{u}_L}{\partial y}(y,s) + \tilde{u}_L(y,s) \frac{\partial \tilde{v}_L}{\partial y}(y,s) \right]. \tag{4.49}$$

We notice that first order terms do not get canceled, so we have neglected second order contributions. However, for symmetric spatial part, that is $p = q = 1$, we have

$$\nabla_y \tilde{\mathbb{E}}_s \left[\tilde{j}^L_{y-\frac{1}{L},y}(s) \right] \simeq \frac{1}{L^2} \tilde{\mathbb{E}}_s \left[\tilde{u}_L(y,s) \frac{\partial^2 \tilde{v}_L}{\partial y^2}(y,s) - \tilde{v}_L(y,s) \frac{\partial^2 \tilde{u}_L}{\partial y^2}(y,s) \right]. \tag{4.50}$$

A similar L dependance also appears for weakly asymmetric dynamics, that is

$$p = 1 + \tfrac{\nu}{2L} \quad \text{and} \quad q = 1 - \tfrac{\nu}{2L} \quad \text{with} \quad \nu \in \mathbb{R}\ , \tag{4.51}$$

which gives

$$\begin{aligned} \nabla_y \tilde{\mathbb{E}}_s \left[\tilde{j}^L_{y-\frac{1}{L},y}(s) \right] \simeq \frac{1}{L^2} \tilde{\mathbb{E}}_s \Bigg[& \left(\tilde{u}_L(y,s) \frac{\partial^2 \tilde{v}_L}{\partial y^2}(y,s) - \tilde{v}_L(y,s) \frac{\partial^2 \tilde{u}_L}{\partial y^2}(y,s) \right) \\ & + \nu \left(\frac{\partial \tilde{u}_L}{\partial y}(y,s) + \frac{\partial \tilde{v}_L}{\partial y}(y,s) \right) \Bigg]. \end{aligned} \tag{4.52}$$

This means that the time scaling leading to a non-vanishing continuity equation is in this case $t = sL^2$. In the end, the microscopic continuity equation (3.68) is mapped into its counterpart in terms of (y,s) as

$$\frac{\partial}{\partial s} \tilde{\mathbb{E}}_s \left[\tilde{\eta}_y(s) \right] + \nabla_y \tilde{\mathbb{E}}_s \left[\tilde{j}^L_{y-\frac{1}{L},y}(s) \right] = 0. \tag{4.53}$$

4.3.2 Jensen-Varadhan Functional

For the totally asymmetric case, for instance when $p = 1$ and $q = 0$, the time scaling is $t = sL$ and the limit of infinite system size triggers the stationary regime, so, assuming the limit of the functions $\tilde{u}_L$ and $\tilde{v}_L$ is well defined, it is plausible to write (4.53) for $L \to \infty$ as

$$\begin{cases} \frac{\partial \rho}{\partial s}(y,s) + \frac{\partial J}{\partial y}(\rho(y,s)) = 0 \\ \rho(y,0) = \rho_0(y) \end{cases}, \tag{4.54}$$

where $\tilde{\mathbb{E}}_s \left[\tilde{\eta}_y(s) \right] \to \rho(y,s)$ and $\nabla_y \tilde{\mathbb{E}}_s \left[\tilde{j}^L_{y-\frac{1}{L},y}(s) \right] \to \frac{\partial}{\partial y} J(\rho(y,s))$ are the stationary density and current, following the local equilibrium assumption discussed at the beginning of Section 4.3. The relation between density and current as in (4.54), belongs to a more general class of equations called *Hyperbolic Conservation Laws*.

To discuss the general known properties of these systems we will follow [73, 74]. We notice that the first equation can also be expanded as

$$\frac{\partial \rho}{\partial s}(y,s) + \frac{\partial J}{\partial \rho}(\rho(y,s)) \frac{\partial \rho}{\partial y}(y,s) = 0. \tag{4.55}$$

A solution for the above Cauchy problem (that is an ordinary differential equation together with the value of the unknown function at a given point in the domain of the solution) is called *classical* if $\rho(y,s) \in \mathcal{C}^1$ for $s > 0$ and $\rho(y,s) \in \mathcal{C}^0$ for $s \geqslant 0$ (where with $\mathcal{C}^n$ we indicate the set of continuos function whose derivatives are continuos up to the n-th order). It is known for equations of the type (4.55) with non-linear $J(\rho)$ that classical solutions do not always exist. An important apparatus to obtain the solution for the Cauchy problem is the *Method of Characteristics*, which basically gives the solution as the union of height lines. In fact, if $y_c(s)$ describes the equation of a height line for the solution, that is $\rho(y_c(s), s) = c$ for all s, we have in general

$$\frac{d}{ds}\rho(y_c(s), s) = \frac{\partial \rho}{\partial y}(y_c(s), s) \frac{dy_c}{ds}(s) + \frac{\partial \rho}{\partial s}(y_c(s), s) = 0, \tag{4.56}$$

and from (4.55) we get

$$\frac{\partial \rho}{\partial s}(y_c(s), s) = -\frac{\partial J}{\partial \rho}(\rho(y_c(s), s)) \frac{\partial \rho}{\partial y}(y_c(s), s), \tag{4.57}$$

which implies

$$\frac{dy_c}{ds}(s) = \frac{\partial J}{\partial \rho}(\rho(y_c(s), s)) =: f(\rho(y_c(s), s)). \tag{4.58}$$

Since $\rho(y_c(s), s)$ is constant, we can integrate the preceding expression to obtain

$$y_c(s) = f(\rho(y_c(s), s)) s + K, \tag{4.59}$$

where K is an integration constant. This is the equation of a straight line whose parameters can be determined from the initial conditions, that is putting $s = 0$, like

$$y_c(s) = J'(\rho(y_c(0), 0)) s + y_c(0). \tag{4.60}$$

For the present thesis, we are interested in the case in which the initial profile $\rho_0(y)$ is given by a step function, like

$$\rho(y,0) = \begin{cases} \rho_1 & \text{for } y < 0 \\ \rho_2 & \text{for } y \in [0, Y] \\ \rho_1 & \text{for } y > Y \end{cases} \quad \text{with } \rho_2 > \rho_1 \ . \tag{4.61}$$

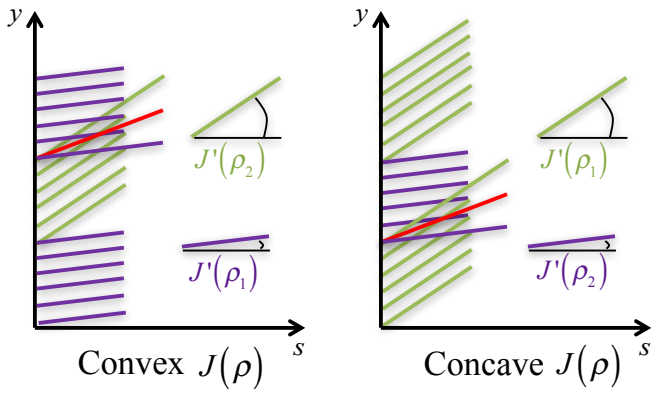

Figure 4.3: These two figures give a visual representation of the position of the shock for convex and concave current density relations. The color code is the following: green corresponds to steeper characteristic lines w.r.t. purple ones and red gives the direction and speed of the shock. Left and right figures correspond to characteristcs for convex and concave $J(\rho)$, respectively.

As can be seen from Figure 4.3, the intersection of characteristics determines an area in which the solution is overspecified and one where it is underspecified. To overcome these difficulties, we consider an integrated version of the continuity equation which gives solutions in a broader sense. So, $\rho(y,s)$ is a *weak solution* if it satisfies

$$\int\int_{s\geqslant 0}\left(\rho\partial_s\varphi + J(\rho)\,\partial_y\varphi\right)dyds + \int_{s=0}\rho_0\varphi dy = 0 \tag{4.62}$$

for every $\varphi(y,s)\in C^1$. It turns out, see [74, p. 248] Equation 15.11, that the weak solution has to fulfill the *Rankine-Hugoniot Condition* (which is basically a conservation of mass principle), that is the intersecting characteristic lines determines a range of possible solutions and the only admissible one has angular coefficient given by

$$v_s(\rho_1,\rho_2) = \frac{J(\rho_2)-J(\rho_1)}{\rho_2-\rho_1}. \tag{4.63}$$

This solution identifies a discontinuity direction and v_s can be interpreted as the propagation speed of a *Shock Wave* (also called *Up Shock*).

On the other side of the shock characteristics drift apart. This means that there is a region in which there is not enough information to propagate characteristic lines and we have freedom in the choice of the solution. While weak solutions always exist, they are typically not unique. A possible strategy is to define a shock wave

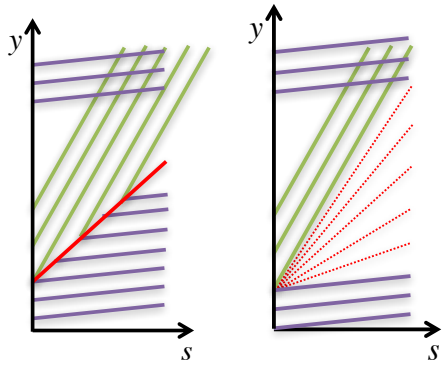

Figure 4.4: Using the color code in Figure 4.3, here we see two admissible weak solution for the Riemann problem with convex current density relation. (Left) The two characteristic lines meet on another characteristic line with angular coefficient in between the two. This corresponds to a sharp transition in the resulting evolution profile. (Right) The solution is given by a pencil of characteristics (red dotted lines) whose slope smoothly varies from the slow to the fast characteristics. This case is the one considered as the entropy solution to the Riemann problem.

satisfying Rankine-Hugoniot condition (see left image in Figure 4.4). Otherwise, we can interpolate between the angular coefficients of the two set of lines (see right image in Figure 4.4). In the latter case, the resulting solution is called *Rarefaction Wave* and, heuristically, seems the most physical solution since it leads to a flat profile on a finite torus (see Figure 4.5). Also, characteristics do not start at the shock position, which would be problematic with the concept of determinism.

In the end, we would like to have a simple mathematical criterion on the weak solutions to single out the unique physical one. This was developed by Kruzkov (see [73]) and is known as *Entropy Criterion*. To see how this approach appears from the weak solution, first we write the conservation law (4.54) in the presence of viscosity

$$\frac{\partial \rho}{\partial s}(y,s) + \frac{\partial J}{\partial y}(y,s) = \varepsilon \frac{\partial^2 \rho}{\partial y^2}(y,s), \tag{4.64}$$

which has now a unique smooth solution called ρ^ε. Second, consider a regular convex function $\rho \mapsto h(\rho)$, called *entropy*, whose corresponding *entropy flux* is given by a function $g(\rho)$ such that

$$\partial_\rho g(\rho) = \partial_\rho J(\rho)\, \partial_\rho h(\rho). \tag{4.65}$$

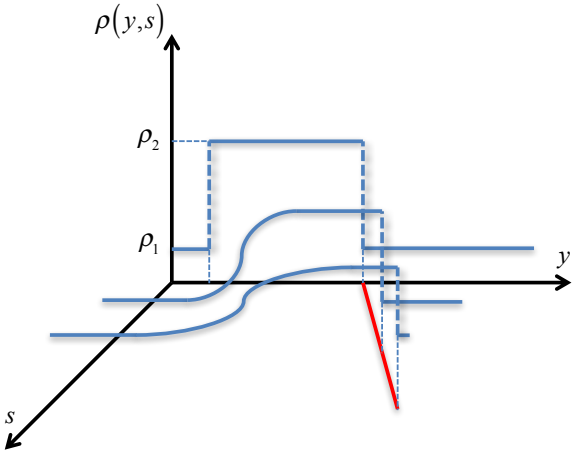

Figure 4.5: Visual representation of the evolution of the step profile for a prototypical hyperbolic conservation law with convex current density relation. The red line traces the shock propagation. Opposite to it, the step profile dissipates into a flat profile following a rarefaction fan solution.

Then, it is possible to show, see [73, p. 33], that the following inequality holds

$$\frac{\partial h}{\partial s}\left(\rho^{\varepsilon}\right)+\frac{\partial g}{\partial y}\left(\rho^{\varepsilon}\right) \leqslant \varepsilon \frac{\partial^{2} h}{\partial y^{2}}\left(\rho^{\varepsilon}\right). \tag{4.66}$$

Now, after having moved all the terms to the right in (4.66), multiplied by a test function φ and integrated, we say that, in the limit of $\varepsilon \to 0$, a weak solution $\rho = \rho(y,s)$ is called an *entropy solution* if

$$\int \int_{t \geqslant 0}\left(h(\rho) \partial_{s} \varphi+g(\rho) \partial_{x} \varphi\right) dyds+\int_{t=0} h\left(\rho_{0}\right) \varphi dy \geqslant 0 \tag{4.67}$$

for all possible entropy-entropy-flux pairs and every $\varphi(y,s) \in C^1$. Intuitively, (4.67) is related to the total entropy of the solution, which should be non-negative. From the last formula, we can deduce the Rankine-Hugoniot condition and the *Lax Shock Condition* which is given as

$$\begin{array}{ll} J'\left(\rho_{1}\right)>v_{s}\left(\rho_{1}, \rho_{2}\right)>J'\left(\rho_{2}\right) & \text{if } J''<0 \\ J'\left(\rho_{2}\right)>v_{s}\left(\rho_{1}, \rho_{2}\right)>J'\left(\rho_{1}\right) & \text{if } J''>0 \end{array}. \tag{4.68}$$

for a shock (ρ_1, ρ_2) to be stable and evolve according to (4.63). As we can see, the last inequality rules out the left case in Figure 4.4. Heuristically speaking, when characteristics collide, picking a specific shock speed means, at each time step, to

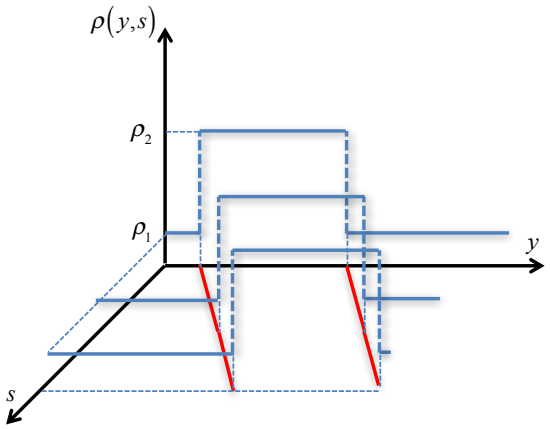

Figure 4.6: Visual representation of the large deviation evolution of the step profile for a prototypical hyperbolic conservation law with convex current density relation. The right red line traces the shock propagation, while the left one (which is parallel to the shock direction) shows that the rarefaction fan is not created.

loose information about the original initial conditions of the system along the shock direction. Thus, we can calculate the entropy production rate across a shock (ρ_1, ρ_2) as

$$\frac{d}{ds}\int h(\rho(y,s))\,ds = g(\rho_1) - g(\rho_2) - \frac{J(\rho_2)-J(\rho_1)}{\rho_2-\rho_1}\left(h(\rho_1)-h(\rho_2)\right) \tag{4.69}$$

$$=: \mathcal{F}(\rho_1,\rho_2)\,. \tag{4.70}$$

For convex current functions, the step profile results in a shock wave and a rarefaction fan as can be seen in Figure 4.5. Since the underlying dynamics of SPS is stochastic, there is the possibility that the initial step profile of type (4.61) evolves as a stable traveling wave $\rho(\cdot,[0,s])$ (see Figures 4.6 and 4.7). This is a large deviation event whose rate function, introduced by Jensen and Varadhan [54] and then further developed by Vilensky [87], was first proved for the TASEP to be given by

$$\mathbb{P}\left[\rho_L([0,sL]) \approx \rho(.,[0,s])\right] \asymp e^{-sL\mathcal{F}(\rho_l,\rho_r)} \quad \text{as } L\to\infty\ . \tag{4.71}$$

Here s is fixed and $\rho_L(t)$ is the measure corresponding to the empirical density $\rho_L(dy,t) := \frac{1}{L}\sum_{x=1}^{L}\eta_x(t)\,\delta_{\frac{x}{L}}(dy)$ which under the large deviation event in the time window $[0,s]$ weakly converges to the non-entropic solution $\rho(y,s)$ on the unit torus. In (4.71) a specific entropy function h has to be used to determine $\mathcal{F}(\rho_1,\rho_2)$. This is the thermodynamic entropy which is given by the Legendre transform of the

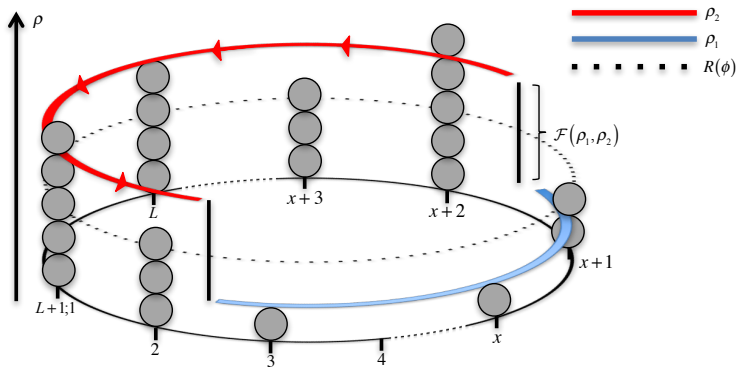

Figure 4.7: Microscopic schematic picture of the step profile for convex current density relation. The vertical black bars highlight the presence of a density separation. The left one is stable and corresponds to the shock propagating on the ring, while to keep stable the right one we need to pay a cost equal to $\mathcal{F}(\rho_l, \rho_r)$.

pressure $\ln z(\phi)$ via

$$h(\rho) = \rho \ln \Phi(\rho) - \ln z(\Phi(\rho)) \ . \tag{4.72}$$

where $\Phi(\rho)$ is given in (3.55). This result has been applied in [14] heuristically in a different scaling. For fixed, large system size L, lower current deviations for the asymmetric exclusion process on a ring are realized by phase separated travelling wave step profiles with two densities $\rho_1 < \rho_2$, which are uniquely determined by the total mass and conditional current, as explained in detail in Chapter 5. The probabilistic cost to realize such a profile does not depend on the system size since only the non-entropic down shock has to be stabilized. This cost is equal to the entropy production across the reversed stable shock given by $\mathcal{F}(\rho_1, \rho_2)$, which is also equal to $-\mathcal{F}(\rho_2, \rho_1)$ by obvious symmetry in (4.69).

4.3.3 Macroscopic Fluctuation Theory (MFT)

MFT [8] is a general framework to tackle the problem of determining the rate function for SPS in the continuos limit. This theory expresses the rate function as a functional in the space of the density as well as current profile which needs to be minimized with respect to both space and time. It was shown in [14], that the JV rate function can be determined from the MFT one in the limit of vanishing viscosity, that is by writing the continuity equation equal to $\varepsilon\Delta\rho$ with $\varepsilon \to 0$ like in 4.64, for the ASEP with open boundaries. However, the two theories have different regimes of applicability. In particular, the MFT needs to satisfy two constraints.

Firstly, the spatial part of the jump rates of the system needs to be symmetric or weakly asymmetric. Secondly, to apply MFT, we need to verify that the model is of *gradient type*, that is there exists a function $h : \Omega \to \mathbb{R}$ such that the instantaneous local current can be written as the difference of two configurations of the system which are translated with respect to each other, that is

$$g_r(x,\eta) - g_l(x+1,\eta) = h(\tau_x\eta) - h(\tau_{x+1}\eta). \tag{4.73}$$

Here $\tau_x\eta$ is a new configuration obtained from η by shifting (in terms of the position of the configuration vector entries) to the right all the occupation numbers by x, like $(\tau_x\eta)_i = \eta_{i-x}$.

The MFT also considers an external field ν (which is assumed constant in the present thesis) acting on the particles. This is taken into account as an exponential tilting of the jump rates

$$\begin{aligned} j^{\nu}_{x,x+1}(\eta) =& g_r(x,\eta) - g_l(x+1,\eta)\, e^{\frac{\nu}{2}} && (4.74)\\ \simeq& h(\tau_x\eta) - h(\tau_{x+1}\eta) + \frac{1}{2}\left(g_r(x,\eta) + g_l(x+1,\eta)\right)\nu, && (4.75)\end{aligned}$$

where in the last step we have performed a first order Taylor expansion of e^{ν} around $\nu = 0$. This means that the external field considered is small compared to the range of the interaction and the system can still be described by a diffusive dynamics: for strong fields the continuity equation of the system is better approximated by hyperbolic conservation laws as in the Jensen-Varadhan case. In this sense, ν is understood as a *microscopic field* encoding a weak asymmetry. In a similar fashion as before, it can be proved that in the hydrodynamic limit $j^{\nu}_{x,x+1}(\eta) \to J^{\nu}(\rho(y,s),y,s)$ and the continuity equation

$$\frac{\partial\rho}{\partial s}(y,s) + \frac{\partial J^{\nu}}{\partial y}(\rho(y,s),y,s) = 0. \tag{4.76}$$

is subject to a costraint called the *constitutive equation* which fixes the expression of the macroscopic stationary current to be

$$J^{\nu}(\rho(y,s),y,s) = -D(\rho(y,s))\frac{\partial\rho}{\partial y}(y,s) + \nu\chi(\rho(y,s)). \tag{4.77}$$

Here

$$D(\rho) = \tfrac{\partial}{\partial\rho}\langle h(\tau_x\eta)\rangle_* \quad \text{and} \quad \chi(\rho) = \tfrac{1}{2}\langle g_r(x,\eta) + g_l(x+1,\eta)\rangle_*\ , \tag{4.78}$$

where $\langle\,\rangle_*$ denote the stationary expectation as defined in (2.58). Given these premises, the MFT in its general form is able to provide a joint LDP and rate function for the density and current profiles (see Equation 8.53 in [8]). The latter is in general difficult to be determined analytically since it involves spatial as well as time integrals. However, the rate function of the current only can be determined from the general MFT rate function via contraction, see (4.8). In addition, since we are mostly interested in the behaviour of the system for large times and with open boundaries, we will use a simpler approach by assuming that the minimization of the rate function is achieved through a stationary density profile [51, 60]. So, in this simplified version, the MFT states that, in the limit of large system size, the probability that the microscopic empirical time-averaged current density converges to some macroscopic value j decays as

$$\mathbb{P}\left[\mathcal{J}_L\left[\eta_{[0,L^2s]}\right] \approx j\right] \asymp e^{-LI(j)}dj \quad \text{as } L \to \infty \ , \tag{4.79}$$

where the rate function is given by

$$I(j) = I\left(\bar{\rho}_j(y), j\right) = \min_{\rho(y)}\left\{I\left(\rho(y), j\right)\right\} \equiv \min_{\rho(y)}\left\{\int_0^1 \frac{\left(j - J^{\nu}(\rho, y)\right)^2}{4\chi(\rho)}dy\right\}, \tag{4.80}$$

where $\bar{\rho}_j(y)$ is the optimal profile and we have dropped the time dependence since we are assuming static density profiles. This assumption together with the continuity equation also implies that the current j is constant in space. In other words, the MFT takes into account deviations of the empirical current from the constitutive equation. The expression (4.80) is obtained from the Girsanov Formula, see Equation A.6 in [7], where the jump rates of one process are an exponentially tilted version of the other followed by a first order expansion.

Without specifying the jump rates, we can put the optimization problem in a readily applicable form for different kinds of models. First we can substitute (4.77) in (4.80) to get

$$I\left(\rho(y), j\right) = \int_0^1 \frac{\left(j - \nu\chi(\rho)\right)^2}{4\chi(\rho)}dy + \int_0^1 \frac{\left(D(\rho)\right)^2}{4\chi(\rho)}\left(\frac{\partial\rho}{\partial y}\right)^2 dy \tag{4.81}$$

$$+ \frac{j}{2}\int_{\rho_0}^{\rho_1}\frac{D(\rho)}{\chi(\rho)}d\rho - \frac{\nu}{2}\int_{\rho_0}^{\rho_1} D(\rho)\,d\rho \tag{4.82}$$

where we have used the Jacobian $\frac{\partial\rho}{\partial y}dy = d\rho$ and ρ_0 together with ρ_1 are the particle

reservoirs densities. We can verify directly that

$$I\left(\rho\left(y\right),j\right)-I\left(\rho\left(y\right),-j\right)=j\int_{\rho_0}^{\rho_1}\frac{D\left(\rho\right)}{\chi\left(\rho\right)}d\rho, \tag{4.83}$$

as follows from the fluctuation relation like in [13, p. 3]. To simplify the notation in the following calculations, we now call

$$A\left(\rho\right)\coloneqq\tfrac{\left(j-\nu\chi(\rho)\right)^2}{4\chi(\rho)}\quad,\quad B\left(\rho\right)\coloneqq\tfrac{\left(D(\rho)\right)^2}{4\chi(\rho)}\quad\text{and}\quad\rho'=\tfrac{\partial\rho}{\partial y}\ . \tag{4.84}$$

To obtain the optimal density profile, we perform the functional derivative

$$\begin{aligned}\frac{\delta}{\delta\rho}I=&\left(\frac{\partial}{\partial\rho}A-\frac{d}{dy}\frac{\partial}{\partial\rho'}A\right)+\left(\frac{\partial}{\partial\rho}\left(B\rho'^2\right)-\frac{d}{dy}\frac{\partial}{\partial\rho'}\left(B\rho'^2\right)\right)\\=&\frac{\partial}{\partial\rho}A-\left(\frac{d}{dy}\rho\right)^2\frac{d}{d\rho}B-2B\frac{d^2}{dy^2}\rho\end{aligned} \tag{4.85}$$

Here, the optimal profile is such that $\frac{\delta I}{\delta\rho}\left(\bar{\rho}_j\left(y\right),j\right)=0$. If we multiply both sides of (4.85) by $\frac{d\bar{\rho}_j}{dy}$ we get, using the optimal profile,

$$0=\frac{d}{dy}\left[A\left(\bar{\rho}_j\right)-B\left(\bar{\rho}_j\right)\left(\frac{d\bar{\rho}_j}{dy}\right)^2\right]. \tag{4.86}$$

Since the last derivative is null, the function inside the brackets is equal to

$$A\left(\bar{\rho}_j\right)-B\left(\bar{\rho}_j\right)\left(\frac{d\bar{\rho}_j}{dy}\right)^2=\text{const.}=:C \tag{4.87}$$

We can rearrange the terms to have

$$\frac{d\bar{\rho}_j}{dy}=\pm\sqrt{\frac{A\left(\bar{\rho}_j\right)-C}{B\left(\bar{\rho}_j\right)}}. \tag{4.88}$$

Given the reservoir density ρ_0, the optimal value of the density at each y is determined by solving the following equation with respect to $\bar{\rho}_j\left(y\right)$

$$\pm\int_{\rho_0}^{\bar{\rho}_j(y)}\sqrt{\frac{B\left(\bar{\rho}_j\right)}{A\left(\bar{\rho}_j\right)-C}}d\bar{\rho}_j=y, \tag{4.89}$$

where the constant C is fixed from the other reservoir particle density by solving $\bar{\rho}_j\left(1\right)=\rho_1$. Equation (4.88) simplifies a bit the rate function which now, by direct

substitution, reduces to

$$I(j) = 2\int_0^1 A(\bar{\rho}_j(y))\,dy - C + \frac{j}{2}\int_{\rho_0}^{\rho_1} \frac{D(\bar{\rho}_j)}{\chi(\bar{\rho}_j)} d\bar{\rho}_j - \frac{\nu}{2}\int_{\rho_0}^{\rho_1} D(\bar{\rho}_j)\,d\bar{\rho}_j. \tag{4.90}$$

To determine the explicit expression of the optimal density profile and the relative cost function, we need to specify the details of the model through the jump rates which then specify $D(\rho)$ and $\chi(\rho)$. In Chapter 7, we will see the MFT in action for the inclusion process.

CHAPTER 5

Large Deviations for Totally Asymmetric SPS on a Ring

In this chapter, we will apply the JV approach, introduced in Section 4.3.2, to the TAZRP and TAIP. For what regards the former, we will look at different families of zero-range dynamics with constant, bounded and unbounded jump rates with concave current-density relations. These will include processes which give rise to the condensation phenomenon (see Section 3.3.2) for which we can compare the large deviation cost of travelling wave (introduced in Section 4.3.2) and condensed profiles. Next, to test the robustness of the JV scheme, we will repeat the same analysis for the inclusion process which, on the contrary, satisfies a convex current-density relation.

5.1 TAZRP

In Chapter 3, we introduced generators for SPS in great generality. For the present Section of the current chapter, we will focus on the TAZRP which, to fix the ideas, defined by

$$\hat{M}_{TAZRPring} = \sum_{x=1}^{L} \left[\hat{c}_{x+1}\hat{a}_x\left(\hat{u}_x\right) - \hat{u}_x\right] \tag{5.1}$$

where $v\left(\eta_x\right) \equiv 1$ and the spatial part reduces to $q = 0$ and $p = 1$.

5.1.1 Current Large Deviations

For fixed L and N the ZRP is a finite-state, irreducible Markov chain on $X_{L,N}$, and a general approach in [10, 9] implies a large deviation principle (LDP) for the empirical current (3.60) in the limit $t \to \infty$. The authors establish an LDP for general empirical densities and flows on path space, and the particle current

is a continuous and in fact linear function of the empirical flow. Then using the contraction principle (4.8) (see e.g. [25, 80]) and linearity they were able to show that the current $\mathcal{J}^L(t)$ satisfies a LDP with a convex rate function. We denote the associated rate function by I^L, and following the usual compact formulation for LDPs (see e.g. [80]) on the level of logarithmic equivalence we have for all lower deviations $j \leqslant J(\rho)$

$$\mathbb{P}\left[\mathcal{J}^L(t) \leq j\right] \asymp e^{-tI^L(j)} \quad \text{as } t \to \infty \,. \tag{5.2}$$

Based on results in [13, 14] for the ASEP on a one-dimensional ring, our main result is a derivation of the rate function for diverging system size

$$I(j) = \lim_{L\to\infty} I^L(j) \,, \tag{5.3}$$

for lower deviations, where $j \leq J(\rho)$. We focus on TAZRPs where the current density relation (3.64)

$$J(\rho) \quad \text{is a non-linear, concave, increasing function,} \tag{5.4}$$

equivalently $R(\phi)$, as given in (3.52), is a non-linear convex increasing function of ϕ. This imposes implicit conditions on the jump rates, which cannot be made explicit to our knowledge, but are fulfilled for example if $u(n)$ is itself non-linear, increasing and concave. Linear functions $J(\rho)$, corresponding to independent particles, are not covered by our general approach, but are of course simple to treat and will be discussed later in Section 5.1.3.3. Note that for all ZRPs, $J(\rho)$ and $R(\phi)$ are increasing, and so the only restriction is on the convexity. Since the current is a time-additive functional, we expect large deviations to be realized homogeneously in time, i.e. modulo a transient depending on the initial conditions, the function $s \mapsto \mathcal{J}^L(s)$ conditioned on $\mathcal{J}^L(t) \leq j$ is roughly constant and equal to j for $s \leq t$. For a discussion of examples where conditioning does not lead to time-homogeneous behaviour see e.g. [4].

In analogy to results for exclusion processes [14], we will see that if the system does not exhibit condensation ($\rho_c = \infty$) then typical realizations of lower current deviations for large L are dominated by phase separated states, as discussed in Section 4.3.2, which are non-entropic weak solutions of the hydrodynamic limit of the ZRP with two spatially separated regions at different densities. Since the phase boundaries move at non-zero speed we will refer to these step profiles as travelling wave profiles, which may exist only in a limited range of conditional

currents. Outside this range, or for systems with finite critical density ($\rho_c < \infty$), condensed states may dominate the current large deviation, where a finite fraction of particles concentrates on a single, fixed lattice site.

5.1.2 General Results

Even though they are only proved for the ASEP, the results in [54, 86, 87] depend only on the hyperbolic scaling limit and are of a general nature that can, at least heuristically, be applied directly to other particle systems. Therefore we assume that the same formalism used for the exclusion process in [14] applies to the ZRPs we consider here, since we assume that they also have concave flux functions $J(\rho)$. This assumption is motivated by the one-to-one correspondence between the dynamics of the ASEP and the ZRP with constant rates, see Appendix B.2 for the mapping.

Below we described two efficient strategies for the process to realise a large deviation of the current $\mathcal{J}^L(t) \leq j < J(\rho)$. The first is by travelling wave profiles, for which we can estimate the large deviation cost of realising a current j using a Jensen-Varadhan approach, similar to that used in [14] for the exclusion process. We denote this cost by $E_{\text{tw}}(j)$ (see (5.13)). Secondly, if the process can exhibit condensation under the stationary measures (i.e. $\rho_c < \infty$) we will see that such a large deviation in the current are sometimes more efficiently realised by condensed states. We denote the large deviation cost associated with realising a current $j < J(\rho)$ by a condensed state by $E_c(j)$ (see (5.20)). Our main result is that for any TAZRP with concave flux function the large deviation rate function (5.3) in the limit $L \to \infty$ is given by

$$I(j) = E_{tw}(j) \quad \text{for all } j < J(\rho)\,, \qquad \text{if } \rho_c = \infty\,, \tag{5.5}$$

and is given by the lower convex hull

$$I(j) = \underline{\text{conv}}\big\{E_{tw}, E_c\big\}(j) \quad \text{for all } j < J(\rho)\,, \qquad \text{if } \rho_c < \infty\,. \tag{5.6}$$

This constitutes a dynamical phase transition, where the realization of current large deviations switches from travelling wave to condensed profiles for low enough values of j. Details on applying this to different examples and finite-size corrections for large L will be discussed in Section 5.1.3, in the following we provide definitions and general results for travelling wave and condensed profiles.

5.1.2.1 Travelling Wave Profiles

Travelling wave profiles are characterized by pairs of fugacities (or currents) $\phi_1 \leq j < J(\rho) \leq \phi_2$ under the constraints of fixed total density ρ and total current $j < J(\rho)$. These constraints are characterized by

$$j = (1-x)\,\phi_1 + x\phi_2 \tag{5.7}$$

$$\rho = (1-x)\,R(\phi_1) + xR(\phi_2)\ , \tag{5.8}$$

where $x \in [0,1]$ parametrizes the volume fraction of the high density ϕ_2 phase. Since $\phi_1 < \phi_2$, by eliminating the variable

$$x = \frac{j-\phi_1}{\phi_2-\phi_1}, \tag{5.9}$$

the constraints (5.7) and (5.8) can be re-written as

$$G(\phi_1,\phi_2) := \frac{\rho(\phi_2-\phi_1) - \phi_2 R(\phi_1) + \phi_1 R(\phi_2)}{R(\phi_2)-R(\phi_1)} = j, \tag{5.10}$$

which implicitly defines a one-dimensional subset of admissible fugacity pairs (ϕ_1,ϕ_2) explained in detail in Section 5.1.3. In Figure 5.1 (left) all relevant quantities are illustrated for the constant rate ZRP, and Figure 5.2 (left) shows an illustration of a travelling wave profile.

The large deviation cost associated with such traveling wave profile can be determined in terms of the thermodynamic entropy (4.72). Since the stationary current for the TAZRP is simply given by $J(\rho) = \Phi(\rho)$, it is easy to see that the corresponding entropy flux that fulfills (4.65) is

$$g(\rho) = \Phi(\rho)\big(\ln\Phi(\rho) - 1\big)\ . \tag{5.11}$$

With the shock speed $v_s = \frac{\Phi(\rho_2)-\Phi(\rho_1)}{\rho_2-\rho_1}$ the Jensen-Varadhan functional for a single shock (4.69), which gives the large deviation cost, can be written conveniently as a

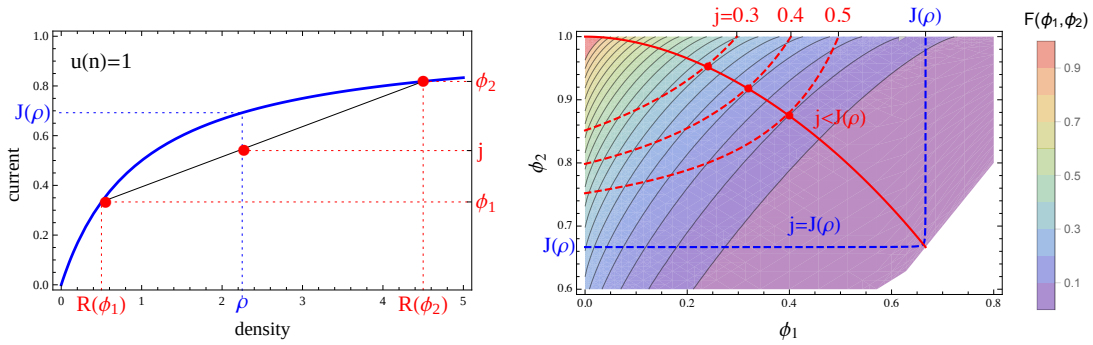

Figure 5.1: The two plots feature the constant rate TAZRP (3.71). (Left) The blue line depicts the current-density relation for the constant rate ZRP (3.71), while the intersecting black line is obtained from the consistency relations (5.7) and (5.8), varying the volume fraction x between 0 and 1. For a fixed density ρ each admissible pair (ϕ_1, ϕ_2) corresponds to a current $j < J(\rho)$. (Right) Contour plot of the Jensen-Varadhan functional (5.12) is shown together with the constraint curves (5.10) (red dashed lines), which are plotted for several values of $j < J(\rho)$. The blue dashed line is the limiting constraint line for $j \to J(\rho)$. The full red dots correspond to the minimizers of (5.14). The union of all the optimal points is represented as a full red line.

function of fugacities $\phi_i = \Phi(\rho_i)$ for a general ZRP,

$$\begin{aligned} F(\phi_1, \phi_2) &:= \mathcal{F}(R(\phi_1), R(\phi_2)) = -\mathcal{F}(R(\phi_2), R(\phi_1)) \\ &= g\big(R(\phi_1)\big) - g\big(R(\phi_2)\big) - v_s\Big[h\big(R(\phi_1)\big) - h\big(R(\phi_2)\big)\Big] \\ &= \Big[(\phi_1 \ln \phi_1 - \phi_1) - (\phi_2 \ln \phi_2 - \phi_2)\Big] - \Big[\frac{\phi_2 - \phi_1}{R(\phi_2) - R(\phi_1)}\Big] \times \\ &\quad \times \Big[(R(\phi_1) \ln \phi_1 - \ln z(\phi_1)) - (R(\phi_2) \ln \phi_2 - \ln z(\phi_2))\Big]. \end{aligned} \tag{5.12}$$

The partition function $z(\phi)$ and density $R(\phi) = \phi\partial_\phi \ln z(\phi)$ can be computed (often explicitly) without the need of inverse functions, and current or fugacity are therefore more suitable variables than densities for ZRP.

Important general properties of (5.12) are the following. $F(\phi_1, \phi_2)$ is decreasing in ϕ_1 and increasing in ϕ_2, and it is anti-symmetric, i.e. $F(\phi_1, \phi_2) = -F(\phi_2, \phi_1)$. Therefore $F(\phi, \phi) = 0$, which corresponds to 0 cost for vanishing step size, and it is positive for $\phi_2 > \phi_1$. In all examples we have studied F is also convex and has concave level lines, but we are not able to show this in general. In our examples, F is also a smooth function on its domain of definition which is either $[0, \phi_c)^2$ or $[0, \phi_c]^2$ in case of a condensing system with $\phi_c < \infty$. This is always the case as long

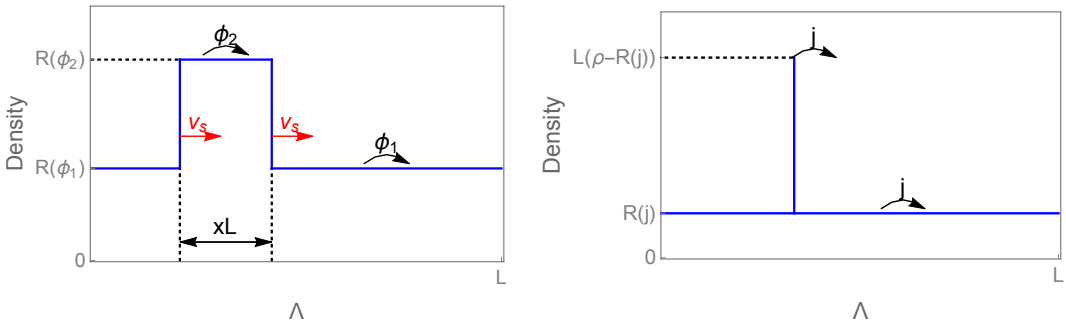

Figure 5.2: Illustrations of phase separated profiles on the lattice Λ with periodic boundary conditions. (Left) A traveling wave profile with high density region at density $R(\phi_1)$ and low density region at $R(\phi_2)$ satisfying (5.7) and (5.8). The profile moves to the right with shock speed v_s given by (5.18). (Right) Condensed state profile with density of the fluid phase given by $R(j)$ and a fixed condensate of typical size $L(\rho - R(j))$.

as $\log z$ is smooth.

Due to concavity of the flux function $J(\rho)$, the above profiles actually realize lower current deviations as is illustrated in Figure 5.1 (left). We fix a density $\rho > 0$ with an associated typical stationary current $J(\rho)$, and condition on a current $j < J(\rho)$. If the system has a finite critical density $\rho_c < \infty$, we also require $\rho < \rho_c$. The rate function of the exponential cost to realize a travelling wave profile is then given by minimizing (5.12) subject to the constraint (5.10), that is

$$E_{tw}(j) := \inf_{\phi_1,\phi_2} \left\{ F(\phi_1,\phi_2) \,:\, G(\phi_1,\phi_2) = j \right\} \in [0,\infty] \,. \tag{5.13}$$

Depending on the regularity of F and G in a given example, the minimizer in (5.13) is often a local minimizer in the interior of the domain and can be found as a solution to the following system of equations

$$\begin{cases} \partial_1 F(\phi_1,\phi_2)\,\partial_2 G(\phi_1,\phi_2) - \partial_2 F(\phi_1,\phi_2)\,\partial_1 G(\phi_1,\phi_2) = 0 \\ G(\phi_1,\phi_2) = j \end{cases} . \tag{5.14}$$

In general, it is not clear if there exists a unique minimizer in (5.13) or whether it is a local or a boundary minimum, and it is not possible to get explicit expressions. We will see later in Section 5.1.3 that, for the jump rates considered here (which were introduced in Section 3.3), it is possible to numerically confirm that the infimum is unique, but that in some cases the constraint (5.10) cannot be fulfilled and

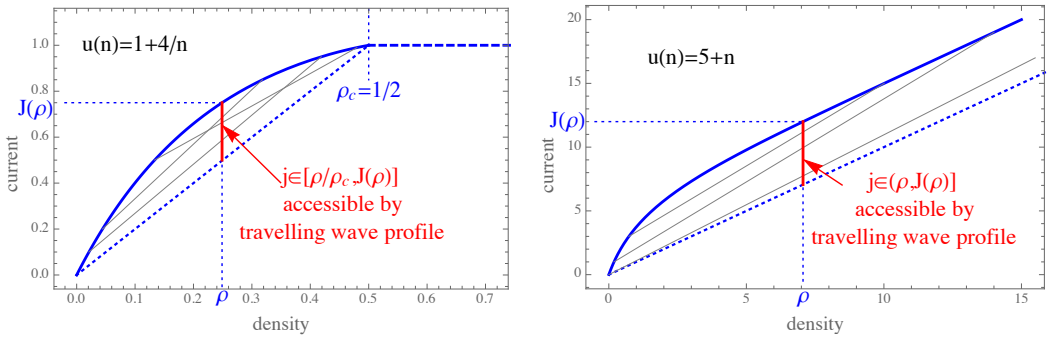

Figure 5.3: Restricted range of currents $j \leq J(\rho)$ which are admissible by travelling wave profiles for a condensing process with rates (3.76) (left), and for asymptotically linear rates (3.73) (right). The grey lines indicate examples of admissible pairs (ϕ_1, ϕ_2) as in Figure 5.1 (left).

there are no travelling wave profiles, resulting in the cost in (5.13) being equal to $\inf \emptyset = \infty$. Travelling wave profiles with more than one up and one down step are more costly than the simple one shown in Figure 5.2 (left) and do not contribute to current large deviation events considered here.

Properties of the travelling wave profile. For the constant rate example illustrated in Figure 5.1, picking $\phi_1 = 0$, it is clear that all currents $0 \leq j \leq J(\rho)$ are admissible for the constraint (5.10) $G(0, \phi_2) = \rho \frac{\phi_2}{R(\phi_2)} = 0$, since $\phi_2 / R(\phi_2) = 1 - \phi_2 \to 0$ as $\phi_2 \to 1$. As is illustrated in Figure 5.3, the smallest current j admissible by travelling wave profiles is in general given by

$$j_{min} = \rho \lim_{\phi_2 \nearrow \phi_c} \frac{\phi_2}{R(\phi_2)} \,, \tag{5.15}$$

where ϕ_c could be finite or infinite. A bounded range of admissible currents j is possible due to a bounded range of densities in condensing systems (e.g. with rates (3.76)), where $j_{min} = \phi_c \frac{\rho}{\rho_c}$, or if $R(\phi)$ is asymptotically linear, as is the case for the system with rates (3.73), where $j_{min} = \rho$.

It is clear from the illustration in Figure 5.1 (left), and the fact that $\phi / R(\phi)$ is decreasing as a consequence of (5.4), that for given ρ and admissible j, ϕ_2 is uniquely determined by ϕ_1. Therefore, for any admissible j with $\phi_1 \leq j \leq J(\rho)$ the solution of the constraint (5.10) implicitly defines a function

$$\bar{\phi}_2(\phi_1) \text{ such that } G(\phi_1, \bar{\phi}_2(\phi_1)) = j \,, \tag{5.16}$$

shown by dashed red lines in Figure 5.1 (right). $\bar{\phi}_2(\phi_1)$ is strictly increasing in ϕ_1 and since $R(\phi)$ and its inverse are also continuous, $\bar{\phi}_2(\phi_1)$ is in fact a continuous increasing function for all $\phi_1 \in [0, j)$. Actually, this domain is bounded above by a value strictly smaller than j for systems with $j_{min} > 0$, and for non-accessible currents $j < j_{min}$ the function (5.16) is not defined. This applies to the examples in Sections 5.1.3.3 and 5.1.3.4 and is discussed there in detail. At the left boundary for $\phi_1 = 0$ the value of $\bar{\phi}_2(0) > 0$ is the positive solution to

$$\rho\phi_2 = jR(\phi_2)\,, \tag{5.17}$$

which exists for all admissible $j < J(\rho)$ and is easily constructed graphically (see Figure 5.1 (left)). We further note that the high density volume fraction x (5.9) as well as the speed of profile

$$v_s = (\phi_2 - \phi_1)/(R(\phi_2) - R(\phi_1)) \tag{5.18}$$

are decreasing with increasing ϕ_1, and in systems with $j_{min} = 0$ both vanish as $\phi_1 \to j$.

For all the examples we studied it further turns out that $\bar{\phi}_2(\phi_1)$ is convex, and with convexity of $F(\phi_1, \phi_2)$ and resulting concave level lines, this leads to a unique minimum of the cost F along the curve $(\phi_1, \bar{\phi}_2(\phi_1))$ as is illustrated in Figure 5.1 (right) for the constant rate process. This minimum could be located inside the domain of definition, or located at the boundary $\phi_1 = 0$ or $\phi_2 = \phi_c$ in the case $\phi_c < \infty$. The location of minima for different $j < J(\rho)$ is shown by a full red line in Figure 5.1 (right). For the typical current $j = J(\rho)$ no condition on the system is imposed and the optimal pair is given by $\phi_1 = \phi_2 = J(\rho)$.

Since we assume non-linearity and concavity of the function $J(\rho)$, it is clear from Figure 5.3 that $j_{min} < J(\rho)$ and there are currents at least close to the typical one which are admissible by travelling wave profiles. Furthermore, due to smoothness of the constraint curve (5.10) and the Jensen-Varadhan functional (5.12), and due to anti-symmetry of the latter, the travelling wave cost function (5.13) is continuous and $E_{tw}(J(\rho)) = 0$ at the typical value for the current. Therefore $E_{tw}(j)$ itself is a proper rate function for the current, and in many cases $I(j) = E_{tw}(j)$.

5.1.2.2 Condensed States

A given current $j < J(\rho)$ can also be realized by the bulk of the system taking density $R(j)$ and all the excess mass $(\rho - R(j))L$ being located on one single (fixed) lattice site. In general, when conditioning on a low current j, a stable condensed

state is obtained when the current out of the condensate matches the current $j < J(\rho)$ in the bulk phase of the system. The condensate acts as a boundary reservoir, the exit rate of which has to be slowed down from a value of order $u\big((\rho - R(j))L\big)$ to j, to assure the right incoming current into the bulk. Then the cost to maintain a stable condensate corresponds to the cost of slowing down a Poisson process across one bond (see e.g. [47])

$$E_c^L(j) = u\big((\rho - R(j))L\big) - j + j \ln \frac{j}{u\big((\rho - R(j))L\big)} \ . \tag{5.19}$$

This is not exact, since we simply replaced the argument of the rates $u(n)$ by an average value. But with our regularity assumptions on u (see (3.5) and below), we have for any n that $u\left((\rho - R\left(j\right))L + n\right) = u\left((\rho - R\left(j\right))L\right) + O\left(\frac{1}{L}\right)$ as $L \to \infty$. So (5.19) is correct to leading order in L. Condensed phase separated profiles are illustrated in Figure 5.2. Note that opposed to travelling wave profiles, the range of admissible currents for condesed states is always given by the full interval $[0, J\left(\rho\right))$.

For unbounded rates u, $E_c^L(j)$ diverges as $L \to \infty$ of order $u\big((\rho - R(j))L\big)$. However, travelling wave profiles always yield costs $E_{tw}(j)$ which are independent of the system size L (see (5.13)) for $j_{\min} < j < J(\rho)$. For such systems the current rate function (5.6) is therefore given by $I(j) = E_{tw}(j)$ for all $j > j_{min}$, and condensed profiles may only contribute in systems with bounded jump rates or if $j_{min} > 0$ in which case not all currents are admissible by travelling wave profiles. An example of the latter is given by asymptotically linear jump rates (3.73), which is discussed in detail in Section 5.1.3.3.

If u is bounded and has a limit, we have $\phi_c = \lim_{k\to\infty} u(k) < \infty$ and for diverging system size the condensed cost converges to a finite value

$$E_c^L(j) \to E_c(j) = \phi_c - j + j \log \frac{j}{\phi_c} \quad \text{as } L \to \infty \quad \text{if } \phi_c < \infty \ . \tag{5.20}$$

Examples of bounded jump rates, in particular the cases of constant rate and condensing ZRP are discussed below in Sections 5.1.3.1 and 5.1.3.4. Note that the expressions (5.19) and (5.20) only apply for $j < J(\rho)$, and that $\lim_{j\to J(\rho)} E_c(j) > 0$ does not vanish when approaching the typical current. In fact, $E_c^L(J(\rho))$ and $E_c(J(\rho))$ are not well defined and depend on details of the limiting sequences involved in (5.20), so the condensed cost itself is not a valid large deviation rate function. In particular, since $j < J\left(\rho\right) < \phi_c$, the minimizer $E_c(\phi_c) = 0$ is outside

the range of validity of (5.20). However, we have seen above that travelling wave profiles are always admissible for currents j just below $J(\rho)$ and $E_{tw}(J(\rho)) = 0$. Therefore the rate function is always dominated by travelling wave profiles for j sufficiently close to $J(\rho)$, and condensed profiles can only be relevant for lower values of j where the description in (5.19) and (5.20) is valid.

If the jump rates are bounded but $\rho_c = \infty$, that is the system does not exhibit condensation under the stationary measures for any density, we will now show that condensed profiles are always less likely than travelling wave profiles. With bounded jump rates we have $\phi_c < \infty$ and $\frac{R(\phi)}{\phi} \to \infty$ as $\phi \to \phi_c$. This implies that $j_{min} = 0$ from (5.15), and includes for example the constant rate case. In order to compare condensed and travelling wave profiles, we fix the size of the high density phase to be $x = \frac{1}{L}$. Together with j and ρ this fixes a particular pair (ϕ_1^c, ϕ_2^c) on the constraint curve (5.16) which does not necessarily minimize (5.12). From the phase separation conditions (5.7) and (5.8), we have

$$x = \frac{1}{L} = \frac{j - \phi_1^c}{\phi_2^c - \phi_1^c} \quad \text{and} \quad R(\phi_2^c) = L\rho - (L-1)\, R(\phi_1^c) \ . \tag{5.21}$$

In the limit $L \to \infty$ this implies

$$\phi_1^c \simeq j \quad \text{with} \quad R(\phi_2^c) \simeq L(\rho - R(j)) \tag{5.22}$$

and from (3.70)

$$\phi_2^c \simeq J(L(\rho - R(j))) \to \phi_c. \tag{5.23}$$

The cost of such a travelling wave profile then satisfies

$$F(\phi_1^c, \phi_2^c) \to \phi_c - j + j \log \frac{j}{\phi_c} = E_c(j) \quad \text{as } L \to \infty, \tag{5.24}$$

where we have used that $\log z(\phi_2)/R(\phi_2) \to 0$ as $\phi \to \phi_c$ (see Lemma in Appendix B). Then, (5.22) is consistent with a single large condensate realizing the current deviation and (5.23) determines the convergence of ϕ_2 towards ϕ_c with increasing L. Note also that the speed (5.18) of such profiles vanishes

$$v_s = \frac{\phi_2^c - \phi_1^c}{R(\phi_2^c) - R(\phi_1^c)} \to 0 \quad \text{as } L \to \infty, \tag{5.25}$$

since $R(\phi_2^c)/\phi_2^c \to \infty$, which is consistent with a condensed state. In this case, for bounded jump rates with diverging density $R(\phi)$, the condensed profile can be

realised as a formal limit of a travelling wave profiles with $\phi_2 \to \phi_c$. This provides a connection between suboptimal travelling waves and condensed profiles, and in-particular implies that

$$E_{tw}(j) \leq E_c(j) \quad \text{for all } j_{min} \leq j \leq J(\rho) \tag{5.26}$$

and the result (5.5) applies. This is illustrated for the constant rate ZRP in Figure 5.4 in Section 5.1.3.1, where the optimal travelling wave profile leads actually to a strictly lower cost unless we condition on a current $j = j_{min} = 0$.

In case $\rho_c < \infty$ we will see in Section 5.1.3.4 that the rate function $I_L(j)$ is given by the lower convex hull of the condensed and travelling wave costs as in (5.6).

5.1.3 Large Deviation Results for Different Models

In this section, we determine the optimal travelling wave profiles for different types of jump rates introduced in Section 3.3.1 and 3.3.2, finding explicit or numerical solutions to the minimization (5.14) for travelling wave profiles, which turn out to be unique in all cases as long as the conditioned current j is admissible. This unique solution depends on the parameters j and ρ, and is denoted (ϕ_1^o, ϕ_2^o) in the following, and also referred to as the optimal pair or fugacities. In light of (5.6), we compare the resulting cost (5.13) with the condensed cost (5.19) to derive the large deviation rate function for the current $I(j)$, and also include remarks on finite size versions $I^L(j)$ where appropriate.

5.1.3.1 Constant Rate TAZRP

For constant rate ZRPs, with rates (3.71), we have $z(\phi) = (1-\phi)^{-1}$ and $R(\phi) = \phi/(1-\phi)$ (see (3.72)), so the Jensen-Varadhan functional (5.12) takes the simple form

$$F(\phi_1, \phi_2) = (\phi_2 - \phi_1) + \phi_1\phi_2 \log \frac{\phi_1}{\phi_2} - (1-\phi_1)(1-\phi_2) \log \frac{1-\phi_1}{1-\phi_2}, \tag{5.27}$$

and the constraint (5.10) reduces to

$$G(\phi_1, \phi_2) = \phi_1\phi_2 + \rho(\phi_2 - 1)(\phi_1 - 1) = j. \tag{5.28}$$

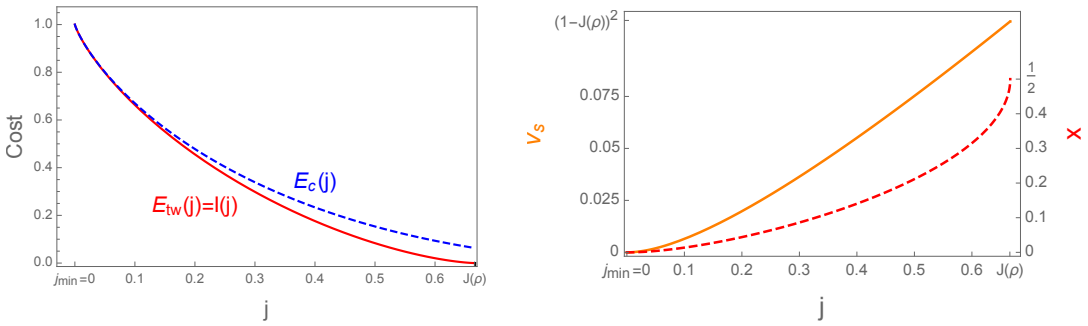

Figure 5.4: Both plots feature the constant rate TAZRP with $u(n) = 1$ and $\rho = 2$. (Left) The traveling wave cost E_{tw} (5.13) shown in full red and the condensed cost E_c (5.33) in dashed blue. The condensed cost is always larger than the traveling wave cost for bounded rates. The red curve was generated implicitly from (5.31) and (5.28). (Right) The spatial fraction of the high density phase (red dashed) and the shock speed (full orange) are increasing functions of j. At the typical current $j = J(\rho)$ we have $\phi_1^o = \phi_2^o$, the high and low density phases are indistinguishable and they occupy half of the system each, that is $x = \frac{1}{2}$. The limiting speed is given by $v_s(J(\rho), J(\rho)) = (1 - J(\rho))^2$.

Explicit computations of the second derivative and the determinant of the Hessian show that $\bar{\phi_2}(\phi_1)$ from (5.28) is convex and F has concave level lines, which leads to unique optimal pairs (ϕ_1^o, ϕ_2^o), as illustrated in Figure 5.1 (right). Using the above explicit expressions, the first equation in the system (5.14) can be simplified to the implicit relation

$$(\phi_2^o)^\rho (1 - \phi_2^o) = (\phi_1^o)^\rho (1 - \phi_1^o). \tag{5.29}$$

By regularity of the function $f(s) := s^\rho (1 - s)$, it is easy to show that (5.29) has exactly one solution $\phi_2^o > \phi_1^o \in (0, 1)$. In [78] Section VII, a particular parametrization is given as

$$\phi_1^o = \frac{e^\lambda - e^{\lambda(1-\rho_0)}}{e^\lambda - 1}, \quad \phi_2^o = \frac{e^{\lambda\rho_0} - 1}{e^\lambda - 1}. \tag{5.30}$$

Here λ is the usual Lagrange multiplier of the maximization problem of the Jensen-Varadhan functional constrained to (5.8) and ρ_0 is the density of the TASEP which is equivalent to the TAZRP with $\rho_0 = \frac{\rho}{1+\rho}$ via a standard mapping (see e.g. [43]). A few examples of explicit solutions to (5.29) are

$$\begin{aligned} \phi_2^o &= \tfrac{1}{2}\left(2 - \phi_1^o - \sqrt{(4 - 3\phi_1^o)\,\phi_1^o}\right) && \rho = \tfrac{1}{2} \\ \phi_2^o &= 1 - \phi_1^o && \rho = 1 \\ \phi_2^o &= \tfrac{1}{2}\left(1 - \phi_1^o + \sqrt{1 + 2\phi_1^o - 3(\phi_1^o)^2}\right) && \rho = 2, \end{aligned} \tag{5.31}$$

where we notice that for $\rho > 1$, the (ϕ_1^o, ϕ_2^o) form a concave curve while for $\rho < 1$ it is convex. The resulting cost function is illustrated in Figure 5.4 where we plot $E_{tw} = F(\phi_1^o, \phi_2^o)$ against the current $j = G(\phi_1^o, \phi_2^o)$. From (5.31) we see that $\phi_2^o \to 1$ as $\phi_1^o \to 0$, and in this limit $j = G(\phi_1^o, \phi_2^o) \to 0$, which is consistent with $j_{min} = 0$. For $j \to 0$ the spatial proportion of the two phases and the shock speed are then given by

$$x = \frac{j - \phi_1^o}{\phi_2^o - \phi_1^o} \to 0 \quad \text{and} \quad v_s(\phi_1^o, \phi_2^o) = (1 - \phi_2^o)(1 - \phi_1^o) \to 0 \ , \tag{5.32}$$

as illustrated in Figure 5.4. This corresponds to a static, condensed profile, which is consistent with the weaker but more general result (5.24), where we observe that in this case the limiting condensed profile is asymptotically optimal. Using (5.20) with $\phi_c = 1$ the limiting cost for condensed configurations is given by

$$E_c(j) = 1 - j + j \log j > E_{tw}(j) \quad \text{for all } j > 0 \ , \tag{5.33}$$

and only for $j = 0$ we have $E_c(0) = E_{tw}(0) = 1$. Therefore, the large deviation rate function is given by $I(j) = E_{tw}(j)$ as shown in Figure 5.4.

5.1.3.2 Unbounded Sublinear Rates

In this section we focus on the TAZRP with rates given by $u(n) = \frac{(n+1)^\gamma - 1}{\gamma}$ with $\gamma \in (0, 1)$ introduced in (3.75), for which we have $J(\rho) \simeq (1 - \rho)^\gamma / \gamma$. This implies

$$J(\rho)/\rho \to 0 \quad \text{and} \quad \frac{\rho \partial_\rho J(\rho)}{J(\rho)} \to \gamma < 1 \quad \text{for } \rho \to \infty \ , \tag{5.34}$$

and all the results of this section will hold under these more general conditions. For the above rates, the Jensen-Varadhan functional can in general not be written as an explicit function of ϕ_1 and ϕ_2 and we rely on numerical solutions to calculate the optimal pairs (ϕ_1^o, ϕ_2^o) and the cost $E_{\text{tw}}(j)$. Illustrations are shown in Figure 5.5 for $\gamma = 0.6$. As $j \to j_{min} = 0$ we have $\phi_1^o \to 0$ and $\phi_2^o \to \phi_c = \infty$. Together with (5.9), this again implies that the volume fraction x of the high density phase vanishes in the limit $j \to 0$ as well as the speed v_s of the profile. Continuity of the Jensen-Varadhan functional F allows us to commute limits, and formally we get

$$\lim_{j \to 0} F(\phi_1^o, \phi_2^o) = \lim_{\phi_2^o \to \infty} F(0, \phi_2^o) = \lim_{\phi_2^o \to \infty} \phi_2^o \left(1 - \frac{\ln z(\phi_2^o)}{R(\phi_2^o)}\right) = \infty \ . \tag{5.35}$$

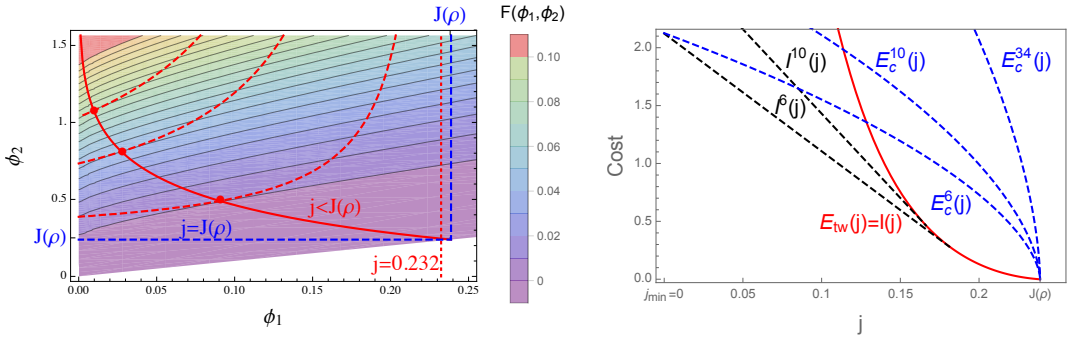

Figure 5.5: Both plots feature the ZRP with rates $u(n) = \frac{(n+1)^\gamma - 1}{\gamma}$, using $\rho = 0.25$ and $\gamma = 0.6$. (Left) Contour plot of the Jensen-Varadhan functional (5.12), constraint curves (5.10) in red dashed for three values of $j < J(\rho)$. Note that all values of j are close to $J(\rho)$, and the asymptote is shown for the rightmost constraint curve with $j = 0.232$ (dotted red). Optimal pairs (full red) are shown analogously to Figure 5.1. (Right) The cost $E_{tw}(j)$ (5.13) (full red), diverges as $j \to j_{min} = 0$, shown alongside $E_c^L(j)$ (5.37) (dashed blue) for several small values of L. Resulting finite size rate functions $I^L(j)$ (5.3) are approximated by dashed black lines, while the limiting rate function is equal to $I(j) = E_{tw}(j)$ in accordance with (5.5).

Here we have used l'Hôpital's rule and a change of variables to get

$$\lim_{\phi\to\infty} \frac{\ln z(\phi)}{R(\phi)} = \lim_{\rho\to\infty} \frac{\rho\partial_\rho J(\rho)}{J(\rho)} < 1 \tag{5.36}$$

where we used $R(\phi) = \phi\partial_\phi \ln z(\phi)$ and the fact that $R(\phi)$ is the inverse of $J(\rho)$. The final inequality is from (5.34).

As in the previous section, for large finite systems the relevant travelling wave profiles as $j \to 0$ correspond to a high density volume fraction $x = 1/L$ in (5.9). This implies $R(\phi_2^o) \sim \rho L$ and a single site contains a non zero fraction of the total mass, so that $\phi_2^o \sim L^\gamma \rho^\gamma/\gamma$. Together with (5.35) this leads to a scaling of $F(0, \phi_2^o) \simeq (1-\gamma)\phi_2^o \sim L^\gamma$.

The cost for condensed profiles for large L is approximately given by (5.19), which implies

$$E_c^L(j) \approx \frac{1}{\gamma}\left((\rho - R(j))L\right)^\gamma = \frac{L^\gamma}{\gamma}(\rho - R(j))^\gamma \tag{5.37}$$

for all $j < J(\rho)$. This is also proportional to L^γ, and again travelling wave profiles are asymptotically similar to condensed profiles with a cost on the same scale in L as $j \to 0$.

As can be seen from Figure 5.5, the cost for condensed profiles for all fixed

$j > 0$ is again higher than the one for travelling wave profiles for large enough system size. Therefore the limiting rate function is simply $I(j) = E_{tw}(j)$ and (5.5) holds. For finite systems with fixed large L, however, the condensed cost $E_c^L(j)$ is eventually lower than $E_{tw}(j)$ for small enough j, and is a concave function of j. This leads to a linear part of the rate function $I^L(j)$ for small j indicating a mixture between travelling wave and completely condensed profiles where all particles are trapped on a single site. This feature is a rather persistent finite size effect illustrated by dashed lines in Figure 5.5 (right). Note that the very small systems shown in the plot only contain of the order of 1 or 2 particles and are just intended for illustration. Low enough deviations in larger systems are not accessible numerically, so the crossover is hard to observe in simulations.

5.1.3.3 Asymptotically Linear Rates

Consider $u\,(n) = n + d$ as introduced in (3.73), where $R(\phi)/\phi \to 1$ as $\phi \to \phi_c = \infty$ and with (5.15) we have $j_{min} = \rho$. As an example in Figure 5.6 we consider $d = 1$, and using (3.74) in this case we have the following explicit expressions

$$\ln z\,(\phi) = \ln \tfrac{e^\phi - 1}{\phi} \quad R\,(\phi) = \phi - 1 + \tfrac{\phi}{e^\phi - 1} \quad \text{for} \quad d = 1\ . \tag{5.38}$$

As in (5.35), the travelling wave cost diverges in the limit of $\phi_2^o \to \phi_c = \infty$. Furthermore, we have that $x \to 0$ and $v_s \to 1$ as $j \to j_{min} = \rho$, so in this case the travelling wave profiles in the limit $j \to j_{min}$ do not correspond to a condensed profile with a spatially fixed condensate. We do not show a contour plot of the Jensen-Varadhan functional (5.12), since it looks qualitatively the same as the one in Figure 5.5 for general unbounded rates, with the exception that constraint curves (5.10) are defined only for $\phi_1 < j - \rho$ and exist up to currents $j \geq j_{\min} = \rho$.

Using (5.19) the condensed cost $E_c^L(j)$ increases linearly in the system size for large L as

$$E_c^L\,(j) = u\big((\rho - R(j))L\big) \approx (\rho - R(j))L\ . \tag{5.39}$$

So as long as $j > \rho$ phase separated states with an L-independent cost dominate the rate function and we have

$$I(j) = \begin{cases} E_{tw}(j) & ,\ j \in (\rho, J(\rho)] \\ \infty & ,\ j \in [0, \rho] \end{cases}\ , \tag{5.40}$$

in accordance with (5.5). As in the previous section, on finite systems we expect condensed profiles to also be relevant for small currents. For this system in fact

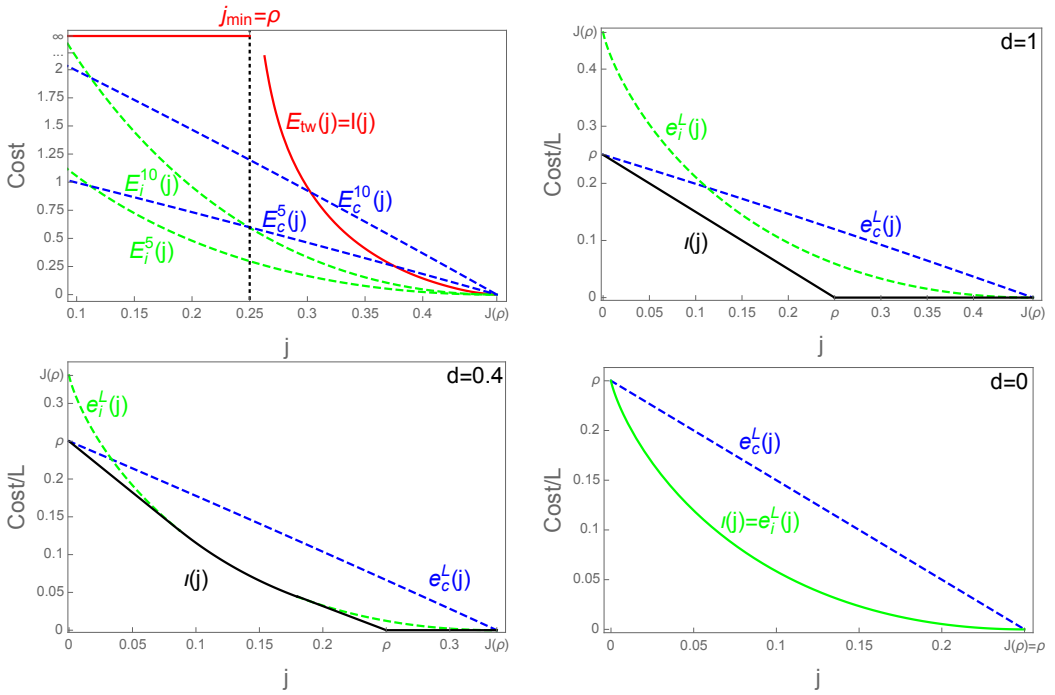

Figure 5.6: All plots feature the ZRP with rates $u(n) = n + d$ and $\rho = 0.25$. (Top left) The cost is plotted against the current for $d = 1$, and in accordance with (5.5) the rate function is given by $I(j) = E_{tw}(j)$ (full red). The costs $E_c^L(j)$ (5.39) and $E_i^L(j)$ (5.41) are shown for small L in dashed blue and green lines, respectively. The other plots illustrate the modified LDP (5.43) with speed Lt for different values of $d \geq 0$, showing the rescaled costs $e_c(j)$ (blue) and $e_i(j)$ (green) (see (5.44)), and the resulting limiting rate function $\iota(j)$ as a full black line for $d > 0$. For independent particles with $d = 0$ (bottom right), the rate function is dominted completely by $e_i(j)$ (green).

a modified large deviation principle with speed Lt instead of t holds in the limit $L \to \infty$, which is illustrated in Figure 5.6 together with (5.40).

Since the condensed cost is of order L, we also have to include in the cost comparison the option of slowing down the jump rates at all lattice sites considering them independently of each other. So, the outgoing current from each site is regarded as a Poisson process with rate $J(\rho)$. In a similar fashion to (5.19), the cost to slow down all the sites independently is approximately given by

$$E_i^L(j) = L\Big(J(\rho) - j + j \log \frac{j}{J(\rho)}\Big) \tag{5.41}$$

We notice that this cost is always of order L and therefore irrelevant in the other

examples. This is equivalent to slowing down the clock of the entire process. Comparing with the cost for condensed profiles, it turns out that $E_i^L(j) < E_c^L(j)$ for a range of j large enough (depending on the parameter d), and as $j \to 0$ we have $E_c^L(0) = L\rho < LJ(\rho) = E_i^L(0)$. This is illustrated in Figure 5.6 for two parameter values $d = 0.4$ and 1. This crossover enters the rate function of the modified LDP with speed tL. In this scaling, the cost of travelling wave profiles is

$$E_{tw}(j)/L \to e_{tw}(j) := \begin{cases} 0 & , \ j \in (\rho, J(\rho)] \\ \infty & , \ j \in [0, \rho] \end{cases} \quad \text{as } L \to \infty \ , \tag{5.42}$$

which again dominates the rate function for currents $j > \rho$. Therefore the rate function is given by the lower convex hull of

$$I^L(j)/L \to \iota(j) := \underline{\text{conv}}\{e_{tw}(j), e_c(j), e_i(j)\} \quad \text{as } L \to \infty \ , \tag{5.43}$$

which is illustrated by full black lines in Figure 5.6. Here

$$e_c(j) := E_c^L(j)/L \quad \text{and} \quad e_i(j) := E_i^L(j)/L \tag{5.44}$$

are L-independent expressions given in (5.39) and (5.41). For d large enough the rate function is simply linear between $j = 0$ and $j = \rho$ and independent of $e_i(j)$, whereas $e_i(j)$ dominates an increasing part of the convex hull for decreasing d. For the degenerate limiting case of independent particles with $d = 0$ we have $J(\rho) = \rho$ and therefore $e_{tw}(j) = \infty$ for all $j < J(\rho)$ and it does not contribute to the rate function. Then (5.43) is given by the cost $e_i(j)$ of slowing down the clock of the process on all sites, or equivalently slowing down all independent particles as is expected in this case (see Figure 5.6 bottom right).

It is impossibe to numerically confirm the extensive behaviour of the rate function for $j \leq j_{min}$ for $d > 0$, but our heuristics is consistent with the case of independent particles with $d = 0$, for which the rate function is exact. The cases in Figure 5.6 (top left) for very small system sizes are numerically accessibe but contain only between 1 and 3 particles, and are only shown for illustration. We do not expect the rate function measured in such systems to coincide with the lower convex hull of the costs since our theoretical arguments only apply for large enough L.

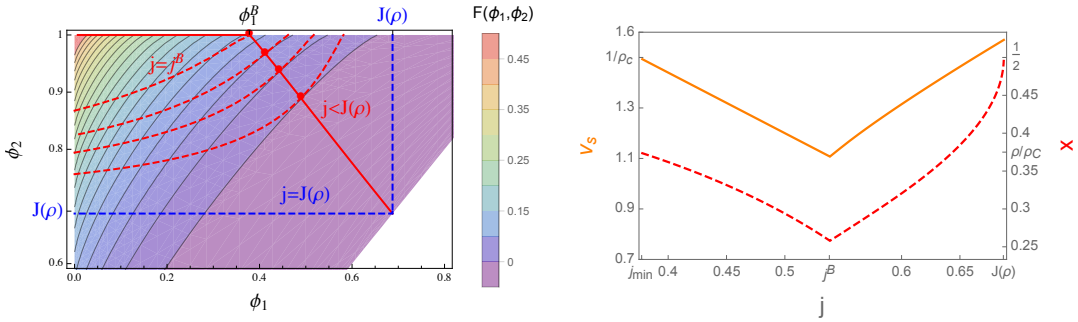

Figure 5.7: Both plots feature the ZRP with rates $u(n) = 1 + b/n$ (3.76) and parameters $b = 3.5$ and $\rho = 0.25$. (Left) The contour plot of the Jensen-Varadhan functional (5.12) is shown together with the constraint curves (5.10) for several values of $j < J(\rho)$ (dashed red) and optimal pairs (full red) analogous to Figure 5.1. For $j < j^B$ optimal pairs correspond to boundary minimizers with $\phi_2^o = 1$ as explained in the text, with corresponding value $\phi_1^B < j_B$. (Right) The red dashed line is the optimal high density fraction x (5.9) as a function of the conditioned current j, while the full orange line is the profile speed v_s. Note that both quantities are plotted on different scales with two ordinate axes. They are not monotone and have a minimum at j^B, as opposed to the constant rate case shown in Figure 5.4 right.

5.1.3.4 Condensing TAZRP

In this section we discuss rates $u(n) = 1 + b/n$ with $b > 2$ as given in (3.76), which exhibit condensation and have a bounded range of currents $\phi \in [0, 1]$ as well as densities with $R(1) = \rho_c = 1/(b-2)$. We focus on total densities $\rho < \rho_c$. The contour plot shown in Figure 5.7 (left) for $b = 3.5$ and $\rho = 0.25$ now includes the upper boundary $\phi_2 = 1$ for the possible values of optimal pairs, as opposed to Figure 5.1 for the constant rate case. The red line indicates the optimal pairs (ϕ_1^o, ϕ_2^o) conditioned on $j_{min} < j < J(\rho)$, where with (5.15) and (3.78) $j_{min} = \frac{\rho}{\rho_c} = \rho(b-2) < 1$. For the parameters in Figure 5.7 there exists a current value $j^B \in (j_{min}, J(\rho))$ where the optimum of the Jensen Varadhan functional switches between a bulk local and a boundary minimizer with $\phi_2^o = 1$. This leads to a non-monotone behaviour of the high density fraction x and the speed v_s of the profile, as shown in Figure 5.7 (right). It also leads to a kink in the cost curve $E_{tw}(j)$ at $j = j^B$. This kink is hard to observe numerically for interesting parameter values and not of particular interest as $E_{tw}(j)$ remains a convex function.

In general, since $\phi_1^o \to 0$ as $j \to j_{min}$, the profile speed (5.18) satisfies

$$v_s = \frac{1-\phi_1^o(j)}{\rho_c - R(\phi_1^o(j))} \to \frac{1}{\rho_c} \quad \text{as } j \to j_{min} \ , \tag{5.45}$$

and

$$x = \frac{j-\phi_1^o(j)}{1-\phi_1^o(j)} \to j_{min} = \frac{\rho}{\rho_c} \quad \text{as } j \to j_{min} \ . \tag{5.46}$$

We can also again commute limits due to continuity of F and get from (5.12)

$$\lim_{j \to j_{min}} F(\phi_1^o(j), \phi_2^o(j)) = F(0,1) = 1 - \frac{\ln z(1)}{\rho_c} = 1 - (b-2)\ln\frac{b}{b-1} \ , \tag{5.47}$$

which is finite and depends only on the parameter b. This is the maximum of the cost curve $E_{tw}(j)$ attained at $j = j_{min} = \rho(b-2)$ shown in Figure 5.8 for two different values of ρ. As in the constant rate case (5.33), the limiting condensed cost is given by the simple expression $E_c(j) = 1 - j + j\ln j < \infty$ independently of all system parameters and valid for all $j \in [0, J(\rho)]$. Depending on the parameters $b > 2$ and $\rho < \rho_c$, the costs $E_{tw}(j)$ and $E_c(j)$ may or may not intersect, as is illustrated in Figure 5.8. In fact, for any fixed $b > 2$, there exists ρ small enough such that $E_{tw}(j) \leqslant E_c(j)$ for all $j \in [j_{min}, J(\rho)]$. To obtain the largest such ρ, we can compare (5.47) with the condensed cost at $j = j_{min}$ to obtain the condition

$$\rho - \ln z(1) \leqslant \rho \ln\left(\frac{\rho}{\rho_c}\right), \tag{5.48}$$

which can be solved numerically and is used in Figure 5.8 (Right).

Since $j_{min} > 0$ and the traveling wave and condensed cost both occur on the same scale, in this case the rate function is given by the non-trivial convex combination of both costs as in (5.6), illustrated by full black lines in Figure 5.8. In the example plotted the right endpoint of the convex hull coincides with $j = j^B$, where $E_{tw}(j)$ exhibits a (hardly visible) kink. While the kink facilitates this behaviour, it does not hold in general and there are parameter values where the convex hull starts above or below j^B. The crossover from travelling wave profiles to condensed states in the realization of current large deviations corresponds to a dynamical phase transition. For currents j in the affine region of the rate function $J(\rho)$, the large deviation is realized by a temporal mixture between travelling wave and condensed profiles in analogy to classical phase separation phenomena (see e.g. [80, 82]). The dynamical phase transition is confirmed by numerical results presented in the next subsection, which require a detailed consideration of finite size

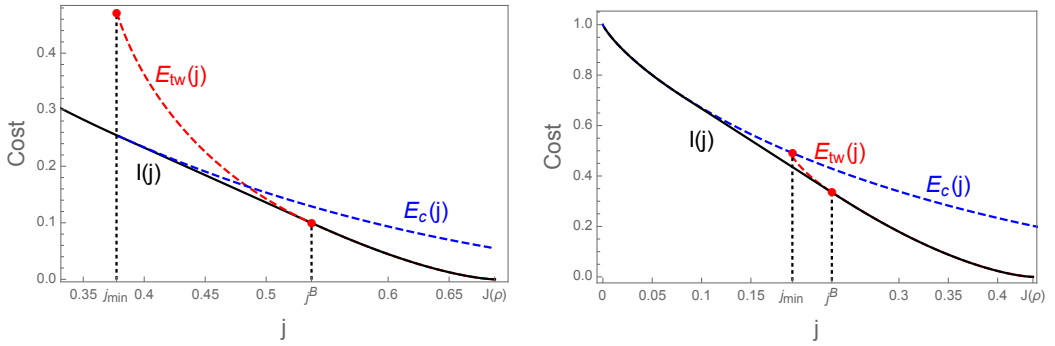

Figure 5.8: Cost functions $E_{tw}(j)$ (5.13) for travelling waves (red dashed) and $E_c(j)$ (5.33) for condensed profiles (blue dashed) for rates (3.76) with $b = 3.5$. The rate function $I(j)$ is given by the lower convex hull (full black) in accordance with (5.6). Note that different ranges on the axes are used. For $\rho = 0.25$ (left) travelling wave and condensed cost curves intersect. For $\rho = 0.12634$ (right) obtained from condition (5.48) $E_{tw}(j)$ and $E_c(j)$ just touch, and for smaller density values they do not intersect.

corrections to the above arguments.

5.1.3.5 Numerical Results for the Condensing TAZRP

We numerically approximate the scaled cumulant generating function $\lambda(k)$ given in (4.10) using a cloning algorithm approach (see e.g. [37]), which is explained in Appendix C. The finite-size rate function I^L is then approximated by numerically performing the Legendre-Fenchel transform (4.4) of the generated data. The results for the ZRP with rates (3.76) with $b = 3.5$ and density $\rho = 0.25$, are shown in Figure 5.9 (left), and agree well with our theoretical prediction after finite size corrections. The finite-size cost functions $E_c^L(j)$ and $E_{\text{tw}}^L(j)$ are defined using the canonical current density relation $J_{L,N} = \langle u \rangle_{L,N}$ with $N = [\rho L]$ as given in [43], in place of the limiting current $J(\rho)$. It is well known that $J_{L,N} = Z_{L,N-1}/Z_{L,N}$, and it can be computed exactly using the recursion $Z_{L,N} = \sum_{k=0}^{N} w(k)\, Z_{L,N-k}$ for the partition function (see e.g. [18] and references therein). For finite L, the maximum current is larger than the limiting value, $\phi_c^L > \phi_c = 1$, and the current is known to significantly differ from its limiting behaviour above the critical density [18]. Inversion of this function defines the density $R^L(\phi)$ as a function of the current. This leads to a finite-size version of the Jensen-Varadhan functional (5.12) $F^L(\phi_1, \phi_2)$ and of the constraint function $G^L(\phi_1, \phi_2)$, which are used as in (5.13) to define a finite-size version of $E_{tw}^L(j)$. The density $R^L(j)$ is also used in (5.19) to define a finite-size corrected version of E_c^L. The resulting finite size corrections to the predicted rate

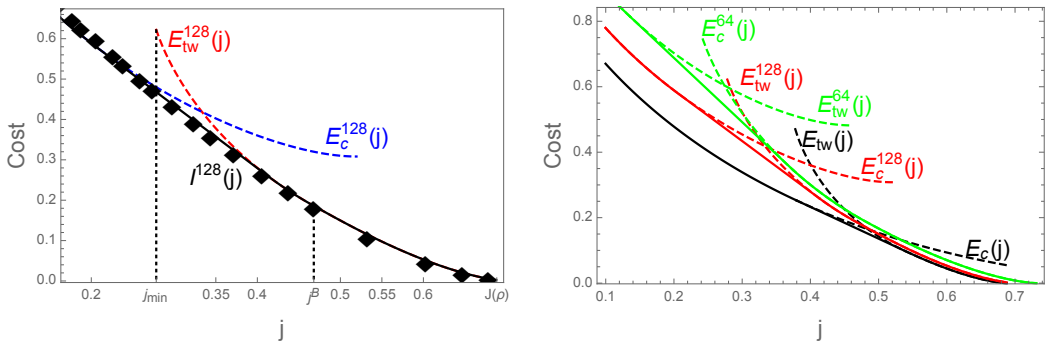

Figure 5.9: Both plots feature the ZRP with rates $u(n) = 1 + \frac{b}{n}$ defined in (3.76) with parameters $\rho = 0.25$ and $b = 3.5$. (Left) Numerical data (black diamonds) obtained from the cloning algorithm are compared to finite-size cost functions E_{tw}^L (red dashed) and E_c^L (blue dashed) for $L = 128$, and coincide very well with the predicted rate function I^L given by the lower convex hull (full black). (Right) Finite-size corrections for cost functions E_{tw}^L and E_c^L (dashed) and the corresponding rate function I^L (full) for $L = 128$ (red) and $L = 64$ (green) are compared with the limiting prediction (black).

function are significant, as shown in Figure 5.9 (right).

The simulations used to calculate the moment generating function $\lambda(k)$, are performed in an ensemble where the average integrated current is fixed by the conjugate parameter k, rather than conditioning the path distribution on a current j. Both parameters a conjugate, and the average current $j(k)$ for a given value of k is given by $\partial_k \lambda(k)$. Affine regions of the rate function I correspond to discontinuous derivatives of $\lambda(k)$, and cannot be explored by the cloning algorithm. On finite systems these effects are smoothed out somewhat, which leads to sparse data points from the simulations in the affine regions of the rate function. However, from simulations with a cloning ensemble it is not possible to directly observe temporal mixtures, which realize such large deviation events for the original ZRP conditioned on a current j in the affine region of the rate function.

5.2 TAIP

The strategy outlined in the preceding section for the TAZRP can also be used to address the same question about current fluctuations for the TAIP whose generator is given by

$$\hat{M}_{IPring} = \sum_{x=1}^{L} \left[\hat{c}_{x+1}\hat{a}_x \left(\hat{u}_x \hat{v}_{x+1}\right) - \hat{u}_x \hat{v}_{x+1}\right] \tag{5.49}$$

where, as for the TAZRP, the spatial part reduces to $q = 0$ and $p = 1$. As explained in Section 3.2.3, we assume that the jump rates related to the arrival site has the form $\hat{v}_x = \hat{u}_x + d$ and $\hat{u}_x |\eta\rangle = \eta_x |\eta\rangle$.

5.2.1 Adapting the JV approach

From the point of view of the conservation law (4.54), the main difference between the two models is the sign of the second derivative of the stationary current: the $J(\rho)$, given in (3.81), for the IP is convex. In this case, as it was explained in Section 4.3.2, the down shock (up shock) is stable (unstable) with velocity

$$v_s(\rho_1, \rho_2) = d + \rho_1 + \rho_2. \tag{5.50}$$

This also implies that the travelling wave profile decomposition, which for the IP is more conveniently expressed in the density space

$$j = (1 - x) J(\rho_1) + x J(\rho_2) \tag{5.51}$$

$$\rho = (1 - x) \rho_1 + x \rho_2, \tag{5.52}$$

leads to upper current fluctuations as can be seen in Figure 5.10. So $j_{max} = \infty$ and all $j > J(\rho)$ are accessible by JV profiles. In the same way, the minimum value of the high density phase is determined from the line passing through the points $(0, 0)$ and (j, ρ) and is equal to $\rho_2^{min} = \frac{j - d\rho}{\rho}$. As we did for the ZRP, the function ruling the set of admissible pairs (ρ_1, ρ_2) for the couple of values (ρ, j) can be obtained by solving (5.51) w.r.t. x and is given as

$$G(\rho_1, \rho_2) = d\rho - \rho_1 \rho_2 + \rho(\rho_1 + \rho_2) = j, \tag{5.53}$$

which implies

$$\rho_2(\rho_1) = \frac{j - \rho(d + \rho_1)}{\rho - \rho_1}. \tag{5.54}$$

To determine the JV cost function, we need first to write the relevant entropy-entropy-flux pair. Using again the definition of the thermodynamic entropy we have that

$$h(\rho) = \rho \ln\left(\frac{\rho}{d + \rho}\right) + d \ln\left(\frac{d}{d + \rho}\right) \tag{5.55}$$

and

$$g(\rho) = \rho \left[(d + \rho) \ln\left(\frac{\rho}{d + \rho}\right) - d\right], \tag{5.56}$$

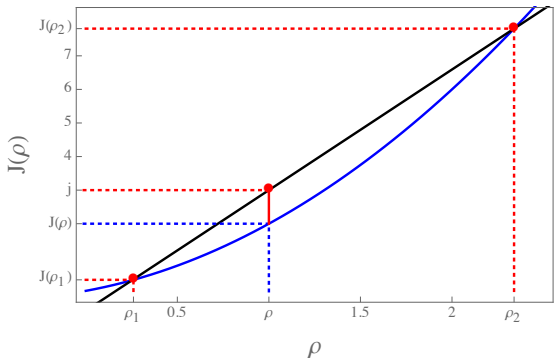

Figure 5.10: The blue curve depicts the current density relation of the TAIP with $d = 1$. Given a value $j \neq J(\rho)$, the point (ρ, j) identifies a pencil of lines. Those which intersect the blue curve in two points highlight admissible pairs (ρ_1, ρ_2) with $\rho_1 < \rho_2$ for the travelling wave decomposition (5.51) as expressed in (5.53). The couple (ρ_1^o, ρ_2^o) which optimize the cost is obtained from (5.59). As we can see from the vertical full red line, only travelling waves obtained from upper current fluctuations can be studied.

as can be verified by direct substitution in $g'(\rho) = J'(\rho) h'(\rho)$. In this way, for the IP, the JV rate function is given by the explicit expression

$$\mathcal{F}(\rho_1, \rho_2) = d(d + \rho_1 + \rho_2) \ln\left(\frac{d+\rho_1}{d+\rho_2}\right) + \rho_1\rho_2 \ln\left(\frac{\rho_2}{\rho_1}\frac{d+\rho_1}{d+\rho_2}\right) + d(\rho_2 - \rho_1). \quad (5.57)$$

As mentioned before, it is important to notice that w.r.t. the ZRP case, the positions of the shock and of the rarefaction fan are, in the typical evolution of the step profiles, interchanged. This means that the correct rate function for the TAIP is $\mathcal{F}(\rho_2, \rho_1)$ (not $\mathcal{F}(\rho_1, \rho_2)$) with associated cost

$$E_{tw}(j) = \inf_{\rho_1, \rho_2} \{\mathcal{F}(\rho_2, \rho_1) : G(\rho_1, \rho_2) = j\} \in [0, \infty]. \quad (5.58)$$

The minimizer of the preceding expression can be obtained from the system of equations as in (5.14)

$$\begin{cases} \partial_1\mathcal{F}(\rho_2, \rho_1)\,\partial_2 G(\rho_1, \rho_2) - \partial_2\mathcal{F}(\rho_2, \rho_1)\,\partial_1 G(\rho_1, \rho_2) = 0 \\ G(\rho_1, \rho_2) = j \end{cases}, \quad (5.59)$$

whose first equation is given explicitely as

$$(\rho_1 - \rho_2)\left[\rho \ln\left(\frac{\rho_2}{d+\rho_2}\frac{d+\rho_1}{\rho_1}\right) + d \ln\left(\frac{d+\rho_1}{d+\rho_2}\right)\right] = 0. \quad (5.60)$$

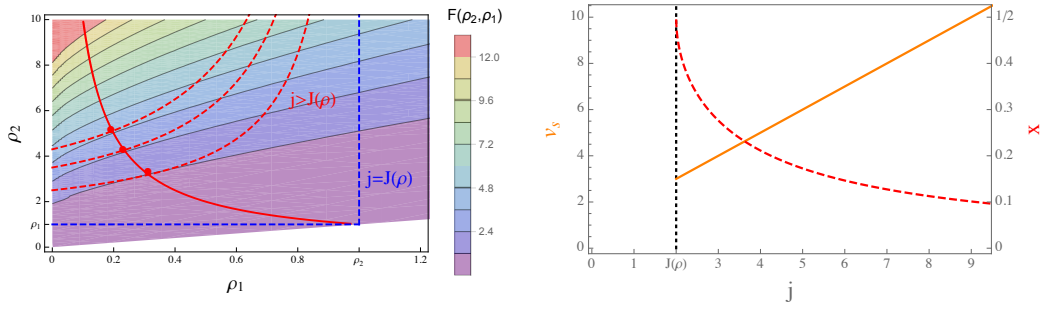

Figure 5.11: (Left) In the background, the contour plot of the JV cost function (5.57) for $\rho = 1$ and $d = 1$ is reported. Red dotted constrained curves are given from (5.54) for different values of j but fixed ρ. The full red curve consists of the optimal pair of points (ρ_1^o, ρ_2^o) for different values of j. (Right) Given the optimal density pairs, the profile speed (orange curve) is obtained from (5.50), while the volume fraction (red dotted curve) is obtained from (5.61). As we can see from the latter, in the stationary state the system is equally split in the high and low density phase. Increasing j implies a decrease of the extension of the high density phase.

We notice that for $\rho_1 = \rho_2$, which corresponds to the stationary regime with $j = J(\rho)$, the minimization condition is always satisfied. The solution of the optimization problem in (5.59) can be solved numerically and is illustrated in Figure 5.11 together with the plots of the optimal shock speed $v_s(\rho_1^o, \rho_2^o)$ and space subdivision parameter (like in (5.9))

$$x = \frac{j - J(\rho_1^o)}{J(\rho_2^o) - J(\rho_1^o)}. \tag{5.61}$$

Substituting the set of optimal values (ρ_1^o, ρ_2^o), reported in Figure 5.11, in the JV function $\mathcal{F}(\rho_2^o, \rho_1^o)$ gives rise to a monotone increasing cost function illustrated in Figure 5.12 together with its associated SCGF.

5.2.2 Ansatz for Lower Current Deviations

As shown for the unbounded sublinear and asymptotically linear rates in Sections 5.1.3.2 and 5.1.3.3, respectively, for the TAZRP, the cost to see lower current deviations for the TAIP scales linearly with the system size. For the IP jump rates, the cost to slow down a Poisson process (which is related to the formation of a condensate as shown in (5.19)) is

$$E_c^L(j) = (\rho - R(j))\, L(d + R(j)) - j + j \ln \frac{j}{(\rho - R(j))\, L(d + R(j))}, \tag{5.62}$$

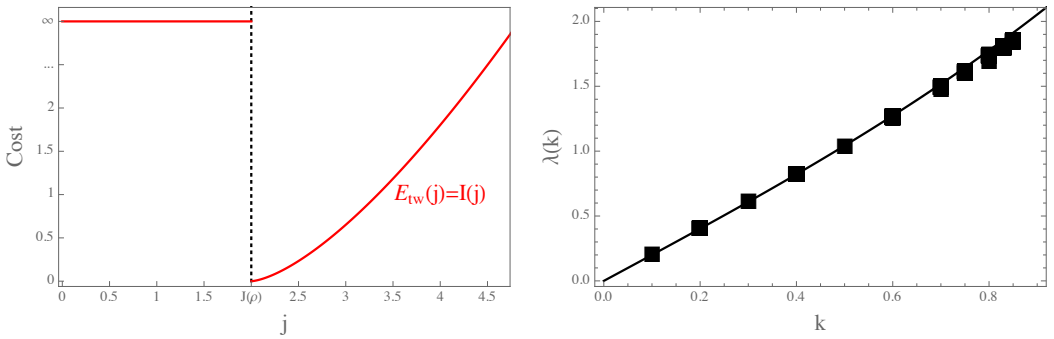

Figure 5.12: For $\rho = 1$ and $d = 1$, (Left) plot of the JV cost function $\mathcal{F}\left(\rho_2^o, \rho_1^o\right)$. The function is convex and monotone increasing since we are looking at upper current deviations, as opposite to the ZRP in which lower current deviation gave as a result convex monotone decreasing cost. (Right) SCGF associated to the JV cost. Black diamond points are obtained from a cloning algorithm simulation with system size $L = 128$, running time L and 2^{15} clones.

which becomes for L large

$$\begin{aligned} e_c \coloneqq \frac{E_c^L}{L} \simeq & \left(\rho - R\left(j\right)\right)\left(d + R\left(j\right)\right) \\ = & \rho\left(d + R\left(j\right)\right) - j \\ = & J\left(\rho\right) - j - \rho\left(\rho - R\left(j\right)\right). \end{aligned} \tag{5.63}$$

Again, the cost to uniformly slow the rate at all sites, as in (5.41), is

$$e_i \coloneqq \frac{E_i^L}{L} = J\left(\rho\right) - j + j \ln \frac{j}{J\left(\rho\right)}. \tag{5.64}$$

Since for the IP the factorised form of the jump rates puts in relation two sites, it is possible to exploit this correlation to generate hyperuniform states. It turns out that these correspond to sites alternating high and low particle densities whose cost we determine in the following. Given two nearest-neighbouring sites, we can distribute the density of the two sites as $\rho_1 + \rho_2 = 2\rho$, where $\rho_1 \leqslant \rho \leqslant \rho_2$. This corresponds to two typical currents across bonds, $\rho_1\left(d + \rho_2\right) < \rho_2\left(d + \rho_1\right)$. In this way, we can slow down the site with the higher density to the current of the lower one (intuitively it is not possible to accelerate the current from the lower density site since it lacks the necessary particles to increase the rates). So, by writing $\rho_1 = 2\rho - \rho_2$, the target conditioning current of the TAIP is

$$j = \left(2\rho - \rho_2\right)\left(d + \rho_2\right), \tag{5.65}$$

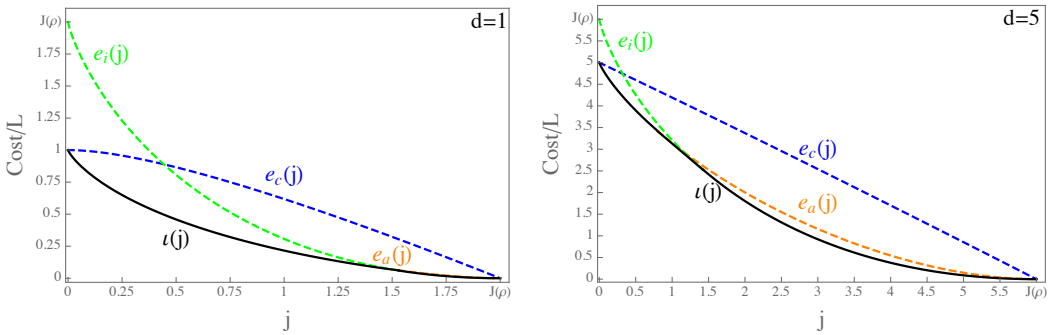

Figure 5.13: Plots of the intensive cost function, as given in (5.68), for lower current deviations of the IP on a ring with $\rho = 1$ and for different values of d. The case $d = 1$ is the reference value for the IP in the present thesis, while we also report $d = 5$, which shows qualitatively similar features to $d = 1$, since it better displays the presence of a convex hull which does not coincide with any of the coloured curves. As we can see, in both cases the resulting convex hull is not affected by the condensate cost.

and the resulting cost

$$\begin{aligned} e_a^L(j) \coloneqq \frac{E_a^L(j)}{L} =& \frac{1}{2}\left(\rho_2(d+\rho_1) - j + j\ln\frac{j}{\rho_2(d+\rho_1)}\right) \\ =& \frac{1}{2}\left(\rho_2(d+2\rho-\rho_2) - j + j\ln\frac{j}{\rho_2(d+2\rho-\rho_2)}\right), \end{aligned} \tag{5.66}$$

where the prefactor $\frac{1}{2}$ takes into account that only half of the sites, which correspond to the high density subset of the lattice, are slowed down. We can see that the above current conditioning give rise to decreasing value simply by calculating the first derivative

$$\frac{dj}{d\rho_2} = -d + 2\rho - 2\rho_2 < 0 \quad \text{for all } \rho_2 \geqslant \rho \ . \tag{5.67}$$

Also, (5.65) determines $\rho_2(j)$ to be inserted in (5.66) for a given j, which is the unique solution greater than ρ of the quadratic equation. In the end, the resulting cost function is given by the convex hull

$$\iota(j) \coloneqq \underline{\text{conv}}\{e_a(j), e_c(j), e_i(j)\} \quad \text{as } L \to \infty \ , \tag{5.68}$$

as illustrated in Figure 5.13. Our ansatz for the alternating profiles cost assumes product measures with alternating densities. In general, a hyperuniform state with long range correlations might have a different cost, but still proportional to L. States with finite or even slowly decaying correlations do not change the associated current

on a macroscopic scale, and there are no known examples where they contribute to current large deviations. By monotonicity arguments, one can see that other splits of the mass in alternating profiles lead to costs in between $e_a(j)$ and $e_i(j)$ and should therefore not contribute to the rate function.
For the ZRP, alternating profiles do not provide different currents j than phase separated one due to the zero-range interaction, and therefore do not have to be considered.

CHAPTER 6

Large Deviations for Partially Asymmetric SPS on a Ring

As we have seen, the JV approach, which was rigorously proved for the TASEP, can be applied to the TAZRP and TAIP. Here, we will show how to extend the heuristics developed in Chapter 5 to the case of partial asymmetry for the ZRP as well as IP. In terms of the rate function, this will result in an explicit dependence on the drift $(p-q)$. For the ZRP, we will also study the large deviations of the current which are outside of the range of validity of the JV scheme. The present thesis part relies on Chapter 5 and most of the considerations developed before are still valid in this context.

6.1 JV for Partial Asymmetry

In this section, we will go through the main equations behind the JV approach with a particular focus on the role of the asymmetry.
To set the notation, we recall the general definition of stationary current density in (3.64) and write

$$J_{PA}(\rho) \coloneqq (p-q)\langle u(\eta_x)\rangle_* \langle v(\eta_x)\rangle_* =: (p-q)\, J_{TA}(\rho). \tag{6.1}$$

The first step in the JV scheme is to determine an entropy-entropy-flux pair. For the PA case, a similar relation to (4.65) holds

$$\partial_\rho g_{PA}(\rho) = \partial_\rho J_{PA}(\rho)\, \partial_\rho h_{PA}(\rho). \tag{6.2}$$

We notice that the stationary measure (3.29) and the fugacity is unaffected by the partial asymmetry. Recalling (4.72), this implies for the entropy that $h_{PA}(\rho) =$

$h_{TA}(\rho)$. So we have

$$g_{PA}(\rho) = (p-q)\, g_{TA}(\rho), \tag{6.3}$$

as can be seen by direct substitution in (6.2). From (4.69), the JV function for partial asymmetric systems is then

$$\mathcal{F}_{PA}(\rho_1, \rho_2) = (p-q)\, \mathcal{F}_{TA}(\rho_1, \rho_2). \tag{6.4}$$

Again, in the same way, the travelling wave decomposition (5.10) becomes

$$G_{PA}(\rho_1, \rho_2) = \frac{\rho\left(J_{PA}(\rho_2) - J_{PA}(\rho_1)\right) - J_{PA}(\rho_2)\,\rho_1 + J_{PA}(\rho_1)\,\rho_2}{\rho_2 - \rho_1} \tag{6.5}$$

$$= (p-q)\, G_{TA}(\rho_1, \rho_2). \tag{6.6}$$

The cost function (5.13) resulting from the optimization problem (5.14) can be used to determine its partial asymmetric counterpart. In fact,

$$E_{tw}^{TA}(j) = \inf\left\{\mathcal{F}_{TA}(\rho_1, \rho_2) : G_{TA}(\rho_1, \rho_2) = j\right\} \tag{6.7}$$

$$= \frac{1}{p-q} \inf\left\{\mathcal{F}_{PA}(\rho_1, \rho_2) : G_{PA}(\rho_1, \rho_2) = (p-q)\, j\right\} \tag{6.8}$$

$$= \frac{1}{p-q} E_{tw}^{PA}((p-q)\, j), \tag{6.9}$$

which by rearranging the terms becomes

$$E_{tw}^{PA}(j) = (p-q)\, E_{tw}^{TA}\left(\frac{j}{p-q}\right). \tag{6.10}$$

Next, we will see the results of the partially asymmetric version of the JV approach for the two models considered in this thesis.

PAZRP - In this case, we need to determine the partially asymmetric version of the condensed states cost function. In the same fashion as before, recalling that for the TAZRP $J_{TA}(\rho) = \Phi(\rho)$, we can write the finite size cost (5.19) as

$$E_c^{PA}(j) = (p-q)\, u\left(\left(\rho - R(j)\right) L\right) - j + j \ln \frac{j}{(p-q)\, u\left(\left(\rho - R(j)\right) L\right)}, \tag{6.11}$$

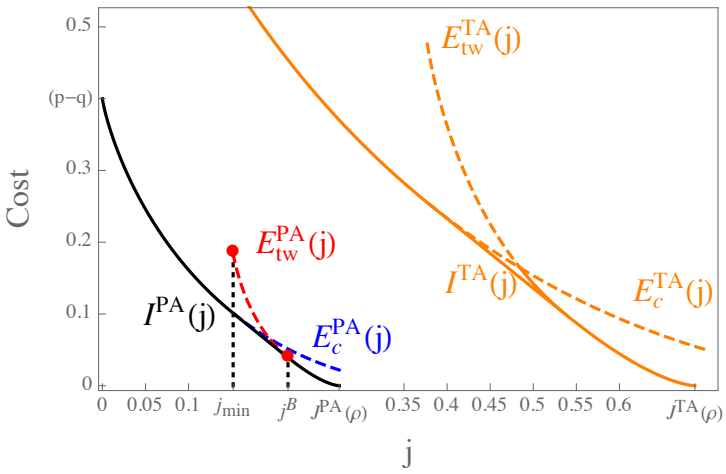

Figure 6.1: PAZRP cost plot for $b = 3.5$, $\rho = 0.25$ and $p = 0.7$. (Black) Large deviation rate function resulting from the convex hull (6.13). At $j = 0$ the function takes a finite value equal to $(p - q)$. (Red) JV cost funcion (6.10). (Blue) Condensate cost function (6.12). (Orange) Total asymmetry analysis as in Figure 5.8. As we can see in comparison, the partial asymmetry does not change the qualitative properties of the large deviation behaviour. However, we see that the cost to produce small currents increases for increasing asymmetry p.

since the contribution to the current from the condensate is equal to $(p - q)\, u\left((\rho - R(j))\, L\right)$. For $L \to \infty$ we have $u\left((\rho - R(j))\, L\right) \simeq 1$ hence

$$E_c^{PA}(j) \simeq (p - q)\, E_c^{TA}\left(\frac{j}{p - q}\right). \tag{6.12}$$

Finally, we conclude that the cost function convex hull is given as before like

$$I^{PA}(j) = \underline{\text{conv}}\left\{E_{tw}^{PA}, E_c^{PA}\right\}(j) \quad \text{for all } 0 < j < J(\rho), \quad \text{if } \rho_c < \infty\ . \tag{6.13}$$

The resulting cost function plot can be found in Figure 6.1 and 6.2.

PAIP - For this model, only the travelling wave cost contribution is involved and the results, which can be found in Figure 6.3 below, follow the analysis and conclusions as in the TAIP.

6.2 PAZRP Beyond the JV approach

The presence of partial asymmetry introduces additional randomness and allows fluctuations also at the level of the spatial part. In fact, it is possible to reach a goal

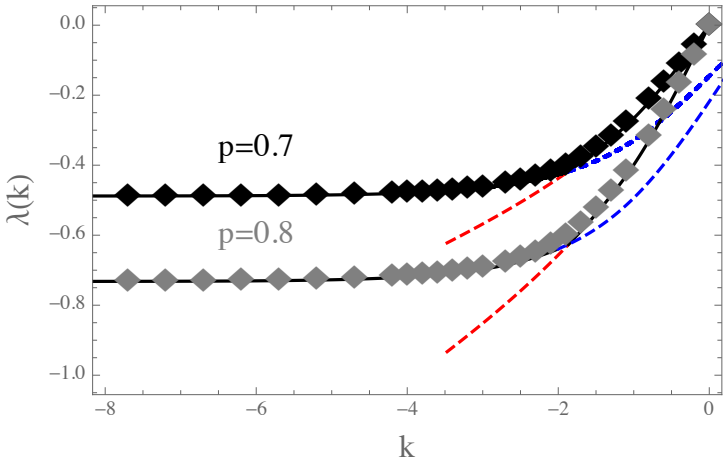

Figure 6.2: SCGF for PAZRP given jump rates $u(n) = 1 + \frac{b}{n}$ and parameters $b = 3.5$, $\rho = 0.25$ with different value of asymmetry (as reported in the Figure), together with data points obtained from a simulation performed using the cloning algorithm (using 2^{15} clones, $L = 64$ and running time L^2). The red (blue) dashed curve is the SCGF of the JV (condensate) rate function, while the full black curve lying under the data points is the SCGF of the resulting rate function convex hull. As can be seen from the plot, large negative values of k are dominated by the condensate regime.

current j with suitably chosen spatial coefficient as

$$(p' - q')\,\Phi(\rho) = j \quad \text{with } p' + q' = 1\ , \tag{6.14}$$

which implies

$$p'(j) = \frac{j + \Phi(\rho)}{2\Phi(\rho)}. \tag{6.15}$$

Using this strategy and due to the presence of the constraint on the spatial coefficients, it is possible to achieve a bounded set of currents $j \in \left[-J^{TA}(\rho), J^{TA}(\rho)\right]$. Thus, exploiting additional randomness due to partial asymmetry allows to obtain also negative atypical currents, which means a particle flow in a direction opposite to the stationary current. Intuitively speaking, the cost to achieve an inverse flow is of order L (since each particle jumping with spatial rate p' and q' is making a large deviation move) so it diverges with the system size. Our ansatz for the cost to condition on an atypical spatial bias is given by the relative entropy formula between the distributions (p, q) and (p', q'),

$$e_{pq}(j) := \frac{E^L_{pq}(j)}{L} := \Phi(\rho)\left(p'(j)\ln\frac{p'(j)}{p} + q'(j)\ln\frac{q'(j)}{q}\right). \tag{6.16}$$

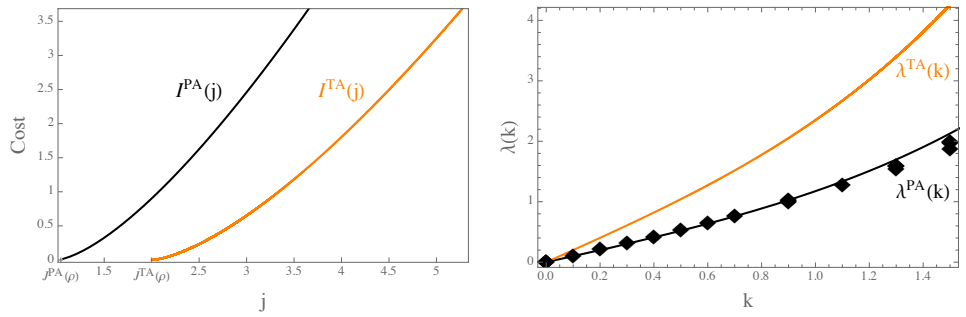

Figure 6.3: (Left) Comparison between the LD rate function (6.13) of the PAIP which is equal to the JV cost (6.10), black curve, with parameters $d = 1$, $p = 0.7$, $\rho = 1$ and TAIP, orange curve. As for the ZRP case, the qualtitative behaviour is left unchanged upon rescaling by $(p - q)$ as in (6.10). (Right) SCGF of the PAIP and TAIP cost functions. Data points correspond to two simulation instances having both 2^{15} clones, $L = 64$ sites but running time L^2 and $5L^2$. The difference in the simulation time is evident in the tail points, which correspond to rarer events, where longer running time leads to points closer to the theoretical curve.

This is the standard rate function to observe an empirical bias (p', q') under repeated independent sampling of a bias variable with distribution (p, q) (see e.g. Chapter II in [25]). To complete the picture, it is possible to achieve currents beyond $\left|J^{TA}(\rho)\right|$ by setting off also the jump rates of the model. In fact, using the same reasoning as for the condensate case in (5.19), increasing the average exit rate of the particles (that is the activity which for the TAZRP satisfies $A(\rho) = J^{TA}(\rho) = \Phi(\rho)$) has a cost function given by the acceleration of a Poisson process from $\Phi(\rho)$ to a value $\hat{\phi} > \Phi(\rho)$

$$e_\Phi\left(\hat{\phi}\right) := \frac{E_\Phi^L\left(\hat{\phi}\right)}{L} := \Phi(\rho) - \hat{\phi} + \hat{\phi} \ln \frac{\hat{\phi}}{\Phi(\rho)}. \tag{6.17}$$

Keeping the asymmetry (p, q) fixed, this mechanism in combination with $j = (p - q)\hat{\phi}$ would lead to a cost function

$$e_J(j) := (p - q)\, e_\Phi\left(\hat{\phi}\right) = J^{PA}(\rho) - j + j \ln \frac{j}{J^{PA}(\rho)}, \tag{6.18}$$

where $J^{PA}(\rho) = (p - q)\Phi(\rho)$. In general the two mechanisms (6.16) and (6.17) can interact. For instance, to obtain an atypical negative current, the system needs to change the spatial bias but, at the same time, it may be more convenient to increase the activity from a certain value of p' onwards. Along the same lines, reaching a current above $J^{PA}(\rho)$ can be achieved as a combination of increasing the asymmetry of the spatial part and the system activity. Leaving $\hat{\phi}$ as a free parameter to optimize

on, we can combine the two costs as

$$\left(p' - q'\right)\hat{\phi} = j \tag{6.19}$$

which gives

$$p'\left(j, \hat{\phi}\right) = \frac{j + \hat{\phi}}{2\hat{\phi}}. \tag{6.20}$$

In the end, the cost function, after optimizing over the free parameter $\hat{\phi}$ which encodes the relative strength of the change in the activity with respect to change of the spatial bias, is given by

$$e_{pq;J}(j) \coloneqq \min_{\hat{\phi}} \left\{ \hat{\phi} \left(p'\left(j, \hat{\phi}\right) \ln \frac{p'\left(j, \hat{\phi}\right)}{p} + q'\left(j, \hat{\phi}\right) \ln \frac{q'\left(j, \hat{\phi}\right)}{q} \right) \right. \tag{6.21}$$

$$\left. + (p - q) \left(\Phi(\rho) - \hat{\phi} + \hat{\phi} \ln \frac{\hat{\phi}}{\Phi(\rho)} \right) \right\}. \tag{6.22}$$

Finally, from (6.13), denoting by

$$\iota^{PA}(j) = \lim_{L \to \infty} \frac{I^{PA}(j)}{L} = \begin{cases} 0 & j \in \left[0, J^{PA}(\rho)\right] \\ \infty & \text{otherwise} \end{cases} \tag{6.23}$$

we can express the optimal cost as the following convex hull

$$\iota(j) \coloneqq \underline{\text{conv}} \left\{ e_{pq;J}, \iota^{PA} \right\}(j) \quad \forall j \in \mathbb{R}. \tag{6.24}$$

The plot of all the mentioned cost function in this section can be found in Figure 6.4. We obtain the corresponding SCGF $\lambda_\infty(k)$ by Legendre-Fenchel transform (6.24), which is shown in Figure 6.5 in comparison with simulation data. To compare data to the asymptotic behaviour as $L \to \infty$, $\lambda(k)$ has to be rescaled as $\frac{1}{L}\lambda\left(\frac{k}{L}\right) \to \lambda_\infty(k)$.

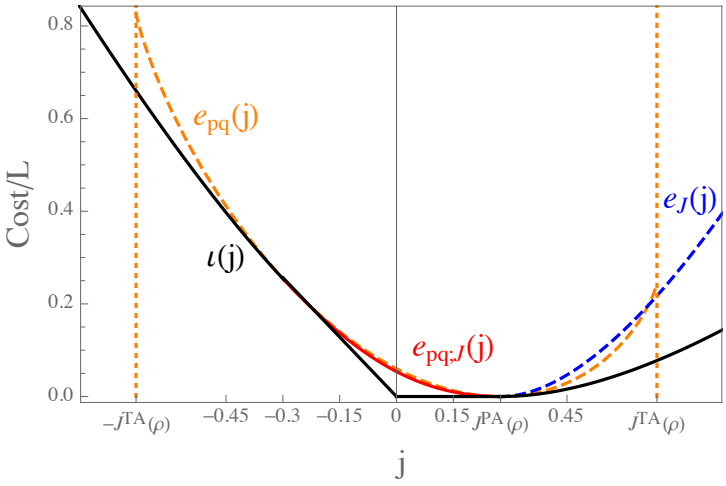

Figure 6.4: Plot of the rescaled cost functions for PAZRP with $p = 0.7$ and $q = 0.3$. Since the JV cost is always finite for $j \in [0, J^{PA}(\rho)]$ the cost on the scale L must be zero in this region (as shown by the black line). It follows that the qualitative features of the plot are independent of the choice of jump rates (which would only shift the position of J^{PA}). In this example, we considered $u(n) = 1 + \frac{b}{n}$ with $b = 3.5$ and $\rho = 0.25$. The full red curve corresponds to the cost contribution as defined in (6.21) giving rise to the convex hull in (6.24), where the flat part of $\iota(j)$ in the range $j \in \left[0, J^{PA}(\rho)\right]$ corresponds to the JV regime. The cost optimizing between spatial and activity contribution given in (6.21) does not coincide with e_{pq} neither e_J, which are shown as dashed lines for comparison.

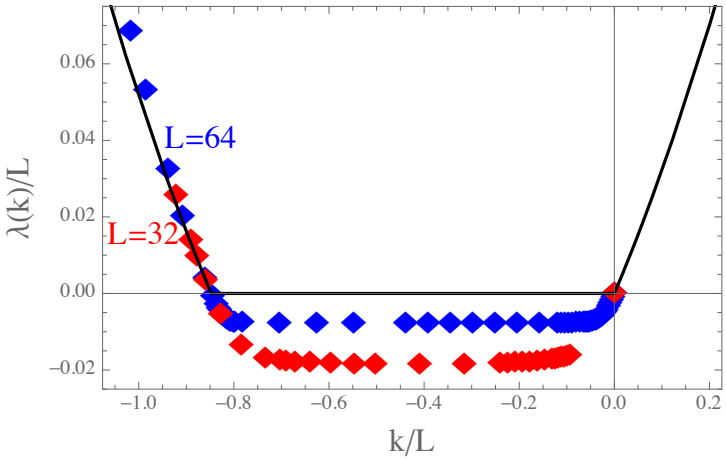

Figure 6.5: The black curve is the SCGF $\lambda_\infty(k)$ corresponding to the rate function (6.24) normalized by the system size for the same ZRP as in Figure 6.4. Data points are obtained from a simulation using the cloning algorithm with 2^{15} clones, L^2 running time and system size $L = 32$ (red), $L = 64$ (blue). The discrepancy between the data points and $\lambda_\infty(k)$ is due to a generic finite size effect smoothing kinks and affine parts of the function, which decreases with L.

CHAPTER 7

Large Deviations for Symmetric SPS with Open Boundaries

In the preceding chapters, we have seen how the Jensen-Varadhan approach can be fruitfully applied to describe the macroscopic large deviation behaviour of the Zero-Range Process, for different classes of jump rates, and the Inclusion Process. Here, we will focus on the open-boundary case with symmetric spatial part and we will study the fluctuations of the macroscopic current for the Inclusion Process only. Next, we will consider the activity, again in the symmetric case, and we will see how to determine its fluctuations from a microscopic view point using an algebraic technique stemming from the quantum matrix form discussed in the Chapter 4. The ideas and methods implemented in this part of the thesis mirror results which were recently obtained for the ZRP in [51].

7.1 MFT Analysis

In section 4.3.3, we expressed the MFT framework in its general version which includes the external field parametrized by 0. In this context, we consider zero external field, that is $\nu = 0$, which from (4.51) gives $p = q = 1$. However, for comparison with the data generated from the numerical simulation, we will consider from now on $p = q = \frac{1}{2}$ without loss of generality. To apply the MFT we need to check that the IP is of gradient type, that is the equation (4.73) must be verified. This can be seen by writing the istantaneous local current with rates given in (3.80) and (3.82)

$$j_{x,x+1}(\eta) = (p-q)\, u(\eta_x)\, u(\eta_{x+1}) + d\,(pu(\eta_x) - qu(\eta_{x+1}))\,, \tag{7.1}$$

from which, in the symmetric case, we clearly deduce that

$$j_{x,x+1}(\eta) = h(\tau_x\eta) - h(\tau_{x+1}\eta) \quad \text{with } h(\tau_x\eta) = \tfrac{d}{2}u(\eta_x) \tag{7.2}$$

Then, the diffusion and mobility coefficients (4.78) of the IP are given by

$$D(\rho) = \tfrac{d}{2} \quad \text{and} \quad \chi(\rho) = \tfrac{1}{2}\rho(\rho + d)\ . \tag{7.3}$$

From the constitutive equation (4.77), the stationary current can be determined in the following way. Since we assume the optimal profile to be stationary, we have $\frac{\partial\rho}{\partial s}(y,s) = 0$ which implies from (4.77) that $J^0(\rho(y), y) = \text{const}$ for all $y \in [0,1]$. This value can be determined by integrating the constitutive equation

$$\int_0^1 J^0(\rho(y), y)\, dy = J^0 = -\frac{d}{2}\int_0^1 \frac{\partial\rho}{\partial y}dy = -\frac{d}{2}\int_{\rho_0}^{\rho_1} d\rho = -\frac{d}{2}(\rho_1 - \rho_0)\,. \tag{7.4}$$

In our example, we considered $\rho_1 > \rho_0$ which implies that the stationary current, when $p = q$, is negative, that is it flows to the left from the larger reservoir to the smaller. To obtain the stationary density profile, we can repeat the same integral on a generic interval $[0, y]$ as

$$\int_0^y J^0(\rho(z), z)\, dz = -\frac{d}{2}(\rho_1 - \rho_0)\, y = -\frac{d}{2}\int_{\rho_0}^{\rho(y)} d\rho = -\frac{d}{2}(\rho(y) - \rho_0)\,, \tag{7.5}$$

which, in the end, gives a straight line connecting the two reservoir densities

$$\rho(y) = (\rho_1 - \rho_0)\, y + \rho_0. \tag{7.6}$$

From the coefficients (7.3), we have explicit versions for the terms $A(\rho)$ and $B(\rho)$ given in (4.84) in order to calculate the optimal stationary density profile. It results that the integral (4.89) gives

$$\begin{aligned}\bar{\rho}_j(y) = \frac{1}{2}\Bigg\{ &\sqrt{\frac{2}{C}\left[j^2 - 2C\chi(\rho_0)\right]}\sin\left(2\frac{\sqrt{2C}}{d}y\right) \\ &+ (d + 2\rho_0)\cos\left(2\frac{\sqrt{2C}}{d}y\right) - d\Bigg\}\end{aligned} \tag{7.7}$$

where C is a constant, which we determine numerically for every choice of the parameters j, ρ_0 and ρ_1, obtained by solving $\bar{\rho}_j(1) = \rho_1$. It is also important to notice that only the square of the current appears in (7.7): this means that

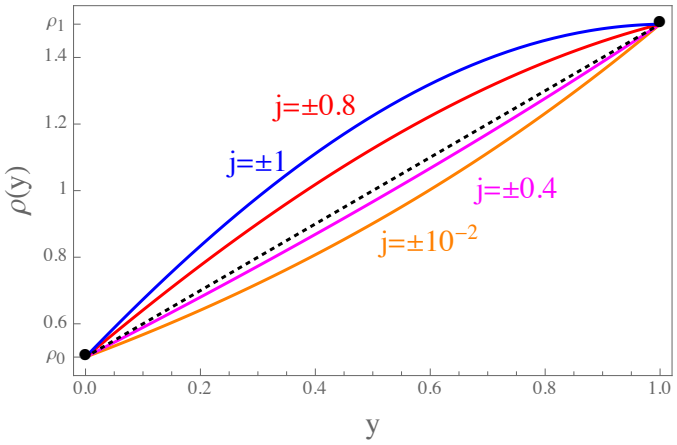

Figure 7.1: Optimal and stationary density profiles of the IP for $p = q = \frac{1}{2}$, $d = 1$, $\rho_1 = 1.5$ and $\rho_0 = 0.5$. The black dots at the top right and at the top left corner highlight the boundary density values. The black dotted line is the stationary profile as in (7.6) which corresponds to the stationary current $-\left|J^0\right| = -\frac{d}{2}(\rho_1 - \rho_0) = -0.5$. As explained in the main text, current conditioning for $j > \left|J^0\right|$ give rise to concave optimal profile, while for $j < \left|J^0\right|$ the density is convex.

corresponding forward and backward currents are generated from the same optimal profile. Since in this case we consider $\nu = 0$, from (4.87) we have

$$j^2 = \left(D\left(\bar{\rho}_j\right)\right)^2 \left(\frac{d\bar{\rho}_j}{dy}\right)^2 + 4C\chi\left(\bar{\rho}_j\right). \tag{7.8}$$

When $C = 0$, the above equation reduces to

$$j^2 = \left(D\left(\bar{\rho}_j\right)\right)^2 \left(\frac{d\bar{\rho}_j}{dy}\right)^2 = \left(J^0\right)^2, \tag{7.9}$$

which is the typical current as results from the constitutive equation (4.77) and the optimal profile coincides with (7.6) (see black dotted line in Figure 7.1). The case when $C < 0$ corresponds to conditioning on currents smaller than the typical one, more precisely $j \in \left(-J^0, J^0\right)$. The optimal profile turns out to be given by

$$\begin{aligned}\bar{\rho}_j^{-}(y) :=& \frac{1}{2}\left\{\sqrt{\frac{2}{|C|}\left(j^2 + 2|C|\chi\left(\rho_0\right)\right)}\sinh\left(2\frac{\sqrt{2|C|}}{d}y\right)\right. \\ &\left. + (d + 2\rho_0)\cosh\left(2\frac{\sqrt{2|C|}}{d}y\right) - d\right\},\end{aligned} \tag{7.10}$$

as can be obtained from (7.7) using the identities $\sinh(x) = i^{-1}\sin(ix)$ and $\cosh(x) = \cos(ix)$, where i is the imaginary unit. By definition, the density profile is positive on its domain. This implies that

$$\sqrt{\frac{2}{|C|}\left(j^2 + 2|C|\,\chi(\rho_0)\right)}\sinh\left(2\frac{\sqrt{2|C|}}{d}y\right) + (d+2\rho_0)\cosh\left(2\frac{\sqrt{2|C|}}{d}y\right) > d > 0. \tag{7.11}$$

Using the hyperbolic function definitions, the following identity is in general verified $a\cosh(x) + b\sinh(x) = \frac{1}{2}\left[(a+b)\,e^{x} + (a-b)\,e^{-x}\right]$. As in our case, when $a, b \in \mathbb{R}^+$ the function is convex. This implies that the optimal profile lies under the stationary one in the spatial range $[0,1]$ since it has to match boundary conditions (see magenta and orange curves in Figure 7.1). Lastly, for $C > 0$ the current conditioning range is $j \in \left(-\infty, -J^0\right) \cup \left(J^0, \infty\right)$ and for the optimal profile we have

$$\bar{\rho}_j^{+}(y) := \frac{1}{2}\left\{\sqrt{\frac{2}{|C|}\left[j^2 - 2|C|\,\chi(\rho_0)\right]}\sin\left(2\frac{\sqrt{2|C|}}{d}y\right)\right. \tag{7.12}$$

$$\left. + (d+2\rho_0)\cos\left(2\frac{\sqrt{2|C|}}{d}y\right) - d\right\}, \tag{7.13}$$

The positivity condition for the square root of the sin coefficient is automatically verified when $C > 0$ from (7.8), that is $j^2 - 4|C|\,\chi(\bar{\rho}_j) = \left(D(\bar{\rho}_j)\right)^2\left(\frac{d\bar{\rho}_j}{dy}\right)^2 \geqslant 0$. It is known that for functions of the form $a\cos(x) + b\sin(x)$ with $a, b \in \mathbb{R}^+$, the inflection points coincide with the roots. In this way, the sign of the second derivative and of the function are opposite. Since $\bar{\rho}_j^{+}(0) = \rho_0$ and the sign is fixed, we can conclude that the optimal density profile is concave (see blue and red curves in Figure 7.1). To determine the cost function we need to substitute the optimal profile in (4.90). It reduces to

$$\frac{I_L(j)}{L} = 2\int_0^1 A\left(\bar{\rho}_j(y)\right)dy - C + \frac{j}{2}\ln\left(\frac{\rho_1(d+\rho_0)}{\rho_0(d+\rho_1)}\right), \tag{7.14}$$

where the first integral gives rise to an explicit lengthy expression using (4.84) which we do not report. The curve of the cost function is plotted in Figure 7.2. Again, we can determine the SCGF for $\lambda(k)$ via the Legendre-Fenchel transform (4.4) as to have a direct comparison with the data obtained from the cloning algorithm simulation. The results are reported in Figure 7.3. Here, the symmetry of the curve is a consequence of the fluctuation relation [48] which is expressed at the level of the SCGF as

$$\lambda\left(I_L'(0) + k\right) = \lambda\left(I_L'(0) - k\right), \tag{7.15}$$

which can be obtained from (4.83) via the Legendre-Fenchel transform.

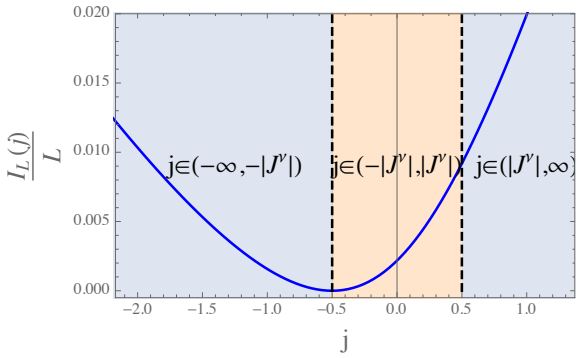

Figure 7.2: Rescaled current large deviation function (7.14) of the IP for $p = q = \frac{1}{2}$, $d = 1$, $\rho_1 = 1.5$ and $\rho_0 = 0.5$. The stationary current corresponds to $-\left|J^0\right| = -\frac{d}{2}(\rho_1 - \rho_0) = -0.5$. We notice that the curve is not symmetric around the minimum since current conditioning flowing in the same direction of the J^0 are more favorable. The light orange area corresponds to convex density profiles, while the remaining light blue refers to concave $\bar{\rho}_j(y)$.

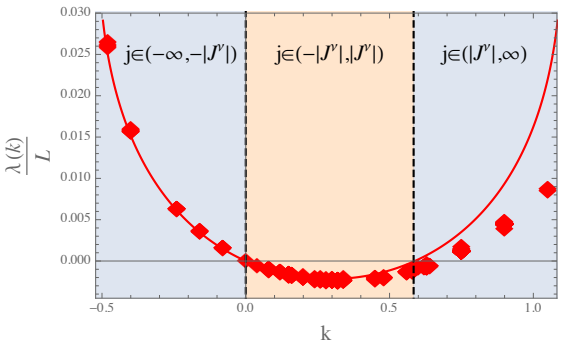

Figure 7.3: SCGF of the IP for $p = q = \frac{1}{2}$, $d = 1$, $\rho_1 = 1.5$ and $\rho_0 = 0.5$. The light orange region corresponds to the light orange shaded area in the cost function in Figure 7.2 and they are related through the Legendre-Fenchel transform. The same holds for the light blue areas. The point $(0, 0)$ corresponds to the stationary current $-\left|J^0\right| = -\frac{d}{2}(\rho_1 - \rho_0)$. The curve is symmetric around the point $k = I'(0)$, as follows from the fluctuation relation for the SCGF (7.15). Red diamond data points are obtained from two instances of the cloning algorithm both having 2^{15} clones, $L = 32$ system size but running time L^2 and $5L^2$. The discrepancy between the data points and the theoretical curve on the right hand side of the plot is due to finite simulation running time, corresponding to positive currents which are more costly since the system needs to reverse current direction (see also Figure 7.2). Longer running times correspond to points closer to the theoretical curve.

In the Figure 7.3, the point $(0.584, 0)$ (which for (7.15) is symmetric to the origin) corresponds to condition the current to the value $j = \frac{d}{2}(\rho_1 - \rho_0)$ which has

the opposite to the stationary current. Up to now, we have considered the case $\rho_1 > \rho_0$ but the same analysis can be performed for identical boundary reservoirs. From (7.6), we see that for $\rho_1 = \rho_0$ the stationary current is equal to $J^0 = 0$. This implies that the light orange area in Figure 7.2 and 7.3 vanishes, leading to concave only profiles (see top Figure in 7.4). In this case, the cost function and its SCGF are symmetric w.r.t. the origin as expected, since we can swap the reservoir densities without any noticeable change (see bottom Figures in 7.4).

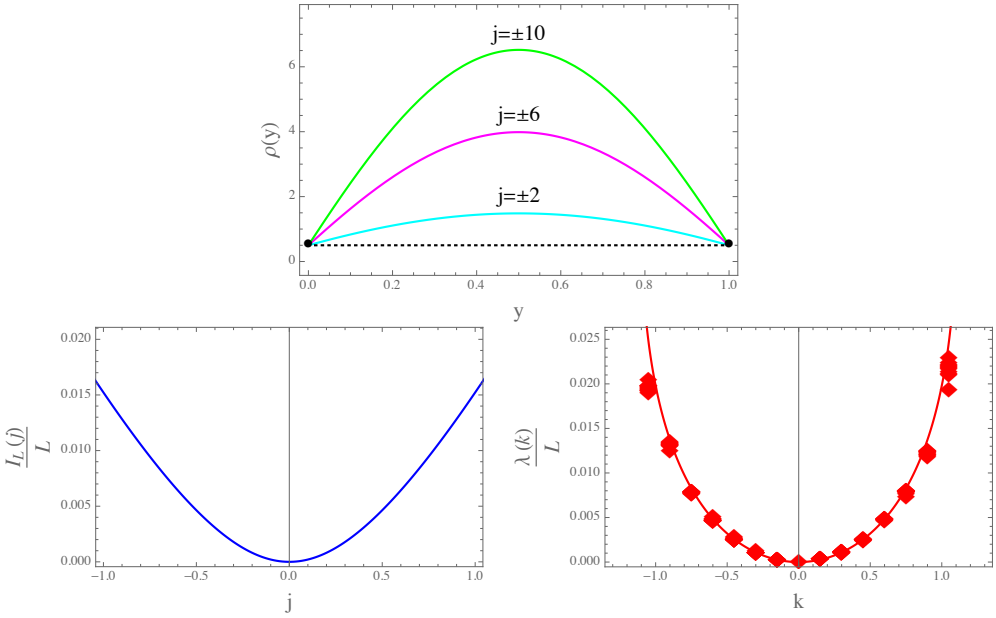

Figure 7.4: (Top) Optimal and stationary density profiles of the IP for $p = q = \frac{1}{2}$, $d = 1$, $\rho_1 = \rho_0 = 0.5$. The black dots highlight the boundary density values which now have the same height. The black dotted line is the stationary profile as in (7.6) which corresponds to the stationary current $J^0 = 0$. As explained in the main text, current conditioning for $j \neq 0$ give rise to concave profile only. (Bottom Left) Cost function of the IP for $p = q = \frac{1}{2}$, $d = 1$, $\rho_1 = \rho_0 = 0.5$. The stationary current corresponds to $J^0 = 0$. In this case, the cost to condition on a current of value j or $-j$ is the same. (Bottom Right) SCGF of the IP for $p = q = \frac{1}{2}$, $d = 1$, $\rho_1 = \rho_0 = 0.5$. The system size used for the cloning simulation is $L = 32$ with running time L^2 and 2^{15} clones. For each value of k used for the simulation, we report the output at different increasing times. As before, the simulation points at the extreme sides of the figure underestimate the theoretical curve since they correspond to more costly current conditionings. Increasing simulation total running time reduces the discrepancy between the data and the SCGF.

7.2 Quantum Algebraic Method

From the MFT, we were able to obtain stationary optimal density profiles to generate current deviations using a macroscopic description relying on a constitutive equation. In this section instead, we will focus on the activity (3.62) and, using a microscopic descritpion, we will apply an algebraic method to determine the leading eigenvalue of the SCGF for this observable. This techinque was used to calculate current fluctuations for the ZRP in [47] and then expanded in [51]. Here, we will study symmetric inclusion process in contact with particle reservoirs extending previous results in [84]. Due to the non-zero range interaction in the IP dynamics, this approach cannot be used to study current large deviations for the IP. In particular, we will focus on the boundary sites activity as will be explained later.

7.2.1 Activity Fluctuations

For the IP with open boundaries, whose generator is

$$\hat{M}_{OB}^{N} = p\left(\hat{c}_1\hat{\alpha}_1^r - \hat{\alpha}_1^r\right) + p\sum_{x=1}^{L-1}\left[\hat{c}_{x+1}\hat{a}_x\left(\hat{u}_x\hat{v}_{x+1}\right) - \hat{u}_x\hat{v}_{x+1}\right] + p\left(\hat{a}_L\hat{\beta}_L^r - \hat{\beta}_L^r\right) \tag{7.16}$$

$$+ q\left(\hat{a}_1\hat{\beta}_1^l - \hat{\beta}_1^l\right) + q\sum_{x=1}^{L-1}\left[\hat{c}_x\hat{a}_{x+1}\left(\hat{u}_{x+1}\hat{v}_x\right) - \hat{u}_{x+1}\hat{v}_x\right] + q\left(\hat{c}_L\hat{\alpha}_L^l - \hat{\alpha}_L^l\right), \tag{7.17}$$

we have seen that a stationary product measure is obtained with flat fugacity profile if the relations (3.37) are satisfied. To realize fluctuations in certain observables, the general idea is to use factorised states with non-trivial density or fugacity profiles as candidates. Here, we allow the fugacity to assume a different value ψ in the bulk of the system as expressed by the vector $(\phi, \psi, \ldots, \psi, \phi)$ with $\phi = \frac{\rho}{\rho+d}$, in contrast to more general spatial dependence for the ZRP [47, 51]. This choice of the fugacity vector is motivated *a posteriori* since it allows the simultaneous cancellation of all the prefactors of the bulk operators in (7.23). The relations (3.42) change into

$$\hat{c}_x\hat{v}_x\left|\mathbb{P}_\psi^*\right\rangle = \psi^{-1}\hat{u}_x\left|\mathbb{P}_\psi^*\right\rangle \ \forall x \in \Lambda, \tag{7.18}$$

$$\hat{a}_x\hat{u}_x\left|\mathbb{P}_\psi^*\right\rangle = \psi\hat{v}_x\left|\mathbb{P}_\psi^*\right\rangle \ \forall x \in \Lambda, \tag{7.19}$$

and the same for (3.44)

$$\hat{c}_x\hat{\alpha}_x \left|\mathbb{P}^*_\psi\right\rangle = \psi^{-1} \langle u\rangle_* \hat{u}_x \left|\mathbb{P}^*_\psi\right\rangle \;\; x \in \{1, L\}\,, \tag{7.20}$$

$$\hat{a}_x\hat{\beta}_x \left|\mathbb{P}^*_\psi\right\rangle = \quad \psi \langle v\rangle_* \hat{v}_x \left|\mathbb{P}^*_\psi\right\rangle \;\; x \in \{1, L\}\,, \tag{7.21}$$

where $\left|\mathbb{P}^*_\psi\right\rangle$ has ψ in place of ϕ in $|\mathbb{P}^*\rangle$. Moreover, we can repeat the same steps as in Section 4.2.2 (where we use positive current operators everywhere since we are considering activity only) and we obtain

$$\begin{aligned}\tilde{M}^{N,J}_{OB}(k) = p\left(e^{\frac{k}{L}}\hat{c}_1\hat{\alpha}^r_1 - \hat{\alpha}^r_1\right) + p\sum_{x=1}^{L-1}\left[\hat{c}_{x+1}\hat{a}_x\left(\hat{u}_x\hat{v}_{x+1}\right) - \hat{u}_x\hat{v}_{x+1}\right] + p\left(e^{\frac{k}{L}}\hat{a}_L\hat{\beta}^r_L - \hat{\beta}^r_L\right)\\ + q\left(e^{\frac{k}{L}}\hat{a}_1\hat{\beta}^l_1 - \hat{\beta}^l_1\right) + q\sum_{x=1}^{L-1}\left[\hat{c}_x\hat{a}_{x+1}\left(\hat{u}_{x+1}\hat{v}_x\right) - \hat{u}_{x+1}\hat{v}_x\right] + q\left(e^{\frac{k}{L}}\hat{c}_L\hat{\alpha}^l_L - \hat{\alpha}^l_L\right).\end{aligned} \tag{7.22}$$

Applying the modified $\left|\mathbb{P}^*_\psi\right\rangle$, reduces the generator to

$$\begin{aligned}\tilde{M}^{N,J}_{OB}(k)\left|\mathbb{P}^*_\psi\right\rangle = \Bigg\{ &\langle u\rangle_\phi \hat{u}_1\left[\left(qe^{\frac{k}{L}}C\phi^{-1}\right)\psi + \left(pe^{\frac{k}{L}}\right)\psi^{-1}\right.\\ &\left. + (q-p)\frac{v(0)}{\langle u\rangle_\phi} - \left(q\phi^{-1} + Cp\right)\right]\\ &+ \langle u\rangle_\phi \hat{u}_L\left[\left(pe^{\frac{k}{L}}C\phi^{-1}\right)\psi + \left(qe^{\frac{k}{L}}\right)\psi^{-1}\right.\\ &\left. + (p-q)\frac{v(0)}{\langle u\rangle_\phi} - \left(p\phi^{-1} + Cq\right)\right]\\ &+ \langle u\rangle_\phi v(0)\left[\psi\left(pe^{\frac{k}{L}}\phi^{-1} + qe^{\frac{k}{L}}\phi^{-1}\right) - (q+p)\right]\Bigg\}\left|\mathbb{P}^*_\psi\right\rangle\end{aligned} \tag{7.23}$$

where C is a parameter in the arrival jump rates (3.31) which is fixed for a given model. As we are focusing on the symmetric case, fixing $p = q = \frac{1}{2}$ allows us to find a value for the bulk fugacity ψ which cancels the terms $\hat{u}_1$ and $\hat{u}_L$ at the same time. It is given by

$$\psi_{+;-}(k) = \frac{\left(\phi^{-1} + C\right) \pm \sqrt{\left(\phi^{-1} + C\right)^2 - 4e^{\frac{2k}{L}}C\phi^{-1}}}{2\left(e^{\frac{k}{L}}C\phi^{-1}\right)}. \tag{7.24}$$

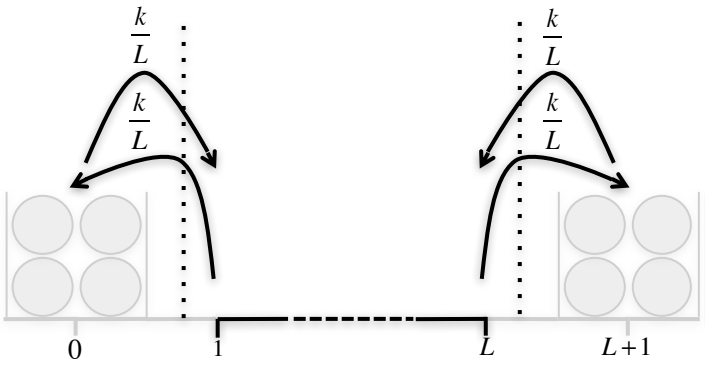

Figure 7.5: Graphic representation of the activity tilting for the IP.

In this way, we have reduced the preceding expression to $\tilde{M}_{OB}^{N,J}(k)\left|\mathbb{P}_{\psi}^{*}\right\rangle = e_{+;-}^{L}(k)\left|\mathbb{P}_{\psi}^{*}\right\rangle$ where we have called the eigenvalue

$$e_{+;-}^{L}(k) \coloneqq \langle u\rangle_{\phi} v(0)\left(\psi_{+;-}\phi^{-1}e^{\frac{k}{L}}-1\right). \tag{7.25}$$

The independence of the eigenvalue from the sites where the counting operator is located can be proved via a similarity transformation (see Equation 17 in [51]). To give meaning to the procedure we just outlined, we need to make the ansatz, like in [47, p. 7], that $\left|\mathbb{P}_{\psi}^{*}\right\rangle$ is the actual stationary probability vector of product form associated to the dominant eigenvalue (7.25), which results from the spectral decomposition of $\tilde{M}_{OB}^{N,J}(k)$. This ansatz allows us to select a solution from (7.24). In fact, we can verify that $\psi_{-}(0)=\phi$ as one would expect since $\tilde{M}_{OB}^{N,J}(0)=\hat{M}_{OB}^{N}$, so the resulting eigenvalue is given by $e_{-}^{L}(k)$.

7.2.2 Consistency Checks

To verify the consistency of the arguments developed in the preceding sections we have carried out two checks. First, we have run a cloning algorithm simulation conditioning only on the activity across the two boundaries, in agreement with the master equation operator (7.22). The results are shown in Figure 7.6. As a second test, we verify that the eigenvalue obtained for $C\to 0$ is the same as the one obtained from a suitably modified ZRP with open boundaries in [47]. To calculate the limit

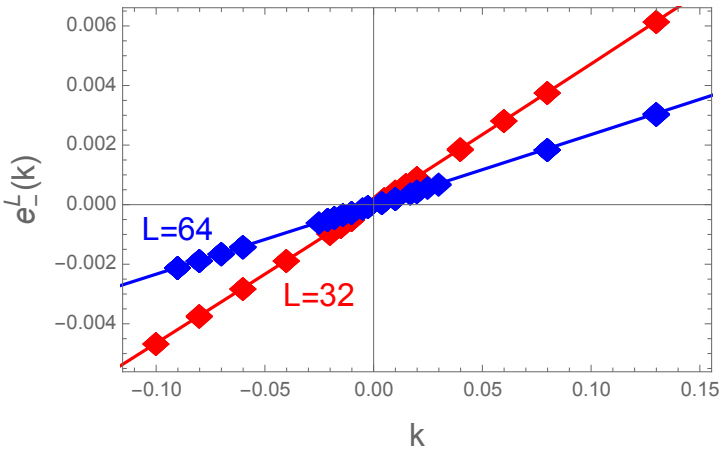

Figure 7.6: Red and blue curves are given from (7.25) for $L = 32$ and $L = 64$, respectively, with $\rho = 1$, $d = 1$ and $C = 1$ for the symmetric IP with rates $u(\eta_x) = \eta_x$ and $v(\eta_x) = \eta_x + d$. Corresponding data points match well and are obtained from a cloning algorithm simulation with 2^{15} clones and running time L^2.

$C \to 0$, we can apply the L'Hopital's rule to the ψ_- case. Thus it follows

$$\lim_{C\to 0} \frac{1 - \frac{1}{2}\left[\left(C+\phi^{-1}\right)^2 - 4\left(e^{\frac{2k}{L}} C\phi^{-1}\right)\right]^{-\frac{1}{2}} \left[2\left(C+\phi^{-1}\right) - 4\left(e^{\frac{2k}{L}}\phi^{-1}\right)\right]}{2\left(e^{\frac{k}{L}}\phi^{-1}\right)} = e^{\frac{k}{L}}\phi, \tag{7.26}$$

and the corresponding eigenvalue is

$$e_-^L(k) = \langle u \rangle_\phi \, v(0)\left[e^{\frac{2k}{L}} - 1\right] \quad \text{with } C \to 0 \ , \tag{7.27}$$

where $\langle u \rangle_\phi$ is given in (3.35). The ZRP with open boundaries as used in [47] is represented in the Figure 7.7.

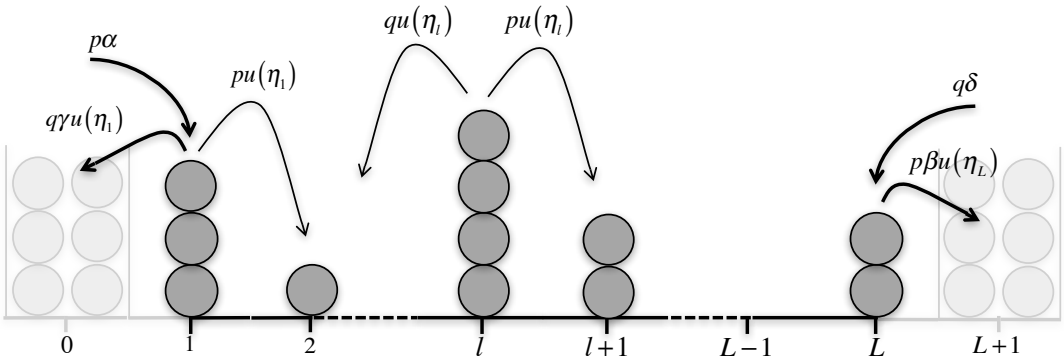

Figure 7.7: Graphic representation of the ZRP with open boundaries using the notation in [47].

Starting from equations (18) and (22) in [47], the master equation operator for the above model applied to the eigenvector $|0\rangle$ related to the principal eigenvalue is given by

$$\begin{aligned}\tilde{M}_{OB}^{N,J}(k)|0\rangle = \Bigg[&\sum_{l=1}^{L-1}\left(p\phi_x - q\phi_{x+1}\right)\left(\phi_{x+1}^{-1}\hat{u}_{x+1} - \phi_x^{-1}\hat{u}_x\right)\\ &+ p\alpha\left(e^{\frac{k}{L}}\phi_1^{-1}\hat{u}_1 - 1\right) + q\gamma\left(e^{\frac{k}{L}}\phi_1 - d_1\right)\\ &+q\delta\left(e^{\frac{k}{L}}\phi_L^{-1}\hat{u}_L - 1\right) + p\beta\left(e^{\frac{k}{L}}\phi_L - \hat{u}_L\right)\Bigg]|0\rangle\,, \end{aligned} \tag{7.28}$$

where $\alpha, \beta, \gamma, \delta$ are the reservoirs jump rates parameters as explained in the Figure 7.7. We notice that the stationary probability distribution for the ZRP with OB admits free choice of the parameters taking into account the presence of the reservoirs [47]. In order to compare the results of the ZRP to ours of the IP, we cast the ZRP under the conditions used for the IP, that is $p = q$ and $z_l = z\ \forall l \in \Lambda$. In this way, the bulk contribution in (7.28) vanishes and the boundary terms are equal to

$$p\left[\left(\alpha e^{\frac{k}{L}}\phi^{-1} - \gamma\right)\hat{u}_1 + \left(\delta e^{\frac{k}{L}}\phi^{-1} - \beta\right)\hat{u}_L + \left(-\alpha + \gamma e^{\frac{k}{L}}\phi - \delta + \beta e^{\frac{k}{L}}\phi\right)\right]. \tag{7.29}$$

To cancel the contribution from the operators $\hat{u}_x$, we need to find a condition which fixes the coefficients in front of the ds to 0 at the same time. This can be achieved by imposing

$$\begin{aligned}\left(\alpha e^{\frac{k}{L}}\phi^{-1} - \gamma\right) = 0 \Rightarrow \phi = \frac{\alpha}{\gamma}e^{\frac{k}{L}}\\ \left(\delta e^{\frac{k}{L}}\phi^{-1} - \beta\right) = 0 \Rightarrow \phi = \frac{\delta}{\beta}e^{\frac{k}{L}}\end{aligned} \tag{7.30}$$

hence we are guided to assume $T \coloneqq \frac{\alpha}{\gamma} = \frac{\delta}{\beta}$. Now, starting from the most general case for the eigenvalue

$$e_0 = p\left(-\alpha + \gamma e^{\frac{k}{L}}\phi - \delta + \beta e^{\frac{k}{L}}\phi\right) \tag{7.31}$$

and using $\gamma = \alpha T^{-1}$ together with $\beta = \delta T^{-1}$ we obtain

$$e_0 = p\left(-\alpha + \gamma e^{\frac{k}{L}}\phi - \delta + \beta e^{\frac{k}{L}}\phi\right) = p\left(\alpha\left(e^{2\frac{k}{L}} - 1\right) + \delta\left(e^{2\frac{k}{L}} - 1\right)\right) \tag{7.32}$$

where if we take $\alpha = \delta = \langle u\rangle_\phi\, v(0)$ and $p = \frac{1}{2}$ we have the same result (7.27) we had for the IP.

CHAPTER 8

Conclusions

In this chapter we will provide a summary of the results described in the thesis and we will provide some outlooks about possible research paths the present work can lead to.

Chapter 2 was dedicated to introducing the quantum notation in the context of HCTMC. The quantum notation turns out to be a suitable framework for stochastic processes due to the analogy between the Schrödinger and the Master equation which puts in relation the quantum Hamiltonian and the generator. In this way, many of the techniques developed for Many-Body quantum systems can be adapted to stochastic processes, like the Bethe Ansatz or the Density-Matrix Renormalization Group see [69, p. 61]. In Chapter 3, we exploited the quantum notation to outline the framework used to define SPS. In this way, we introduced the main observables together with the models of interest for the present thesis, which are the ZRP and the IP. In particular, for both models, we have focused on nearest-neighbour interactions on one-dimensional lattices with periodic as well as open boundary conditions, that is in contact with particle reservoirs. In both situations, the two models present stationary site-factorizable product measures in explicit forms which we proved using the quantum notation by showing diagonalization properties for creation and annihilation operators. With these ingredients, we defined the NESS which are the starting point of our analysis. In fact, the question we inquired is about the behaviour of large fluctuations from the typical stationary values of the main non-equilibrium observables in the NESS. So, in Chapter 4, we reviewed the main approaches to determine fluctuations for the models of interest stemming from LDT (which was briefly summarized at the beginning of the chapter). From the microscopic perspective, we reviewed the logical steps to determine an effective dynamics generating the large deviation event starting from the definition of the SCGF, which is the main quantity of interest for LDT together with the rate function. This can be achieved by selecting a suitable time window and

transforming the generator of the original process via Doob's method. Next, we considered, by giving heuristic arguments, the hydrodynamic limit of SPS. Depending on the scaling of the spatial asymmetry of the model, there exist qualitative different behaviour for the resulting continuity equation. In fact, for total or partial asymmetry, the models essentially behave like hyperbolic conservation laws. For symmetric or weakly-asymmetric systems, the resulting dynamics is parabolic or heat-equation like. In terms of LDT, these two kinds of continuos behaviour lead to different rate functions. Current fluctuations for total and partially asymmetric dynamics can be explored within the JV approach, while symmetric and weakly-asymmetric systems can be studied within the general framework of MFT.

In Chapter 5, we study lower current large deviations for general TAZRP with concave flux functions $J(\rho)$, which can be realized by phase separated density profiles. Travelling wave profiles related to non-entropic hydrodynamic shocks are identified as the universal typical realization at least for small deviations from the typical current. These shocks can be stabilized by local changes in the dynamics and lead to rate functions which are independent of the system size, which have been studied before for the exclusion process. The range of accessible currents for these profiles may be limited, and we established a dynamical phase transition where large deviations for low currents are realized by condensed profiles. In this case the rate function is determined by slowing down the exit process out of the condensate which is again independent of the system size in the case of bounded rates. The transition is caused by two basic mechanisms (summarized in Figure 5.3); firstly, the range of densities in travelling wave profiles is bounded by the critical density in condensing ZRPs, this leads to a minimal accessibe current of $j_{min} = \rho/\rho_c$. Secondly, the ratio of limiting current and density appearing in (5.15) may be bounded due to an asymptotically linear current density relation. In this case the rate function for condensed states is extensive in the system size. We have studied these cases in detail for typical examples of jump rates, together with other generic models with bounded and unbounded rates which do not exhibit a dynamic transition. In this way we cover all qualitative cases of concave flux functions which gives a complete picture of the large deviations for lower current deviations formulated in (5.5) and (5.6) in the limit of diverging system size. For condensing systems large deviations of the current may be realized by a temporal mixture leading to a rate function which is not strictly convex everywhere, which we have confirmed by numerical simulations using a cloning algorithm in Section 5.1.3.4. For finite systems, other strategies beyond travelling waves or condensed profiles may play a role as is illustrated for asymptotically linear rates in Section 5.1.3.3. It turns out, tha the JV analysis

can be used also for convex current-density relations as in the case of the TAIP. In this case, only upper current deviations are covered by this approach. For lower current deviations, it turns out that a combination of alternating density profiles and a general slowing down of the dynamics provide the most efficient strategies. Condensed profiles are more costly and do not play a role for IP.

In Chapter 6, we adapted the JV framework for the case of partial asymmetry. It turns out that the analysis and conclusions obtained for the current regimes of the totally asymmetric case, for both the ZRP and IP, are left unchanged apart for a rescaling factor which takes into account the partial asymmetry. However, in this case, it is possible to reach atypical currents beyond the ranges analyzed in Chapter 5. By conditioning on the spatial part of the jump rates, it is possible to obtain negative atypical currents which correspond to the particles flowing in the direction opposite to the stationary current. Negative current conditioning for the PAZRP can also be obtained as a combination of spatial and activity biasing. In fact, this give rise to a new optimal cost function. Currents beyond the JV range are obtained with flat profiles and the associated cost functions are linear in the system size. In combination with size-independent cost in the JV regime, the cost per site give rise to a convex hull, which is the signature of a dynamical phase transition. As before, the SCGF associated to the convex hull cost function is compared with numerical simulation performed using the cloning algorithm.

In Chapter 7, mirroring previous results for the ZRP in [47, 51], we studied macroscopic current fluctuations for the symmetric IP with open boundaries. Using the contraction principle, we reduced the general current and density MFT cost function to an optimization problem over the density profile functional which, for simplicity, is assumed to be stationary in time. The particle reservoirs are taken into account by imposing fixed boundary density values in the same fashion as explained in Chapter 2 in the context of the stationary product measure. It turns out that when the two density values are identical, current fluctuations for the IP are realized through concave symmetric density profiles only which have their maximum in the middle of the lattice. For different boundary density values, concave as well as convex profiles are admitted. The former case is realized for currents which are in modulo less than the stationary value, while the latter for every other current conditioning. The second part of the chapter analyse fluctuations of the activity using a microscopic method exploiting the quantum notation which allows us to determine the dominant eigenvalue for large times. It turns out that activity fluctuations are realized through a constant bulk fugacity profile which is a function of the reservoir fugacities. The results obtained are corroborated by cloning algorithm simulations

as well as by adapting previous results of the ZRP.

All the results presented in the thesis are based on heuristic arguments which are supported by numerical simulations. For future works it would be desirable to complement our JV analysis with exact results derived from a microscopic approach, analogously to results for open boundary systems [51], and to investigate how the dynamic transition can be understood in the framework of macroscopic fluctuation theory. There has been recent evidence [60, 51] that this framework (possibly taking appropriate limits) can also be used for partially or totally asymmetric dynamics. Moreover, it is interesting to study the space-time structure of the dynamical transitions presented in the thesis at the critical regime in which the convex hull does not coincide with the cost functions from which it is orginated. In addition, the microscopic analysis for activity fluctuations for the IP could be extended to current fluctuations by writing the diagonalization properties for creation and annihilation operators in terms of densities. However, this type of analysis for ZRP made particular use of the existence of non-homogeneous factorized stationary states which do not exist for IP, so this is likely to be a significant challenge. In this way, we could be able to recover the macroscopic density profile obtained from the eigenvalue structure of the large deviation underlying dynamics which could give us information about how to reconcile the JV and MFT approaches.

APPENDIX A

Quantum Operators in the Stationary State

This appendix is dedicated to collect the proofs of the properties of quantum operators, introduced in Section 3.2.3, related to particle creation and annihilation in the stationary state. We will also show some properties of counting operators discussed in Section 4.2.2. In the end, using the quantum notation, we will show that the probability distribution defined in (3.29) is stationary.

Lemma A.0.1. *Let $\langle\,\rangle_*$ be the expectation w.r.t. the stationary product measure as defined in (3.34) and u, v as given in (3.5). Then, the following identity holds*

$$\langle v\rangle_* = \frac{1}{\phi}\langle u\rangle_*\,.$$

Proof.

$$\begin{aligned}
\langle v\rangle_* &= \frac{1}{z(\phi)}\sum_{n=0}^{\infty} v(n)\,\omega(n)\,\phi^n = \frac{1}{z(\phi)}\sum_{n=0}^{\infty}\phi^n v(n)\prod_{k=1}^{n}\frac{v(k-1)}{u(k)}\\
&= \frac{1}{\phi}\frac{1}{z(\phi)}\sum_{n=0}^{\infty}\phi^{n+1}u(n+1)\,\frac{v(n)}{u(n+1)}\prod_{k=1}^{n}\frac{v(k-1)}{u(k)}\\
&= \frac{1}{\phi}\frac{1}{z(\phi)}\sum_{n=0}^{\infty}\phi^{n+1}u(n+1)\,\omega(n+1)\\
&= \frac{1}{\phi}\langle u\rangle_*
\end{aligned}$$

since $u(0)=0$ by definition. □

Lemma A.0.2. *Let $|\mathbb{P}^*\rangle$ be the probability vector as defined in (3.32), and $\hat{c}_x$, $\hat{v}_x$ operators given in (3.24) and (3.23), respectively. Then, the following identity holds*

$$\hat{c}_x \hat{v}_x |\mathbb{P}^*\rangle = \phi^{-1} \hat{u}_x |\mathbb{P}^*\rangle$$

Proof.

$$\begin{aligned}
\hat{c}_x \hat{v}_x |\mathbb{P}^*\rangle &= \sum_{\eta} \mathbb{P}^*_{\eta} \hat{c}_x \hat{v}_x |\eta\rangle \\
&= \sum_{\eta} P^*_{\eta} v(\eta_x) |\eta^{+x}\rangle = \sum_{\eta} \left[\prod_{y \in \Lambda} \left(\frac{1}{z(\phi)} w(\eta_y) \phi^{\eta_y} \right) \right] v(\eta_x) |\eta^{+x}\rangle \\
&= \sum_{\eta} \left[\frac{w(\eta_x) \phi^{\eta_x}}{z(\phi)} \prod_{y \in \Lambda - \{x\}} \frac{1}{z(\phi)} w(\eta_y) \phi^{\eta_y} \right] v(\eta_x) |\eta^{+x}\rangle
\end{aligned}$$

$$\begin{aligned}
w(\eta_x) \phi^{\eta_x} &= \phi^{\eta_x} \prod_{k=1}^{\eta_x} \frac{v(k-1)}{u(k)} = \phi^{\eta_x} \left[\frac{\phi}{\phi} \right] \prod_{k=1}^{\eta_x} \frac{v(k-1)}{u(k)} \left[\frac{v(\eta_x)}{u(\eta_x+1)} \frac{u(\eta_x+1)}{v(\eta_x)} \right] \\
&= \left(\frac{1}{\phi} \frac{u(\eta_x+1)}{v(\eta_x)} \right) \phi^{\eta_x+1} \prod_{k=1}^{\eta_x+1} \frac{v(k-1)}{u(k)} = \left(\frac{1}{\phi} \frac{u(\eta_x+1)}{v(\eta_x)} \right) \phi^{\eta_x+1} w(\eta_x+1)
\end{aligned}$$

$$\begin{aligned}
\hat{c}_x \hat{v}_x |\mathbb{P}^*\rangle &= \phi^{-1} \sum_{\eta} \left[\left(\frac{u(\eta_x+1)}{v(\eta_x)} \right) \frac{\phi^{\eta_x+1} w(\eta_x+1)}{z(\phi)} \prod_{y \in \Lambda - \{x\}} \frac{1}{z(\phi_y)} w(\eta_y) \phi^{\eta_y} \right] v(\eta_x) |\eta^{+x}\rangle \\
&= \phi^{-1} \sum_{\eta} u(\eta_x+1) \mathbb{P}^*_{\eta^{+x}} |\eta^{+x}\rangle = \phi^{-1} \hat{u}_x |\mathbb{P}^*\rangle
\end{aligned}$$

□

Lemma A.0.3. *Let $|\mathbb{P}^*\rangle$ be the probability vector as defined in (3.32), and $\hat{a}_x$, $\hat{u}_x$ operators given in (3.24) and (3.23), respectively. Then, the following identity holds*

$$\hat{a}_x\hat{u}_x\left|\mathbb{P}^*\right\rangle = \phi\hat{v}_x\left|\mathbb{P}^*\right\rangle$$

Proof.

$$\begin{aligned}\hat{a}_x\hat{u}_x\left|\mathbb{P}^*\right\rangle &= \sum_{\eta}\mathbb{P}^*_{\eta}\hat{a}_x\hat{u}_x\left|\eta\right\rangle \\ &= \sum_{\eta}P^*_{\eta}u\left(\eta_x\right)\left|\eta^{-x}\right\rangle \\ &= \sum_{\eta}\left[\frac{w\left(\eta_x\right)\phi^{\eta_x}}{z\left(\phi\right)}\prod_{y\in\Lambda-\{x\}}\frac{1}{z\left(\psi_y\right)}w\left(\eta_y\right)\phi^{\eta_y}\right]u\left(\eta_x\right)\left|\eta^{-x}\right\rangle\end{aligned}$$

$$\begin{aligned}w\left(\eta_x\right)\phi^{\eta_x} =&\phi^{\eta_x}\prod_{k=1}^{\eta_x}\frac{v\left(k-1\right)}{u\left(k\right)} = \phi^{\eta_x}\left[\frac{\phi}{\phi}\right]\frac{v\left(\eta_x-1\right)}{u\left(\eta_x\right)}\prod_{k=1}^{\eta_x-1}\frac{v\left(k-1\right)}{u\left(k\right)} \\ =&\left(\phi\frac{v\left(\eta_x-1\right)}{u\left(\eta_x\right)}\right)\phi^{\eta_x-1}\prod_{k=1}^{\eta_x-1}\frac{v\left(k-1\right)}{u\left(k\right)} = \left(\phi\frac{v\left(\eta_x-1\right)}{u\left(\eta_x\right)}\right)\phi^{\eta_x-1}w\left(\eta_x-1\right)\end{aligned}$$

$$\begin{aligned}\hat{a}_x^r\hat{u}_x\left|\mathbb{P}^*\right\rangle =&\phi\sum_{\eta}\left[\left(\frac{v\left(\eta_x-1\right)}{u\left(\eta_x\right)}\right)\frac{\phi^{\eta_x-1}w\left(\eta_x-1\right)}{z\left(\phi\right)}\prod_{y\in\Lambda-\{x\}}\frac{1}{z_y\left(\phi\right)}w\left(\eta_y\right)\phi^{\eta_y}\right]u\left(\eta_x\right)\left|\eta^{-x}\right\rangle \\ =&\phi\sum_{\eta}v\left(\eta_x-1\right)\mathbb{P}^*_{\eta^{-x}}\left|\eta^{-x}\right\rangle = \phi\hat{v}_x\left|\mathbb{P}^*\right\rangle\end{aligned}$$

□

Lemma A.0.4. *Let $\hat{j}_x$ and $\hat{J}_x$ be current operators as defined in (4.35) acting on the counting space $|\theta\rangle$, see (4.34). Then, the following identity holds*

$$e^{-\frac{k}{L}\hat{J}_x}\hat{j}_x^{\pm}e^{\frac{k}{L}\hat{J}_x} = e^{\mp\frac{k}{L}}\hat{j}_x^{\pm}$$

Proof.

$$\begin{aligned}e^{-\frac{k}{L}\hat{J}_x}\hat{j}_x^{\pm}e^{\frac{k}{L}\hat{J}_x}\left|\theta\right\rangle =&e^{-\frac{k}{L}\hat{J}_x}\hat{j}_x^{\pm}e^{\frac{k}{L}\theta_x}\left|\theta\right\rangle = e^{\frac{k}{L}\theta_x}e^{-\frac{k}{L}\hat{J}_x}\hat{j}_x^{\pm}\left|\theta\right\rangle \\ =&e^{\frac{k}{L}\theta_x}e^{-\frac{k}{L}\hat{J}_x}\left|\theta^{\pm x}\right\rangle = e^{\frac{k}{L}\theta_x}e^{-\frac{k}{L}(\theta_x\pm1)}\left|\theta^{\pm x}\right\rangle = e^{\mp\frac{k}{L}}\left|\theta^{\pm x}\right\rangle = e^{\mp\frac{k}{L}}\hat{j}_x^{\pm}\left|\theta\right\rangle\end{aligned}$$

□

Lemma A.0.5. *Let $\hat{j}_x$ and $\hat{J}_x$ be current operators as defined in (4.35) acting on the counting space $|\theta\rangle$, see (4.34). Then, the following identity holds*

$$\left[\hat{j}_x^{\pm}, \hat{J}_x\right] = \mp \hat{j}_x^{\pm}$$

Proof.

$$\begin{aligned}\left[\hat{j}_x^{\pm}, \hat{J}_x\right]|\theta\rangle &= \left(\hat{j}_x^{\pm}\hat{J}_x - \hat{J}_x\hat{j}_x^{\pm}\right)|\theta\rangle = \hat{j}_x^{\pm}\hat{J}_x|\theta\rangle - \hat{J}_x\hat{j}_x^{\pm}|\theta\rangle = \hat{j}_x^{\pm}\hat{J}_x|\theta\rangle - \hat{J}_x\left|\theta^{\pm x}\right\rangle \\ &= \theta_x\hat{j}_x^{\pm}|\theta\rangle - \hat{J}_x\left|\theta^{\pm x}\right\rangle = \theta_x\hat{j}_x^{\pm}|\theta\rangle - (\theta_x \pm 1)\left|\theta^{\pm x}\right\rangle \\ &= \theta_x\hat{j}_x^{\pm}|\theta\rangle - (\theta_x \pm 1)\,\hat{j}_x^{\pm}|\theta\rangle = (\theta_x - \theta_x \mp 1)\,\hat{j}_x^{\pm}|\theta\rangle \\ &= \mp\,\hat{j}_x^{\pm}|\theta\rangle\end{aligned}$$

□

Lemma A.0.6. *Let $\hat{M}_{OB}^N$ be the master equation operator for an open boundary SPS as defined in (3.41). Then, the probability vector $|\mathbb{P}^*\rangle$ as defined in (3.32) is an eigenvector for $\hat{M}_{OB}^N$ with 0 eigenvalue.*

$$\hat{M}_{OB}^N|\mathbb{P}^*\rangle = |0\rangle$$

Proof. Explicitely, the operator is given as

$$\begin{aligned}\hat{M}_{OB}^N|\mathbb{P}^*\rangle = \Bigg\{ & p\left(\hat{c}_1\hat{\alpha}_1^r - \hat{\alpha}_1^r\right) + p\sum_{x=1}^{L-1}\left[\hat{c}_{x+1}\hat{a}_x\left(\hat{u}_x\hat{v}_{x+1}\right) - \hat{u}_x\hat{v}_{x+1}\right] + p\left(\hat{a}_x\hat{\beta}_x^r - \hat{\beta}_x^r\right) + \\ & + q\left(\hat{a}_1\hat{\beta}_1^l - \hat{\beta}_1^l\right) + q\sum_{x=1}^{L-1}\left[\hat{c}_x\hat{a}_{x+1}\left(\hat{u}_{x+1}\hat{v}_x\right) - \hat{u}_{x+1}\hat{v}_x\right] + q\left(\hat{c}_x\hat{\alpha}_x^l - \hat{\alpha}_x^l\right)\Bigg\}|\mathbb{P}^*\rangle\end{aligned}$$

If we first apply the properties (3.42) of the operators to the bulk we arrive at the following expression:

$$p\sum_{x=1}^{L-1}\left[\hat{u}_{x+1}\hat{v}_x - \hat{u}_x\hat{v}_{x+1}\right] + q\sum_{x=1}^{L-1}\left[\hat{u}_x\hat{v}_{x+1} - \hat{u}_{x+1}\hat{v}_x\right]$$

Using the assumption $\hat{v}_x = \left(C\hat{u}_x + v\left(0\right)\hat{I}\right)$ made in (3.31), we obtain:

$$p\left[v\left(0\right)\hat{u}_x - v\left(0\right)\hat{u}_1\right] - q\left[v\left(0\right)\hat{u}_x - v\left(0\right)\hat{u}_1\right]$$

Consider now move the boundaries terms in $\hat{M}_{OB}^N$. Applying again the properties

of the operators gives:

$$p\left(\phi^{-1}\left\langle u\right\rangle_{*}\hat{u}_{1}-\left\langle u\right\rangle_{*}\hat{v}_{1}\right)+p\left(\phi\left\langle v\right\rangle_{*}\hat{v}_{x}-\left\langle v\right\rangle_{*}\hat{u}_{x}\right)$$
$$+q\left(\phi\left\langle v\right\rangle_{*}\hat{v}_{1}-\left\langle v\right\rangle_{*}\hat{u}_{1}\right)+q\left(\phi^{-1}\left\langle u\right\rangle_{*}\hat{u}_{x}-\left\langle u\right\rangle_{*}\hat{v}_{x}\right)$$

As a side step we notice that if we taxe the average $\left\langle\ \right\rangle_{*}$ of $\hat{v}_{x}=\left(C\hat{u}_{x}+v\left(0\right)\hat{I}\right)$ and we combine it with $\left\langle v\right\rangle_{*}=\frac{1}{\phi}\left\langle u\right\rangle_{*}$ we obtain $\phi^{-1}-C=\frac{v(0)}{\left\langle u\right\rangle_{*}}$. If we apply the first and last formula in succession to the boundary part, we get exactly the terms which cancel boundary contributions for $x=1$ and $x=L$. □

APPENDIX B

Supplementary Material on ZRP

In this Appendix, we show the proof of the lemma which supports the result in (5.24) used in Chapter 5 and we discuss the analogy between the constant rate TAZRP and the TASEP in the context of the JV approach.

B.1 A Supportive Result

Lemma B.1.1. *Consider a ZRP with critical fugacity* $\phi_c \in (0, \infty]$ *as defined in* (3.30). *If* $R(\phi)/\phi \to \infty$ *as* $\phi \to \phi_c$, *then*

$$\lim_{\phi \to \phi_c} \frac{\ln z(\phi)}{R(\phi)} = 0. \tag{B.1}$$

Note that for $\phi_c < \infty$ *the assumption is equivalent to* $R(\phi) \to \infty$ *as* $\phi \to \phi_c$.

Proof. Suppose for contradiction that there exists $A > 0$ for which

$$R(\phi) \leqslant A \ln z(\phi) \quad \text{for all } \phi \in [0, \phi_c). \tag{B.2}$$

Using the chemical potential $\mu = \ln \phi$ this can be rewritten as

$$\partial_\mu \ln z(\mu) = R(\mu) \leqslant A \ln z(\mu) \quad \text{for } \mu \in (-\infty, \ln \phi_c) \ . \tag{B.3}$$

By Gronwall's inequality this implies

$$z(\mu) \leqslant C e^{\mu} \quad \text{for some } C > 0 \ , \tag{B.4}$$

and consequently, changing back variables

$$\phi\partial_\phi \ln z(\phi) = \partial_\mu \ln z(\mu) \leqslant C' e^\mu = C'\phi \quad \text{for some } C' > 0 \ . \tag{B.5}$$

This implies

$$\tfrac{R(\phi)}{\phi} = \partial_\phi \ln z(\phi) \leqslant C' \quad \text{for all } \phi \in [0, \phi_c) \tag{B.6}$$

in contradiction to the assumption. □

B.2 Relation with EP

Any ZRP can be mapped to an *Exclusion Process* (EP) in the following way. The number of particles $\hat{N}$ of the EP is the same as for the ZRP, that is $\hat{N} = N$, while the number of sites $\hat{L}$ of the EP is given by $\hat{L} = N + L$. Then, a site of the ZRP containing m particles becomes a block of m occupied sites in the EP. This is a standard mapping [69], which leads on the level of configurations to

$$\hat{\rho} = \frac{1}{1+\rho}, \tag{B.7}$$

where $\hat{\rho}$ is the density of particles in the EP as a function of the ZRP density ρ.
In this way, for any choice of the transition rates $u(n)$, the ZRP can be mapped to an EP with jump rates depending on block sizes.
The current per site $\hat{j}$ of the EP is simply given by a renormalization of the ZRP current per site j as

$$\hat{j} = \frac{L}{L+N} j = \frac{\rho}{1+\rho} j. \tag{B.8}$$

The same applies to the stationary current

$$\hat{J}(\hat{\rho}) = \frac{\rho}{1+\rho} J(\rho) = (1-\hat{\rho})\, J\left(\frac{\hat{\rho}}{1-\hat{\rho}}\right). \tag{B.9}$$

The EP is simply another representation of the same process. In this way, the large deviation principle (5.6) implies the rate function

$$\hat{I}\left(\hat{j}\right) = I(j) = I\left(\frac{\hat{j}}{1-\hat{\rho}}\right) \tag{B.10}$$

for the exclusion model. As expected $\hat{I}\left(\hat{J}(\hat{\rho})\right) = I(J(\rho)) = 0$, so the rate function vanishes at the stationary current.
Note that, from (B.9), $\hat{J}(\hat{\rho})$ is concave, since we assumed that $J(\rho)$ is concave

as well (5.4). Also, for all sublinear currents $J(\rho)$, $\hat{J}(\hat{\rho})$ is non-monotone since $\hat{J}(\hat{\rho}) = (1-\hat{\rho})\, J\left(\frac{\hat{\rho}}{1-\hat{\rho}}\right) \to 0$ as $\hat{\rho} \to 1$. For asymptotically linear currents, like $J(\rho) \simeq d + \rho$ (see Section 3.3.1), we have $\hat{J}(\hat{\rho}) \to 1$ as $\hat{\rho} \to 1$. Furthermore, travelling wave profiles in the ZRP map to travelling waves in the EP with shock speed $\hat{v}_s = \frac{\hat{J}(\hat{\rho}_2)-\hat{J}(\hat{\rho}_1)}{\hat{\rho}_2-\hat{\rho}_1}$. Condensed states in the ZRP also map to travelling wave profiles in the EP (which does not have condensed profiles), with the condensate corresponding to a block of fully occupied sites.

The concavity of $\hat{J}(\hat{\rho})$ leads to lower current deviations being realized in the EP by phase separated profiles analogously to ZRP. (B.10) is then consistent with the Jensen-Varadhan approach applied directly to the exclusion representation of the system (as is done in [78] for the standard TASEP, which can be mapped to the constant rate ZRP).

APPENDIX C

Cloning Algorithm

The cloning algorithm, first introduced in [38] and then expanded in [37, 79, 62], allows to numerically determine the SCGF of a discrete or continuos time Markov chain. In this Appendix, we will discuss the main ideas behind the algorithm and we will give a brief sketch of the steps involved.
Starting from (4.10), we can rewrite the terms in (4.11) as

$$\left(e^{q_{hh}\tau_n} d\tau_n\right) e^{+\frac{k}{L}} q_{hj} = N\left(\eta_h, \tau_n\right) \left(e^{V(\eta_h)\tau_n} d\tau_n\right) W\left(\eta_h, \eta_j\right) \tag{C.1}$$

where

$$V\left(\eta_h\right) \coloneqq \sum_{\eta_j \neq \eta_h} e^{\frac{k}{L}\sum_{x=1}^{L} \theta^{+}_{x,x+1}(\eta_h,\eta_j)} e^{-\frac{k}{L}\sum_{x=1}^{L} \theta^{-}_{x,x+1}(\eta_h,\eta_j)} q_{hj}, \tag{C.2}$$

$$W\left(\eta_h, \eta_j\right) \coloneqq e^{\frac{k}{L}\sum_{x=1}^{L} \theta^{+}_{x,x+1}(\eta_h,\eta_j)} e^{-\frac{k}{L}\sum_{x=1}^{L} \theta^{-}_{x,x+1}(\eta_h,\eta_j)} \frac{q_{hj}}{V\left(\eta_h\right)}, \tag{C.3}$$

$$N\left(\eta_h, \tau_n\right) \coloneqq V\left(\eta_h\right) e^{(q_{hh} - V(\eta_h))\tau_n}. \tag{C.4}$$

In other words, the SCGF can be understood as the path average w.r.t. the modified dynamics $\mathbb{P}_W$ with rates W of the following quantity

$$\mathbb{E}_t\left[e^{tk\mathcal{J}_L}\right] = \int_D e^{tk\mathcal{J}_L[\eta_{[0,t]}]} \mathbb{P}\left[d\eta_{[0,t]}\right] = \int_D \mathcal{N}\left[\eta_{[0,t]}\right] \mathbb{P}_W\left[d\eta_{[0,t]}\right] =: \mathbb{E}_t^W\left[\mathcal{N}\right]. \tag{C.5}$$

Here

$$\mathcal{N}\left[\eta_{[0,t]}\right] \coloneqq \prod_{(\eta',\tau')\in\eta_{[0,t]}} N\left(\eta', \tau'\right), \tag{C.6}$$

with τ' being the relevant holding time of the state η'. It is important to notice that $\mathcal{J}_L$ is a path dependent quantity involving contributions from two configurations via θ functions, while $\mathcal{N}$ only takes into account a single η.
In the aforementioned literature, the cloning algorithm is usually understood as follows. From the process interpretation as an ensemble of clones, the path element

$N(\eta', \tau')$ can be interpreted as the population growth factor. In our case, for a single step in a generic path realization of the W-modified dynamics, starting from a configuration η, we obtain $1 \cdot n$ identical η' configurations, where $n = \lfloor N(\eta', \tau') + \epsilon \rfloor$ being ϵ a random number uniformly distributed in $[0, 1]$. In this way, considering an initial population of N_c identical *clones*, a single step of a path under $\mathbb{P}_W$ changes the total number of clones to $N_c + n - 1$. In the end, the final population size is on average $N_c(t) = \mathbb{E}_t^W[\mathcal{N}] N_c$ and the main idea is to estimate $\mathbb{E}_t^W[\mathcal{N}]$ from the ratios $\frac{N_c+n-1}{N_c}$. However, in this way $N_c(t)$ either increases or decreases exponentially in t, which is computationally impractical. For this reason, at every step the population is restored to the initial value N_c by substituting n randomly chosen clones with η'. If $n = 0$, the opposite happens, that is η' is substituted by a single randomly chosen clone.

To give a specific example of how this procedure is implemented in the thesis, we will consider the IP on a ring but the considerations presented are valid for any HCTMC. First, we noticed that (4.41) can be rewritten (simply by summing and substracting suitable terms) as

$$\tilde{M}_{ring}^{N,J}(k) = p\left\{\delta_p(k)\left[\sum_{x=1}^{L}\left\lceil e^{\frac{k}{L}}\right\rceil \hat{c}_{x+1}\hat{a}_x(\hat{u}_x\hat{v}_{x+1}) - \hat{u}_x\hat{v}_{x+1}\right]\right\} \tag{C.7}$$

$$+ p\left\{(1-\delta_p(k))\left[\sum_{x=1}^{L}\left\lfloor e^{\frac{k}{L}}\right\rfloor \hat{c}_{x+1}\hat{a}_x(\hat{u}_x\hat{v}_{x+1}) - \hat{u}_x\hat{v}_{x+1}\right]\right\} \tag{C.8}$$

$$+ q\left\{\delta_q(k)\left[\sum_{x=1}^{L}\left\lceil e^{-\frac{k}{L}}\right\rceil \hat{c}_x\hat{a}_{x+1}(\hat{u}_{x+1}\hat{v}_x) - \hat{u}_{x+1}\hat{v}_x\right]\right\} \tag{C.9}$$

$$+ q\left\{(1-\delta_q(k))\left[\sum_{x=1}^{L}\left\lfloor e^{-\frac{k}{L}}\right\rfloor \hat{c}_x\hat{a}_{x+1}(\hat{u}_{x+1}\hat{v}_x) - \hat{u}_{x+1}\hat{v}_x\right]\right\}, \tag{C.10}$$

where

$$\delta_p(k) \coloneqq e^{\frac{k}{L}} - \left\lfloor e^{\frac{k}{L}}\right\rfloor \quad \text{and} \quad \delta_q(k) \coloneqq e^{-\frac{k}{L}} - \left\lfloor e^{-\frac{k}{L}}\right\rfloor . \tag{C.11}$$

We notice that if $k > 0$, $\left\lceil e^{-\frac{k}{L}}\right\rceil = 1$ (which, as we will see, corresponds to keep the population size to N_c) and $\left\lfloor e^{-\frac{k}{L}}\right\rfloor = 0$ (which corresponds to kill the new state by substitution with another randomly chosen agent). The resulting clones dynamics expressed by $\tilde{M}_{ring}^{N,J}(k)$ is understood as follows.

- Using a binary tree architecture to keep track of all the clones, we determine, through an exact Gillespie algorithm on the dynamics generated by the original $\hat{M}_{ring}^{N}$, the first jumping particle.

- As an example, consider a right jumping particle. Then, with probability $\delta_p(k)$ (or 1-$\delta_p(k)$) the new state is copied $\left\lceil e^{\frac{k}{L}} \right\rceil - 1$ (or $\left\lfloor e^{\frac{k}{L}} \right\rfloor$-1) times onto randomly chosen agents in N_c. The population growth ratio is then $\frac{N_c + \left\lceil e^{\frac{k}{L}} \right\rceil - 1}{N_c}$.

- We notice that for the generator chosen in this example, the agents population can change in only four possible ways given by $\left\lceil e^{\frac{k}{L}} \right\rceil$, $\left\lfloor e^{\frac{k}{L}} \right\rfloor$, $\left\lceil e^{-\frac{k}{L}} \right\rceil$ and $\left\lfloor e^{-\frac{k}{L}} \right\rfloor$. Since after each cloning step the population size is artificially left unchanged, all we need to keep track of is the amount of times each unit is picked, which we label as c_p^+, c_p^-, c_q^+ and c_q^-, respectively.

- In the end, we can determine the SCGF as the product

$$\mathbb{E}_t\left[e^{tk\mathcal{J}_L}\right] \simeq \left(\frac{N_c + \left\lceil e^{\frac{k}{L}} \right\rceil - 1}{N_c}\right)^{c_p^+} \cdot \left(\frac{N_c + \left\lfloor e^{\frac{k}{L}} \right\rfloor - 1}{N_c}\right)^{c_p^-} \tag{C.12}$$

$$\cdot \left(\frac{N_c + \left\lceil e^{-\frac{k}{L}} \right\rceil - 1}{N_c}\right)^{c_q^+} \cdot \left(\frac{N_c + \left\lfloor e^{-\frac{k}{L}} \right\rfloor - 1}{N_c}\right)^{c_q^-} \tag{C.13}$$

Bibliography

[1] Agliari, E., Barra, A., Galluzzi, A., Pizzoferrato, A., and Tantari, D. (2014). Ferromagnetic models for cooperative behavior: Revisiting universality in complex phenomena. In *Mathematical Models and Methods for Planet Earth*, pages 73–86. Springer.

[2] Anderson, W. J. (2012). *Continuous-time Markov chains: An applications-oriented approach*. Springer Science & Business Media.

[3] Andjel, E. D. (1982). Invariant Measures for the Zero Range Process. *The Annals of Probability*, 10(3):525–547.

[4] Angeletti, F. and Touchette, H. (2016). Diffusions conditioned on occupation measures. *Journal of Mathematical Physics 57, 023303 (2016).*

[5] Barra, A., Contucci, P., Sandell, R., and Vernia, C. (2014). An analysis of a large dataset on immigrant integration in spain. the statistical mechanics perspective on social action. *Scientific reports*, 4:4174.

[6] Barra, A. and Moro, A. (2015). Exact solution of the van der Waals model in the critical region. *Annals of Physics*, 359:290–299.

[7] Bertini, L., De Sole, A., Gabrielli, D., Jona-Lasinio, G., and Landim, C. (2002). Macroscopic fluctuation theory for stationary non-equilibrium states. *Journal of Statistical Physics*, 107(3-4):635–675.

[8] Bertini, L., De Sole, A., Gabrielli, D., Jona-Lasinio, G., and Landim, C. (2015a). Macroscopic fluctuation theory. *Reviews of Modern Physics*, 87(2):593.

[9] Bertini, L., Faggionato, A., and Gabrielli, D. (2015b). Flows, currents, and cycles for markov chains: Large deviation asymptotics. *Stochastic Processes and their Applications, 125(7), 2786-2819. 10.1016/j.spa.2015.02.001.*

[10] Bertini, L., Faggionato, A., and Gabrielli, D. (2015c). Large deviations of the empirical flow for continuous time markov chains. *Annales de l'institut Henri Poincare (B) Probability and Statistics, 51(3), 867-900. 10.1214/14-AIHP601.*

[11] Bhattacharya, R. and Waymire, E. (2007). *A basic course in probability theory*, volume 69. Springer.

[12] Bialas, P., Burda, Z., Petersson, B., and Tabaczek, J. (1997). Appearance of mother universe and singular vertices in random geometries. *Nuclear Physics B*, 495(3):463–476.

[13] Bodineau, T. and Derrida, B. (2004). Current fluctuations in nonequilibrium diffusive systems: An additivity principle. *Physical Review Letters 92, 180601.*

[14] Bodineau, T. and Derrida, B. (2006). Current large deviations for asymmetric exclusion processes with open boundaries. *Journal of statistical physics*, 123(2):277–300.

[15] Burda, Z., Johnston, D., Jurkiewicz, J., Kamiński, M., Nowak, M., Papp, G., and Zahed, I. (2002). Wealth condensation in Pareto macroeconomies. *Physical Review E*, 65(2):026102.

[16] Chaichian, M. and Demichev, A. (2001). *Path integrals in physics. Vol. 1: Stochastic processes and quantum mechanics*. IOP, Bristol, UK.

[17] Chetrite, R. and Touchette, H. (2015). Nonequilibrium Markov processes conditioned on large deviations. *Annales Henri Poincaré*, 16(9):2005–2057.

[18] Chleboun, P. and Grosskinsky, S. (2010). Finite size effects and metastability in zero-range condensation. *Journal of Statistical Physics 140: 846872.*

[19] Chleboun, P. and Grosskinsky, S. (2014). Condensation in stochastic particle systems with stationary product measures. *Journal of Statistical Physics*, 154(1-2):432–465.

[20] Chleboun, P., Grosskinsky, S., and Pizzoferrato, A. (2017). Lower current large deviations for Zero-Range Processes on a ring. *Journal of Statistical Physics*, 167(1):64–89.

[21] Chowdhury, D., Santen, L., and Schadschneider, A. (2000). Statistical physics of vehicular traffic and some related systems. *Physics Reports*, 329(4):199–329.

[22] Chowdhury, D. and Stauffer, D. (2000). *Principles of equilibrium statistical mechanics*. Wiley Online Library.

[23] Cocozza-Thivent, C. (1985). Processus des misanthropes. *Probability Theory and Related Fields*, 70(4):509–523.

[24] Coolen, A., Kühn, R., and Sollich, P. (2005). *Theory of neural information processing systems*. OUP Oxford.

[25] Den Hollander, F. (2008). *Large deviations*, volume 14. American Mathematical Soc.

[26] Derrida, B. (2007). Non-equilibrium steady states: fluctuations and large deviations of the density and of the current. *Journal of Statistical Mechanics: Theory and Experiment*, 2007(07):P07023.

[27] Di Castro, C. and Raimondi, R. (2015). *Statistical Mechanics and Applications in Condensed Matter*. Cambridge University Press.

[28] Drouffe, J.-M., Godrèche, C., and Camia, F. (1998). A simple stochastic model for the dynamics of condensation. *Journal of Physics A: Mathematics and General*, 31(1):L19.

[29] Durlauf, S. (1996). Statistical mechanics approaches to socioeconomic behavior. *National Bureau of Economic Research*, 203.

[30] Durlauf, S. (1999). How can statistical mechanics contribute to social science? *Proceedings of the National Academy of Sciences*, 96(19):10582–10584.

[31] Eggers, J. (2009). Sand as Maxwell's demon. *Physical Review Letters 83, 5322*.

[32] Ellis, R. (2007). *Entropy, large deviations, and statistical mechanics*. Springer.

[33] Evans, M. (2000). Phase transitions in one-dimensional nonequilibrium systems. *Brazilian Journal of Physics*, 30.

[34] Evans, M., Majumdar, S., Pagonabarraga, I., and Trizac, E. (2010). Condensation transition in polydisperse hard rods. *The Journal of chemical physics*, 132(1):014102.

[35] Evans, M. R. and Hanney, T. (2005). Nonequilibrium statistical mechanics of the zero-range process and related models. *Journal of Physics A: Mathematics and General*, 38(19):R195.

[36] Galam, S. (2012). *Sociophysics: a physicist's modeling of psycho-political phenomena*. Springer Science & Business Media.

[37] Giardinà, C., Kurchan, J., Lecomte, V., and Tailleur, J. (2011). Simulating Rare Events in Dynamical Processes. *Journal of Statistical Physics*, 145:787–811.

[38] Giardinà, C., Kurchan, J., and Peliti, L. (2006). Direct evaluation of large-deviation functions. *Physical review letters*, 96(12):120603.

[39] Giardinà, C., Redig, F., and Vafayi, K. (2010). Correlation inequalities for interacting particle systems with duality. *Journal of Statistical Physics*, 141(2):242–263.

[40] Godrèche, C. (2007). From Urn models to Zero-Range Processes: statics and dynamics. *Lecture notes in Physics*, 716:261–294.

[41] Godrèche, C. and Luck, J.-M. (2012). Condensation in the inhomogeneous Zero-Range Process: an interplay between interaction and diffusion disorder. *Journal of Statistical Mechanics: Theory and Experiment*, 2012(12):P12013.

[42] Gorissen, M., Lazarescu, A., Mallick, K., and Vanderzande, C. (2012). Exact current statistics of the Asymmetric Simple Exclusion Process with open boundaries. *Physical review letters*, 109(17):170601.

[43] Grosskinsky, S. (2013). Interacting stochastic particle systems. *London Mathematical Society Lecture Note Series*, 1(408):125–209.

[44] Grosskinsky, S., Redig, F., and Vafayi, K. (2011). Condensation in the Inclusion Process and related models. *Journal of Statistical Physics*, 142(5):952–974.

[45] Grosskinsky, S., Schütz, G. M., and Spohn, H. (2003). Condensation in the Zero Range Process: stationary and dynamical properties. *Journal of Statistical Physics*, 113(3-4):389–410.

[46] Gupta, S., Barma, M., and Majumdar, S. N. (2007). Finite-size effects on the dynamics of the Zero-Range Process. *Physical Review E*, 76(6):060101.

[47] Harris, R., Rákos, A., and Schütz, G. (2005). Current fluctuations in the Zero-Range Process with open boundaries. *Journal of Statistical Mechanics: Theory and Experiment*, 2005(08):P08003.

[48] Harris, R. and Schütz, G. (2007). Fluctuation theorems for stochastic dynamics. *Journal of Statistical Mechanics: Theory and Experiment*, 2007(07):P07020.

[49] Harris, R. J., Popkov, V., and Schütz, G. M. (2013). Dynamics of instantaneous condensation in the ZRP conditioned on an atypical current. *Entropy*, 15(11):5065–5083.

[50] Harris, R. J., Rákos, A., and Schütz, G. M. (2006). Breakdown of Gallavotti–Cohen symmetry for stochastic dynamics. *Europhysics Letters*, 75:227.

[51] Hirschberg, O., Mukamel, D., and Schütz, G. M. (2015). Density profiles, dynamics, and condensation in the ZRP conditioned on an atypical current. *Journal of statistical mechanics: theory and experiment*, 2015(11):P11023.

[52] Izyumov, Y. A. and Skryabin, Y. N. (1988). *Statistical mechanics of magnetically ordered systems*. Springer Science & Business Media.

[53] Jack, R. L., Thompson, I. R., and Sollich, P. (2015). Hyperuniformity and phase separation in biased ensembles of trajectories for diffusive systems. *Physical review letters*, 114(6):060601.

[54] Jensen, L. H. (2000). *Large Deviations of the Asymmetric Simple Exclusion Process in One Dimension*. PhD thesis, NYU.

[55] Jordan, T. (2012). *Linear operators for quantum mechanics*. Courier Corporation.

[56] Kipnis, C. and Landim, C. (2013). *Scaling limits of interacting particle systems*, volume 320. Springer.

[57] Kobayashi, H., Mark, B., and Turin, W. (2011). *Probability, random processes, and statistical analysis: applications to communications, signal processing, queueing theory and mathematical finance*. Cambridge University Press.

[58] Krapivsky, P., Redner, S., and Leyvraz, F. (2000). Connectivity of growing random networks. *Physical Review Letters*, 85(21):4629.

[59] Lazarescu, A. (2013). *Exact Large Deviations of the Current in the Asymmetric Simple Exclusion Process with Open Boundaries*. PhD thesis, IPhT CEA-Saclay.

[60] Lazarescu, A. (2015). The physicist's companion to current fluctuations: one-dimensional bulk-driven lattice gases. *Journal of Physics A: Mathematical and Theoretical*, 48(50):503001.

[61] Lebowitz, J. L. and Spohn, H. (1999). A Gallavotti-Cohen type symmetry in the large deviation functional for stochastic dynamics. *Journal of Statistical Physics*, 95(1-2):333–365.

[62] Lecomte, V. and Tailleur, J. (2007). A numerical approach to large deviations in continuous time. *Journal of Statistical Mechanics: Theory and Experiment*, 2007(03):P03004.

[63] Liggett, T. (2010). *Continuous time Markov processes: an introduction*, volume 113. American Mathematical Society.

[64] Liggett, T. (2012). *Interacting particle systems*, volume 276. Springer Science & Business Media.

[65] Mallick, K. (2015). The Exclusion Process: A paradigm for non-equilibrium behaviour. *Physica A: Statistical Mechanics and its Applications*, 418:17–48.

[66] Popkov, V., Schütz, G. M., and Simon, D. (2010). ASEP on a ring conditioned on enhanced flux. *Journal of Statistical Mechanics: Theory and Experiment*, 2010(10):P10007.

[67] Press, W. (2007). *Numerical recipes 3rd edition: The art of scientific computing*. Cambridge university press.

[68] Rákos, A. and Harris, R. J. (2008). On the range of validity of the fluctuation theorem for stochastic markovian dynamics. *Journal of Statistical Mechanics: Theory and Experiment*, 2008(05):P05005.

[69] Schadschneider, A., Chowdhury, D., and Nishinari, K. (2010). *Stochastic transport in complex systems: from molecules to vehicles*. Elsevier.

[70] Schütz, G. (2015). The space-time structure of extreme current and activity events in the ASEP. In *Nonlinear Mathematical Physics and Natural Hazards*, pages 13–28. Springer.

[71] Schütz, G. (2017). Fluctuations in stochastic interacting particle systems. *Pre-School Lecture Notes of the Conference – Stochastic Dynamics out of Equilibrium*.

[72] Schütz, G., Domb, C., and Lebowitz, J. (2000). *Phase transitions and critical phenomena*, volume 19. Academic Press, London.

[73] Serre, D. (1999). *Systems of Conservation Laws 1: Hyperbolicity, entropies, shock waves*. Cambridge University Press.

[74] Smoller, J. (1994). *Shock Waves and Reaction-Diffusion Equations*. Springer.

[75] Spitzer, F. (1970). Interaction of Markov processes. *Advances in Mathematics*, 5:246–290.

[76] Spohn, H. (2012). *Large scale dynamics of interacting particles*. Springer.

[77] Stanley, H., Buldyrev, S., Goldberger, A., Goldberger, Z., Havlin, S., Mantegna, R. N., Ossadnik, S., Peng, C.-K., and Simons, M. (1994). Statistical Mechanics in biology: how ubiquitous are long-range correlations? *Physica A: Statistical Mechanics and its Applications*, 205(1-3):214–253.

[78] T. Bodineau, B. D. (2005). Distribution of current in nonequilibrium diffusive systems and phase transitions. *Physical Review E 72, 066110.*

[79] Tailleur, J. and Lecomte, V. (2009). Simulation of large deviation functions using population dynamics. In *AIP Conference Proceedings*, volume 1091, pages 212–219. AIP.

[80] Touchette, H. (2009). The large deviation approach to Statistical Mechanics. *Physics Reports*, 478:1–95.

[81] Touchette, H. (2012). A basic introduction to large deviations: Theory, applications, simulations. *arXiv preprint arXiv:1106.4146.*

[82] Touchette, H. (2015). Equivalence and nonequivalence of ensembles: Thermodynamic, macrostate, and measure levels. *Journal of Statistical Physics*, 159(5):987–1016.

[83] Tsobgni, N. P. and Touchette, H. (2016). Large deviations of the current for driven periodic diffusions. *Physical Review. E*, 94(3-1):032101.

[84] Vafayi, K. and Duong, M. (2014). Weakly nonequilibrium properties of a Symmetric Inclusion Process with open boundaries. *Physical Review E*, 90(5):052143.

[85] van Enter, A. and den Hollander, F. (1992). Interacting Particle Systems and Gibbs Measures. *Lecture Notes, Master Class*, 93.

[86] Varadhan, S. R. S. (2004). Large deviations for the Asymmetric Simple Exclusion Process. *Advanced Studies in Pure Mathematics*, pages 1–27.

[87] Vilensky, Y. (2008). *Large Deviation Lower Bounds for the Totally Asymmetric Simple Exclusion Process.* PhD thesis, NYU.

[88] Villavicencio-Sanchez, R., Harris, R. J., and Touchette, H. (2012). Current loops and fluctuations in the Zero-Range Process on a diamond lattice. *Journal of Statistical Mechanics: Theory and Experiment*, 2012(07):P07007.

[89] Weber, M. and Frey, E. (2017). Master equations and the theory of stochastic path integrals. *Reports on Progress in Physics*, 80(4):046601.

[90] Wolynes, P. G. and Lubchenko, V. (2012). *Structural Glasses and Supercooled Liquids: Theory, Experiment, and Applications*. John Wiley & Sons.